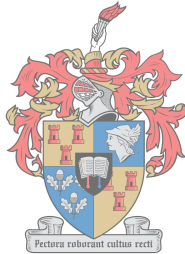


Assessment of SHCC overlay retrofitting of unreinforced load
bearing masonry for seismic resistance

by

Dirk Jacobus Adriaan de Jager



UNIVERSITEIT
iYUNIVESITHI
UNIVERSITY
*Thesis presented in partial fulfilment of the requirements for
the degree of Master of Engineering in Structural Engineering
in the Faculty of Engineering at Stellenbosch University*
100
1918 · 2018

Supervised by:

Prof. G.P.A.G van Zijl

December 2018

Declaration

By submitting this thesis electronically, I declare that the entirety of the work contained herein is my own original work, and that I am the sole author hereof (save to the extent explicitly otherwise stated), that reproduction and publication thereof by Stellenbosch University will not infringe any third-party rights and that I have not previously in its entirety or in part submitted it for obtaining any qualification.

Signature:

Date:

Abstract

A significant stock of multi-story unreinforced load bearing masonry (ULM) structures is located in the Cape Town region (South Africa). The region is categorised as a light to moderate seismic region. Retrofitting techniques of these buildings have been proposed at Stellenbosch University by a group of researchers. The research is motivated by the large number of ULM structures constructed prior to seismic activity becoming a requirement in the South African National Standard in 1989. These buildings will undergo poor shear behaviour during seismic events due to their brittle in-plane shear response. A Strain Hardening Cement-based Composite (SHCC), which can be applied by spraying, was developed as a retrofitting overlay material to improve shear behaviour during seismic events.

Triplet tests were performed on the SHCC for characterizing the bonding strength of the masonry/SHCC interface and the shear behaviour while the SHCC form fine multiple cracks. Drying shrinkage of free and restrained specimens was measured. The characterized response of the SHCC enabled the design of favourable overlay thickness and obtaining test specifications on walls loaded by an in-plane shear force.

This research also reports the nonlinear finite element analysis (FEA) of the large-scale tests performed previously at Stellenbosch University. The computational model is calibrated and used for extrapolation to other cases. A debonded strip interface strategy is analysed and subsequently validated by laboratory tests to obtain an improved ductility performance.

Eight walls with varying wall and overlay thickness (single and double leaf walls, and 15 mm and 30 mm overlay) were previously tested in the Stellenbosch University structures laboratory. The calibrated data is used to perform nonlinear analyses, using the DIANA FEA software, on masonry walls retrofitted with an SHCC overlay and subjected to a pull-over force, while restraint is provided vertically to simulate the effect of multiple stories. The performed analysis and material parameters on shear walls with and without SHCC overlay are used as calibration. However, the primary aim was the calibration of the double leaf wall retrofitted with 15 mm overlay. An anisotropic continuum model, allowing for compression hardening along with compression and tension softening, was used to model the masonry wall. A rotating smeared cracking principal stress limit function is used for the modelling of the SHCC, simulating elastic-perfect plastic tensile behaviour. Coulomb-friction plane interface is used to model the masonry/SHCC interface. After computational calibration, alternate debonded strip interfaces are applied and modelled. The analysis reveals that the debonded interfaces provide an enlarged crack distribution and enhanced ductility.

The results of tests performed on four double leaf walls containing debonded strip interfaces and 15 mm overlays, and one without the strips are presented. The tests demonstrate an enlarged cracking region and improved ductility of walls containing debonded strips, compared to the reference wall without debonded strips. The enhanced wall deformation capacity brought about by the strip debonded overlay

improves the potential of exceeding the earthquake displacement demand expected in the particular region and founding soil type.

It can be concluded that the sprayed SHCC retrofitting of shear walls with debonded strip interfaces provides significant in-plane strength and ductility enhancements when subjected to seismic loading regimes. Further development and testing on full scale ULM buildings are recommended.

Acknowledgements

My greatest appreciation goes to my supervisor and study leader, Professor Gideon Van Zijl, without who's knowledge, support, and motivation this research project would not have been possible. His experience and guidance added tremendous contribution to this project.

I would like to further express my great appreciation towards the following people:

- Dr Stephan Zeranka, for his guidance and assistance in the laboratory during construction of the test setup and testing. I thank him for his time for operating the Instron machine.
- Mr Ramat and Mr Jones (laboratory staff), for their help throughout all laboratory work performed. Thank you for always assisting me in the times when it was needed.
- Uncle Johan, for all the great lessons he taught me in the workshop. I thank you for all your time.
- DIANA support team, for providing help and tutorials that were valuable during computational modelling. Thank you for your quick responses.
- The Civil Engineering department at Stellenbosch University for allowing me the time and space to finish this project over two years, and for providing all the necessary materials.
- My office colleagues for their motivation and putting a smile on my face during difficult times.

I would also like to express my great appreciation to my family and friends for all their love and support. I especially want to thank my dad for giving me the financial support to complete my MEng degree.

Contents

| | |
|--|-----|
| Declaration | i |
| Abstract | ii |
| Acknowledgements | iv |
| Contents..... | v |
| List of Figures | vii |
| List of Tables..... | xi |
| Abbreviations | xii |
| Chapter 1 | 1 |
| Introduction | 1 |
| 1.1 Motivation | 2 |
| 1.2 Outline..... | 2 |
| Chapter 2 | 4 |
| Literature Review | 4 |
| 2.1 Seismic activity in South-Africa | 4 |
| 2.1.1 Introduction | 4 |
| 2.1.2 Structural seismic design considerations..... | 5 |
| 2.2 Masonry..... | 6 |
| 2.2.1 Unreinforced Masonry (URM) buildings..... | 6 |
| 2.2.2 Failure modes of URM shear walls..... | 8 |
| 2.3 Retrofitting of URM buildings..... | 9 |
| 2.3.1 Carbon Fibre Reinforced Polymer (CFRP) strips..... | 9 |
| 2.3.2 Near Surface Mounted (NSM) reinforcement including steel mesh..... | 10 |
| 2.3.3 SHCC bonded overlays | 10 |
| 2.4 Strain Hardening Cement-based Composites (SHCC)..... | 11 |
| 2.4.1 SHCC tensile behaviour | 11 |
| 2.4.2 SHCC flexural behavior | 13 |
| 2.4.3 SHCC shear behaviour | 14 |
| 2.4.4 Compressive behaviour | 15 |
| 2.4.5 Elastic modulus (E)..... | 15 |
| 2.4.6 Properties of the matrix constituents..... | 15 |
| 2.5 Development of a sprayable SHCC mix | 16 |
| 2.5.1 Considerations for a sprayable mix | 16 |
| 2.5.2 Adopted sprayable mix..... | 17 |
| 2.5.3 Direct Tensile Test (DTT)..... | 17 |
| 2.5.4 Cast vs sprayed specimens | 19 |

| | | |
|---|---|----|
| 2.6 | Shrinkage..... | 19 |
| 2.6.1 | Shrinkage mechanisms | 19 |
| 2.6.2 | Bonded overlays subjected to restrained shrinkage..... | 20 |
| 2.7 | Computational Modelling..... | 21 |
| 2.7.1 | Discrete crack modelling..... | 21 |
| 2.7.2 | Smearred crack modelling | 21 |
| 2.8 | Nonlinear Structural Analysis using DIANA..... | 22 |
| 2.8.1 | Convergence issues | 22 |
| 2.8.2 | Input data affecting nonlinear analysis..... | 23 |
| 2.8.3 | Analysis procedures | 24 |
| 2.9 | Bonded SHCC Overlay Systems | 27 |
| 2.9.1 | Bonded SHCC overlay subjected to mechanical loading..... | 27 |
| 2.9.2 | Bonded SHCC overlay subjected to drying shrinkage conditions..... | 29 |
| 2.9.3 | Balanced interface behaviour | 30 |
| 2.10 | Earthquake Displacement Demand | 31 |
| Chapter 3 | | 32 |
| Nonlinear Computational Modelling of Shear Walls..... | | 32 |
| 3.1 | DIANA FEA Shear wall model setup | 33 |
| 3.1.1 | Geometry | 33 |
| 3.1.2 | Material Properties | 34 |
| 3.1.3 | Boundary Conditions..... | 37 |
| 3.1.4 | Loadings..... | 37 |
| 3.1.5 | Mesh | 38 |
| 3.1.6 | Analysis..... | 40 |
| 3.2 | Results and Discussions of Shear Wall Computational Models..... | 44 |
| 3.2.1 | Bare masonry shear walls without retrofitting overlay | 44 |
| 3.2.2 | Masonry shear walls retrofitted with SHCC | 49 |
| 3.3 | Conclusions and recommendations | 60 |
| Chapter 4 | | 62 |
| Computational Prediction and Experimental Validation Design of Strip Debonded Overlay | | 62 |
| 4.1 | Modelling of shear walls retrofitted with SHCC overlay and debonded strip interfaces..... | 63 |
| 4.1.1 | Setup..... | 63 |
| 4.1.2 | Results and discussions | 65 |
| 4.2 | Experimental SHCC overlay and debonded strips spray-ability and adherence testing..... | 69 |
| 4.2.1 | Shotcrete equipment | 69 |
| 4.2.2 | SHCC mix design..... | 70 |
| 4.2.3 | Deformability test..... | 71 |
| 4.2.4 | Spray-ability and adhesion to small-scale masonry test walls | 73 |
| 4.3 | Masonry shear wall test setup | 76 |

| | | |
|--|---|-----|
| 4.3.1 | Introduction | 76 |
| 4.3.2 | Mortar and masonry brick compressive tests | 76 |
| 4.3.3 | Experimental shear wall specimen | 77 |
| 4.3.4 | Testing machine | 81 |
| 4.3.5 | Constraints and loading regimes | 87 |
| 4.3.6 | Collecting data..... | 88 |
| 4.4 | Conclusions and recommendations | 88 |
| Chapter 5 | | 90 |
| Results and Discussion..... | | 90 |
| 5.1 | Introduction | 90 |
| 5.2 | Compressive strength | 90 |
| 5.3 | Shear wall results..... | 91 |
| 5.3.1 | Boundary conditions results and interpretation..... | 91 |
| 5.4 | Shear wall results comparison..... | 105 |
| 5.4.1 | Shear walls test results summary..... | 105 |
| 5.4.2 | Debonded strip interface energy contribution | 107 |
| 5.5 | Concluding Summary..... | 111 |
| Chapter 6 | | 113 |
| Conclusions and Recommendations..... | | 113 |
| 6.1 | Conclusions | 113 |
| 6.1.1 | Nonlinear FEA and calibration..... | 113 |
| 6.1.2 | Debonded strip interface computational modelling..... | 114 |
| 6.1.3 | Shear wall experimental validation | 115 |
| 6.2 | Recommendations | 116 |
| References | | 118 |
| Appendices | | 121 |
| Appendix A – Computational models without strips | | 122 |
| With and without bonded SHCC overlay..... | | 122 |
| Appendix B – Experimental setup..... | | 130 |

List of Figures

| | |
|---|---|
| Figure 2.1: South African seismic hazard map with peak ground accelerations, 10% in 50 years exceedance probability (SANS 10160-4, 2011)..... | 5 |
| Figure 2.2: URM structural load path system (eg. Van Der Kolf, 2014). | 7 |
| Figure 2.3: Examples of damage to New Zealand URM buildings as a result of seismic loading. | 8 |

| | |
|---|----|
| Figure 2.4: In-plane mechanisms of failure of URM shear walls (Tomazevic, 1999)..... | 9 |
| Figure 2.5: URM shear walls in-plane retrofitting techniques adopted from Van Zijl et al. (2005) and ElGawady et al. (2006)..... | 10 |
| Figure 2.6: (a) Stress-strain behaviour of HPFRCC materials subjected to uniaxial tensile forces and (b) crack width control exhibited by SHCC adopted from Van Zijl et al. (2012)..... | 12 |
| Figure 2.7: Tensile response of SHCC when subjected to cyclic loading (Boshoff and Van Zijl, 2007). | 13 |
| Figure 2.8: Four-point bending test setup and flexure response conducted by Dehghani et al. (2013). 14 | |
| Figure 2.9: (a) Iosipescu shear beam test and (b) shear behaviour of SHCC adopted from Van Zijl (2007). | 14 |
| Figure 2.10: DTT adopted from Boshoff (2007)..... | 18 |
| Figure 2.11: Restrained shrinkage tests where (a) vertically restrained, (b) horizontally restrained, (c) SHCC specimen, (d) LVDT, and (e) 1150 x 935 mm specimen (De Beer, 2016)..... | 20 |
| Figure 2.12: Incremental load methods (Palacio, 2013)..... | 25 |
| Figure 2.13: Iterative solution procedures (Palacio, 2013). | 26 |
| Figure 2.14: Simulations of the beams subjected to three-point bending showing the crack patterns with the SHCC at the bottom (Luković et al., 2014)..... | 28 |
| Figure 2.15: simulations showing the crack patterns where the overlay is applied at the top compression face of the three-point bending test (Luković et al., 2014). | 28 |
| Figure 2.16: Crack distributions of simulations obtained by drying the top surface of the SHCC material (Luković et al., 2014). | 29 |
| Figure 2.17: (a) and (b) flexural experiments with SHCC on a concrete substrate, followed by the simulations with (c) 55% of maximum load and (d) maximum load (Van Zijl and Stander, 2009). | 30 |
| Figure 3.1: Experimental masonry shear wall setup (De Beer, 2016)..... | 32 |
| Figure 3.2: Geometrical setup of computational shear wall model..... | 33 |
| Figure 3.3: Yield conditions of a Rankine-Hill material model. | 34 |
| Figure 3.4: Linear-crack fracture energy curve..... | 35 |
| Figure 3.5: Triangular finite membrane and interface elements. | 39 |
| Figure 3.6: Mesh dependence test performed on 220 mm masonry wall with 15 mm SHCC overlay (SW220-15). | 39 |
| Figure 3.7: Triangular 30 mm mesh of elements. | 40 |
| Figure 3.8: Procedures with (a) Phase analysis; (b) Stress initialization..... | 41 |
| Figure 3.9: Convergence procedure (Manie and Kikstra, 2017). | 42 |
| Figure 3.10: (a) Properties of iteration method, (b) Solution procedure. | 43 |
| Figure 3.11: Shear force-displacement diagram of shear wall with no retrofitting overlay..... | 45 |
| Figure 3.12: Failure mechanisms of SW220-0 experimental test; (a) Cracked experimental specimen; (b) Documented visualisation of the crack formation (De Beer, 2016). | 46 |
| Figure 3.13: Principle strains (E_1) of SW220-0 at different top horizontal displacements. | 47 |
| Figure 3.14: Compressive stress (S_{yy}) diagrams of the SW220-0 model at different pull-over displacements. | 48 |
| Figure 3.15: Principle Vertical stress (S_2) in SW220-0 at varying pull-over displacements..... | 48 |

| | |
|---|----|
| Figure 3.16: Shear force vs horizontal displacement diagram of 220 mm thick shear wall retrofitted with 15mm SHCC overlay. | 49 |
| Figure 3.17: Principle strains (E_1) of SW220-15 at different horizontal displacements..... | 50 |
| Figure 3.18: The principle vertical stress (S_2) and compressive stress (S_{yy}) of the SW220-15 model. | 51 |
| Figure 3.19: Shear force-displacement diagram of SW220-10, SW220-15 and SW220-30..... | 52 |
| Figure 3.20: Principle strain diagrams of SW220-30 model..... | 53 |
| Figure 3.21: The principle vertical stress (S_2) and compressive stress (S_{yy}) of the SW220-30 model. | 54 |
| Figure 3.22: Shear force-displacement diagram of SW110-10, SW110-15 and SW110-30..... | 55 |
| Figure 3.23: Principle strain diagrams of SW110-30 model..... | 56 |
| Figure 3.24: The principle vertical stress (S_2) and compressive stress (S_{yy}) of the SW110-30 model. | 57 |
| Figure 3.25: Shear force-displacement diagram of SW330-10, SW330-15 and SW330-30..... | 58 |
| Figure 3.26: Principle strain diagrams of SW330-15 model..... | 58 |
| Figure 3.27: The principle vertical stress (S_2) and compressive stress (S_{yy}) of the SW330-15 model. | 59 |
| Figure 4.1: Debonded strip model layout..... | 62 |
| Figure 4.2: Debonded strip model geometry..... | 64 |
| Figure 4.3: Debonded strip model mesh..... | 64 |
| Figure 4.4: Shear force vs horizontal displacement diagram of shear walls retrofitted with 15 mm SHCC overlay with and without debonding strips..... | 65 |
| Figure 4.5: Principle strain diagrams of SW-75-150-Strip Analysis model at different horizontal displacements..... | 67 |
| Figure 4.6: The principle vertical stress (S_2) and compressive stress (S_{yy}) of the SW-75-150-Strip Analysis model..... | 68 |
| Figure 4.7: Rockcrete-TSL shotcrete equipment..... | 69 |
| Figure 4.8: Circumferential nozzle..... | 70 |
| Figure 4.9: Slump flow test (a) directly after mixing, and (b) 15 minutes after mixing..... | 71 |
| Figure 4.10: Deformability γ and Γ after time of mixing with the adopted SHCC mix..... | 72 |
| Figure 4.11: Spray-ability and adhesion testing on small-scale test wall specimens..... | 73 |
| Figure 4.12: SHCC thickness before and after trowelling..... | 74 |
| Figure 4.13: Tape bonding to masonry and surface roughness tests..... | 75 |
| Figure 4.14: Run-off and surface roughness tests..... | 75 |
| Figure 4.15: Burned clay bricks..... | 77 |
| Figure 4.16: Shear wall specimen dimensions..... | 78 |
| Figure 4.17: Concrete beam dimensions (De Beer, 2016)..... | 78 |
| Figure 4.18: RC beams casting mould and procedure (De Beer, 2016)..... | 79 |
| Figure 4.19: Masonry walls with debonding strips..... | 80 |
| Figure 4.20: Retrofitting shear walls with SHCC overlay..... | 80 |
| Figure 4.21: Testing machine setup with a SW specimen in place; (a) Instron supporting frame; (b) Instron actuator; (c) Base steel beam; (d) Instron head lateral roller support; (e) Load spreader beam; (f) Coil springs; (g) Lateral roller supporting frame structure; (h) Spreader beam connected to a lateral support; (i) Vertical roller support; (j) Camera..... | 82 |
| Figure 4.22: Lateral roller supports at (a) Instron head and (b) spreader beam..... | 83 |

| | |
|---|-----|
| Figure 4.23: Vertical roller support..... | 83 |
| Figure 4.24: Testing setup layout..... | 84 |
| Figure 4.25: SWS in the testing rig in place and the LVDT's indicated with blue boxes; (a) Instron head/spreader beam bolt connection; (b) Bottom spreader beam connecting the base beam to the concrete floor with colts; (c) Foot stop angle section; (d) Connection of vertical rods to parallel base beams..... | 86 |
| Figure 4.26: Close up of (a) 50 mm Vertical LVDT sliding on a smooth Perspex surface; (b) Load cell taking prestress measurement at bottom of vertical rods. | 86 |
| Figure 4.27: Shear wall specimen free body diagram. | 88 |
| Figure 5.1: (a) Rod forces vs horizontal displacement; (b) Sum of rod forces vs vertical displacement. | 92 |
| Figure 5.2: (a) Sum of rod forces and shear force vs horizontal displacement; (b) Vertical vs shear force..... | 93 |
| Figure 5.3: (a) Shear and vertical force vs horizontal displacement of SW-220-15-No Strips specimen and (b) compared to the results obtained by De Beer, (2016)..... | 94 |
| Figure 5.4: SW-220-15-No Strips crack pattern in the masonry..... | 95 |
| Figure 5.5; SW-220-15-No Strips (a) localised crack with crack pattern/width outlined; (b) enlarged photograph..... | 95 |
| Figure 5.6: Shear and vertical force vs horizontal displacement of SW-75-150-01 specimen. | 96 |
| Figure 5.7: SW-75-150-01 crack pattern in the masonry..... | 97 |
| Figure 5.8: SW-75-150-01 (a) localised crack with crack pattern outlined; (b) enlarged photograph; (c) enlarged photograph focussing on crack distribution. | 97 |
| Figure 5.9: Shear and vertical force vs horizontal displacement of SW-75-150-02 specimen. | 98 |
| Figure 5.10: SW-75-150-02 crack pattern in the masonry..... | 99 |
| Figure 5.11: SW-75-150-02 (a) Crack patterns during different cracking patterns outlined; (b) bottom enlarged photograph; (c) top enlarged photograph; (d) delamination..... | 99 |
| Figure 5.12: Shear and vertical force vs horizontal displacement of SW-100-200-01 specimen. | 100 |
| Figure 5.13: SW-100-200-01 crack pattern in the masonry..... | 101 |
| Figure 5.14: SW-100-200-01 (a) Crack patterns outlined; (b) delamination in bottom right corner. . | 101 |
| Figure 5.15: SW-100-200-02 2 cm horizontal grooves at (a) top and (b) bottom..... | 102 |
| Figure 5.16: Shear and vertical force vs horizontal displacement of SW-100-200-02 specimen. | 103 |
| Figure 5.17: SW-100-200-02 crack pattern in the masonry..... | 104 |
| Figure 5.18: SW-100-200-02 crack patterns outlined..... | 104 |
| Figure 5.19: Crack spacing..... | 105 |
| Figure 5.20: Summary of shear walls shear force vs displacement results..... | 106 |
| Figure 5.21: Shear force vs displacement with indicated energy at a 200 kN force..... | 108 |
| Figure 5.22: Horizontal forces for determining ECF of SW-75-150-01..... | 108 |
| Figure 5.23: Horizontal forces for determining ECF of SW-75-150-02..... | 109 |
| Figure 5.24: Horizontal forces for determining ECF of SW-100-200-02..... | 111 |
| Figure A.6.1: SW110-0 Principle strain (E1) diagams..... | 122 |
| Figure A.6.2: SW330-0 Principle strain (E1) diagrams..... | 123 |

| | |
|---|-----|
| Figure A.6.3: SW110-0 Principle vertical stress (S_2) and compressive stress (S_{yy}) diagrams. | 123 |
| Figure A.6.4: SW330-0 Principle vertical stress (S_2) and compressive stress (S_{yy}) diagrams. | 124 |
| Figure A.6.5: SW220-10 Principle strain (E_1) diagrams. | 125 |
| Figure A.6.6: SW220-10 Principle vertical stress (S_2) and compressive stress (S_{yy}) diagrams. | 125 |
| Figure A.6.7: SW110-10 Principle vertical stress (S_2) and compressive stress (S_{yy}) diagrams. | 127 |
| Figure A.6.8: SW110-15 Principle vertical stress (S_2) and compressive stress (S_{yy}) diagrams. | 127 |
| Figure A.6.9: SW330-10 Principle strain (E_1) diagrams. | 128 |
| Figure A.6.10: SW330-30 Principle strain (E_1) diagrams. | 128 |
| Figure A.6.11: SW330-10 Principle vertical stress (S_2) and compressive stress (S_{yy}) diagrams. | 129 |
| Figure A.6.12: SW330-30: Principle vertical stress (S_2) and compressive stress (S_{yy}) diagrams. | 129 |
| Figure B.6.13: Storage of shear walls in structure lab. | 130 |
| Figure B.6.14: Cracked shear wall specimen. | 131 |

List of Tables

| | |
|---|-----|
| Table 2.1: Richter magnitude and MMI comparison for expected South African seismic events (Saradj, 2007). | 4 |
| Table 2.2: PVA-fibre properties adopted from Stander (2007). | 16 |
| Table 2.3: SHCC mix for spray-ability adopted by De Beer (2016). | 17 |
| Table 2.4: Tensile behaviour of casted SHCC compared to sprayed SHCC (De Beer, 2016). | 19 |
| Table 3.1: Masonry Rankine-Hill material properties input. | 35 |
| Table 3.2: Smearred rotating crack material model input. | 36 |
| Table 3.3: Load combinations. | 38 |
| Table 3.4: Notations of computational models. | 44 |
| Table 3.5: Peak shear force with its corresponding displacement values of shear wall with no retrofitting overlay. | 45 |
| Table 3.6: Summary of computed and experimental tests on shear walls with and without SHCC overlay. | 60 |
| Table 4.1: SHCC mix proportions adopted from De Beer (2016). | 71 |
| Table 4.2: Mortar mix proportions. | 76 |
| Table 5.1: Compressive strength of mortar specimens. | 90 |
| Table 5.2: Experimental tests maximum shear and vertical forces and stresses with its associated displacements. | 106 |
| Table 5.3: ECF factor of SW-75-150-01. | 109 |
| Table 5.4: ECF factor of SW-75-150-02. | 109 |
| Table 5.5: Average ECF of specimens with 75 mm strips. | 110 |
| Table 5.6: ECF factor of SW-100-200-02. | 111 |

Abbreviations

| | |
|-----------|--|
| ASTM | American Society for Testing and Materials |
| C | Cement |
| CAC | Calcium Aluminate Cement |
| CBM | Cement-Based Materials |
| CFRP | Carbon Fibre Reinforced Polymer |
| CoV | Coefficient of Variance |
| DIANA | Displacement Analyser Software |
| DTT | Direct Tensile Tests |
| ECC | Engineered Cement-based Composite |
| E-Modulus | Modulus of Elasticity |
| FA | Fly Ash |
| FEA | Finite Element Analysis |
| FEM | Finite Element Method |
| FRC | Fire Reinforced Concrete |
| FRP | Fibre Reinforced Polymer |
| GGCS | Ground Granulated Corex Slag |
| HPC | High-Performance Concrete |
| HPFRCC | High-Performance Fibre Reinforced Cement Composite |
| LC | Load Cell |
| LVDT | Linear Variable Differential Transformer |
| MTM | Materials Testing Machine |
| NSM | Near Surface Mounted |
| OPC | Ordinary Portland Cement |
| PVA | Polyvinyl-alcohol |
| RC | Reinforced Concrete |
| SABS | South African Bureau of Standards |
| SANS | South African National Standard |
| SCC | Self Compacting Concrete |
| SHCC | Strain Hardening Cement based Composite |
| SUN | Stellenbosch University |

| | |
|------|-----------------------------------|
| SP | Superplasticiser |
| SW | Shear Wall |
| SWS | Shear Wall Specimen |
| TCB | Top Concrete Beam |
| TW | Testing Wall |
| UHPC | Ultra-High-Performance Concrete |
| ULM | Unreinforced Load-bearing Masonry |
| URM | Unreinforced Masonry |
| UTT | Uni-axial Tensile Tests |
| VA | Viscous Agent |
| w/b | water binder ratio |

Chapter 1

Introduction

Masonry is a widely used building material in South Africa. Unreinforced load-bearing masonry (ULM) is mostly used for the construction of houses, office buildings and apartments rising not higher than four stories. Masonry structures are known for their good resistance to gravitational loads due to the high compressive resistance of masonry but to have a poor performance during lateral loading regimes due to its low tensile resistance and brittle in-plane shear failure characteristics. Such lateral loads are caused when the building is subjected to seismic activity caused by earthquakes.

The Cape Town region of South Africa is categorised as a low to moderate seismic region. Seismic design requirements were only introduced in South Africa in 1989, which implies that ULM buildings constructed prior to this are in danger of in-plane shear failure during a design level seismic event. When ULM structures are subjected to seismic loads, predominant cracks are observed on the diagonal during brittle in-plane shear failure. This has inspired the development of retrofitting techniques for enhanced performance during such events.

Strain Hardening Cement-based Composite (SHCC) is a potential retrofitting material designed to increase the ductility of retrofitted ULM structures. It is able to reach significant strains of 3-6% when subjected to tensile loads, compared to the roughly 0.01% ultimate tensile strain of normal concrete. The material contains 2% randomly distributed PVA fibres, enabling a unique strain-hardening response after initial crack formation due to its crack bridging capability. The high tensile strains obtained by SHCC while retaining full or even increased tensile resistance, makes it an ideal retrofitting material in seismic regions, providing enhanced ductility and overall structural performance after failure of the masonry mortar joints or units.

The spraying of an SHCC overlay on ULM structures as a retrofitting technique to increase the overall structural performance, with primary focus on the ductility of the structure, has been examined by researchers at Stellenbosch University, as well as internationally. However, more research is still needed to obtain a better understanding of the failure mechanisms in this material and to improve its in-plane shear performance. A good bond between the masonry and SHCC interface is necessary to ensure that the strain-hardening behaviour of the SHCC is utilized, and that delamination of the overlay is limited due to the occurrence thereof leading to brittle failure.

SHCC material development to optimize its fresh material properties for favourable shotcrete application has previously been performed at Stellenbosch University. Large scale tests have been

performed on masonry walls with and without SHCC overlay to obtain the enhanced shear performance thereof.

This thesis performs finite element analysis of De Beer's walls' behaviour, after calibration to capture the correct failure mechanisms, and obtain reasonable agreement with global shear force-lateral displacement response. The calibrated computational model is subsequently used to predict further ductility improvement by applying debonded strip interfaces. Finally, the computed shear response of strip-bonded SHCC retrofitted overlay is validated by laboratory experiments.

1.1 Motivation

Engineers are responsible for complying with standardised design and construction requirements to ensure structural safety. With knowledge gained from work performed in the past on retrofitting building materials and earthquake events, one can progress with the research of obtaining a retrofitting technique to ensure the structural integrity of ULM buildings during seismic events. This study aims to advance the retrofitting strategy by performing nonlinear analysis with well-integrated software and performing validating laboratory experiments towards the development of further improvements.

1.2 Outline

The research proposal and motivation documented in this study originate from the need of retrofitting strategy development and improvement. The modelling approach with DIANA software for simulation and improvement, through to the design, construction, execution and interpretation of large scale validation tests on shear walls retrofitted with an SHCC overlay and debonded strip interfaces are reported in this thesis.

Chapter two discusses the theoretical background of seismic events, masonry behaviour, SHCC as retrofitting material and computational modelling based on the findings of various researchers.

Chapter three consists of a discussion of the computational theory and conceptualisation with models and tools available in the DIANA software for performing nonlinear analysis on masonry shear walls. The laboratory investigation performed by a former study with varying wall and overlay thickness is studied computationally and the computational results are compared with the experimental results to calibrate the computational model and model parameters.

Chapter four proposes the new debonding strip interface retrofitting technique, presents the computed response of such a retrofitted wall as prediction and describes the design setup and preparation of the validating laboratory shear walls.

Chapter five discusses the results and interpretations obtained from the laboratory shear wall tests towards validation of the new proposed strip-bonded overlay retrofitting strategy.

The final chapter draws conclusions and presents recommendations for further improvements and testing of the retrofitting technique. This is followed by the bibliography and appendices in which additional results and photographs are presented.

Chapter 2

Literature Review

2.1 Seismic activity in South-Africa

2.1.1 Introduction

A seismic event (earthquake) is defined as a geological event caused by energy traveling through the crust of the earth, causing movement of the ground. Most seismic events are naturally-induced due to tectonic plate movement, but human-induced causes include fracking or mining activities.

Magnitude and intensity are two different methods used to represent the severity of a seismic event. The magnitude is the quantity of energy contained by the seismic event, which can be measured using various techniques. The Richter scale is the most popular method of quantifying the magnitude of a seismic event. The intensity is understood as a measurement of the effect that the seismic event has on the environment, people and surrounding structures. The Modified Mercalli intensity scale (MMI) is an intensity measurement on a scale of I to XII, indicated by human observation and structural damage caused by an earthquake (Van Der Kolf, 2014). Additionally, recording the acceleration of the ground is used as a measurement to indicate the intensity of the seismic activity. The intensity caused by the same seismic event may differ between areas due to the different soil types in the areas. Different soil types play a significant role in how a seismic event is observed. A comparison of the Richter magnitude and MMI of expected seismic events in South Africa is given in Table 2.1.

Table 2.1: Richter magnitude and MMI comparison for expected South African seismic events (Saradj, 2007).

| Richter Magnitude | MMI | Description |
|--------------------------|------------|--|
| 4.0-4.9 | IV-V | IV. Felt indoors by many and outdoors by few. Walls make cracking sound and windows disturbed. |
| 5.0-5.9 | VI-VII | V. Felt by nearly everyone. Broken windows. VI. Felt by all and many frighten. Movement of heavy furniture. VII. Considerable damage in poorly designed structures, slight to moderate in well-built structures, and neglectable damage in well-designed buildings. |
| 6.0-6.9 | VIII-IX | VIII. Slight damage of well-designed buildings, and considerable damage in well-built buildings. IX. Considerable damage in well-designed structures. |

2.1.2 Structural seismic design considerations

The seismic zones considered to be applicable in South Africa, according to SANS 10160-4:2011 are shown in Figure 2.1. The ground accelerations and two types of zones for the different areas are identified:

- Zone I: demonstrates seismic events caused natural and
- Zone II: demonstrates human-induced and natural seismic events.

The Cape Fold Belt within the Western Cape has a $0.15g$ peak ground acceleration as shown in the seismic hazard map, and the seismic activity of the region is classified as low to medium. Structural design standards considering seismic loading were introduced to South African engineers for the first time in 1989 (SABS 0160:1989). The code was found to be conservative and the Eurocode (EN 1998-1, 2005) was therefore adapted to implement an updated version (SANS 10160-4:2011). Structures dated before 1989 need to be assessed and, if deemed unsafe, to be retrofitted as the seismic code requirements were not applied in their original design.

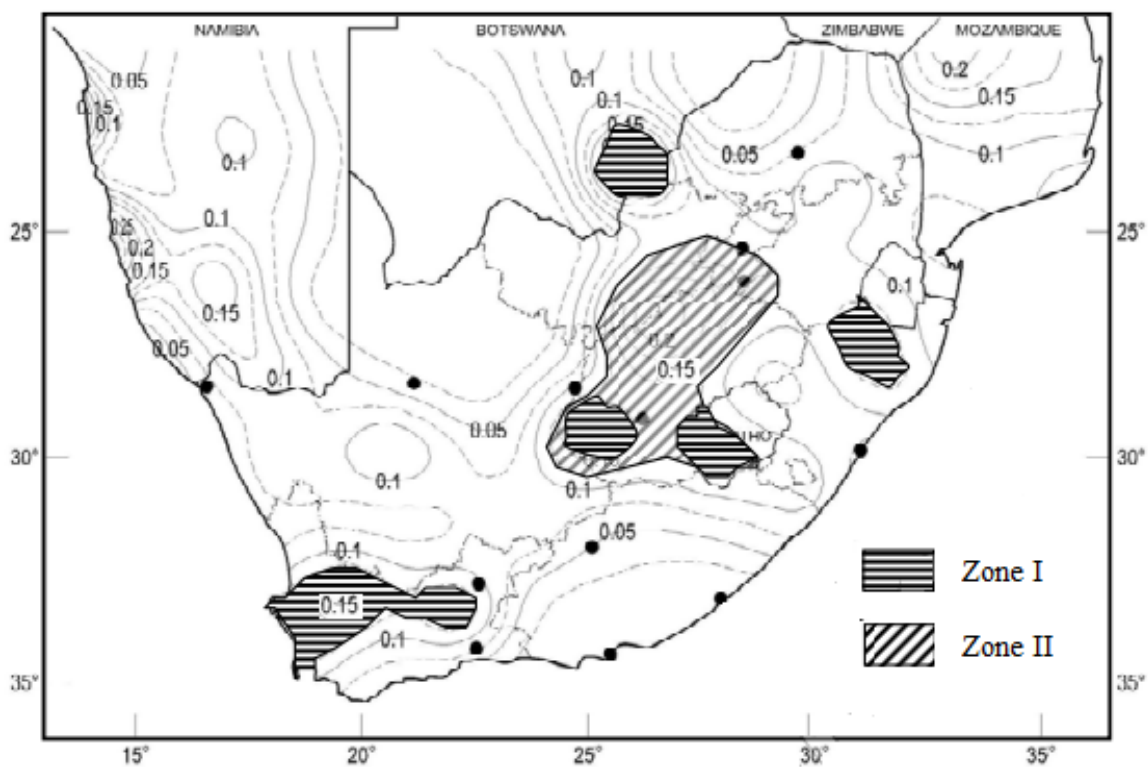


Figure 2.1: South African seismic hazard map with peak ground accelerations, 10% in 50 years exceedance probability (SANS 10160-4, 2011).

2.2 Masonry

Masonry has been widely used as building material in South African buildings due to its relatively low cost. Three main structural categories are used to classify masonry elements, namely: confined, reinforced and un-reinforced. Reinforced masonry structures are more resilient than unreinforced masonry (URM) structures during seismic loading due to their superior resistance to lateral forces and their capacity to transmit tension (eg. Van Der Kolf, 2014). Additionally, it ensures higher ductility by allowing larger deflections before element failure. Ductility increases the seismic resistance of a structure, because horizontal accelerations and displacements are the main actions caused by a seismic event.

2.2.1 Unreinforced Masonry (URM) buildings

Key aspects to consider when designing URM structures according to SANS 10160-4:2011 are discussed here.

The multi-story URM structures situated in the Western Cape consist of calcium-silica, baked clay, or concrete units. The scope of this thesis is limited by focusing solely on masonry consisting of clay brick units. Concrete units will, however, be taken into consideration and tested in the research group in the future, due to the high prevalence of this building unit locally.

URM structures are mostly similar, making load path prediction and failure mode anticipation easier. Known load paths simplify the retrofitting work of designers as only critical elements need to be retrofitted to ensure structural safety. Simple and uniform structures are guiding principles. Structural redundancy refers to an increased number of mechanisms of resistance added to a structure by additional elements. Such additional resistance will be provided to URM structures in the case of seismic loads by shear walls.

URM structures should have the required resistance to withstand horizontal forces in all directions as the ground motion caused by seismic activity occurs in any direction. Horizontal forces are transmitted into the shear walls during seismic activity by roofs and floors which act as diaphragms in the horizontal direction. It is essential for connections to be sufficient and in-plane floor stiffness to be adequate (eg. Van Der Kolf, 2014).

URM structures are characterised as brittle with low ductility under seismic loading as the design thereof is prior to the SANS 10164-1:1989 implementation. A study conducted by Bruneau (1994) demonstrated that URM structures have a high risk of failure under seismic loading. However, further studies showed that well-designed URM structures with effective energy dissipation and connections can resist seismic loading. Thus, there is a need for these historic structures to be evaluated for their resistance during seismic events.

Structural ductility allows higher deflection and wide-spread cracking of the walls while maintaining resistance to the vertical load during lateral acceleration and displacement caused by a seismic event (eg. Van Der Kolf, 2014). Energy dissipation takes place while the wall is in the process of deflecting and cracking. The process repeats itself until a failure mechanism forms which causes the element to collapse. If a failure mechanism forms within a critical element of the structure, global collapse may occur, which must be prevented by appropriate design for seismic resistance.

Structural elements of an URM structure are designed to transmit loads to the foundation following a certain path. Elements along this path must be able to resist the forces and deformations they may be subjected to. Failure can occur within structural elements, or in connections if not properly designed and constructed. Thus, it is important to ensure that connections between walls and floors have the adequate capacity to resist the loads and deformations they are subjected to. Global collapse may occur if the capacity of a critical connection or structural element is exceeded.

URM structures have a sufficient ability to withstand upper story vertical loads. Primarily designed floors (diaphragms) transmit lateral loads, from lower stiffness elements into shear walls with adequate stiffness, resisting the loads in-plane as shown in Figure 2.2. Thus, effectively connected shear walls with sufficient capacity are necessary to transfer loads into the foundation. Structural elements will be subjected to out-of-plane deflection when a force is applied perpendicular to its face. Floors and horizontally braced walls transmit these forces into shear walls, which are then distributed into the foundation.

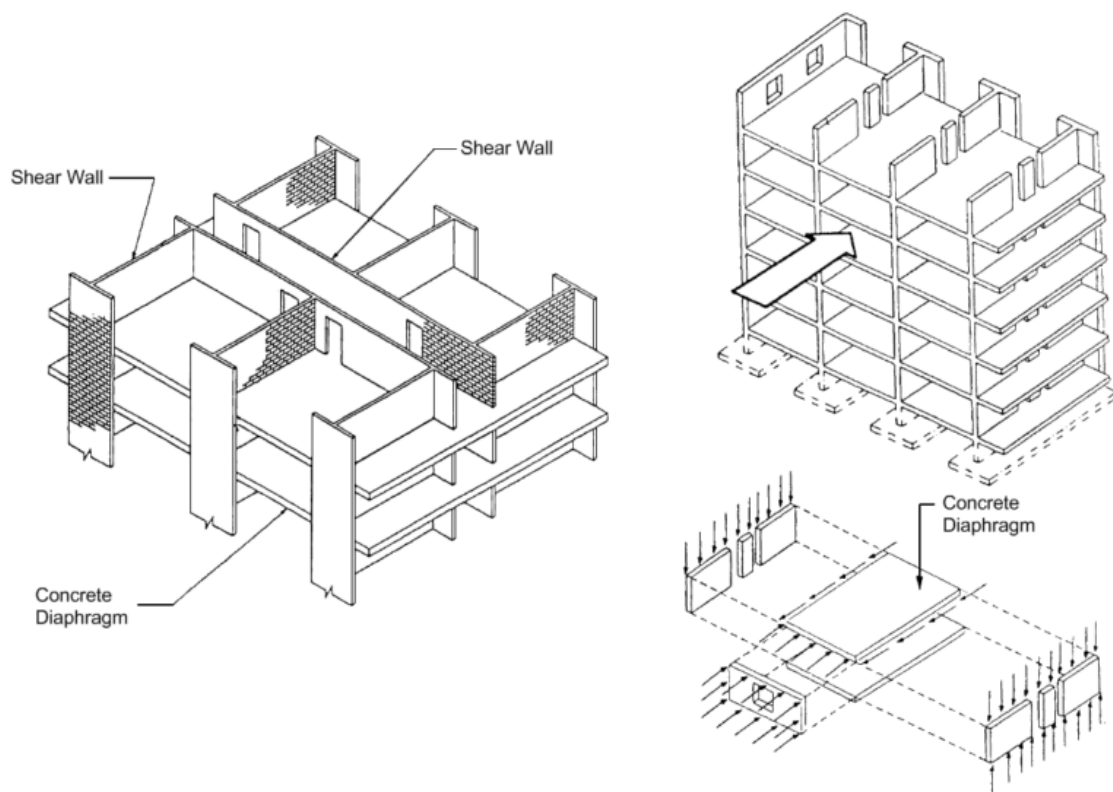


Figure 2.2: URM structural load path system (eg. Van Der Kolf, 2014).

2.2.2 Failure modes of URM shear walls

New Zealand is a country with high seismicity as it is located at the boundary between the Australian Plate and the Pacific Plate. The vulnerability of New Zealand URM buildings during seismic events has been clearly demonstrated in a number of previous earthquakes with the 1931 M7.8 Hawke's Bay earthquake and more recently in the 2010 M7.1 Darfield earthquake and 2011 M6.3 Christchurch earthquake being responsible for causing the greatest extent of damage to URM buildings (Lin et al., 2014). The damage levels caused to the URM buildings in these seismic events included complete collapse (see Figure 2.3 (a)), individual walls collapsing completely or partially out-of-plane for seismic loading oriented perpendicular to the walls (see Figure 2.3 (b)); or varying damage levels, including diagonal shear cracking in piers, when seismic loading was oriented parallel to the wall (see Figure 2.3 (c)).

Multi-leaf construction is typically used to compose URM bearing walls, with wall thickness of 2 and 3 leaf being the most common, although single leaf thick walls are also observed, typically as part of cavity wall construction (Lin et al., 2014). Wall thickness exceeding 3 leaf are also encountered and tend to be used more commonly in URM buildings having a height exceeding two stories.



a) Damage caused by the 1931 M7.8 Hawke's Bay earthquake



b) Collapse of out-of-plane loaded URM walls in the 2010 M7.1 Darfield earthquake



c) In-plane diagonal cracks caused by the 2011 M6.3 Christchurch earthquake

Figure 2.3: Examples of damage to New Zealand URM buildings as a result of seismic loading.

The in-plane and out-of-plane actions, induced by the lateral movement of a seismic event, cause various failure modes in URM structures. Seismic observations and studies have distinguished modes of in-plane and out-of-plane failure due to insufficient anchorage and floor related failures. The in-plane shear walls resist horizontal forces as they have a significantly higher in-plane stiffness and strength compared to their out-of-plane stiffness and strength. Only in-plane failure mechanisms of the shear walls will be discussed in this thesis, but it is acknowledged that the out-of-plane response of elements during seismic action must safely accommodate the deformation demand of the event as transmitted by the in-plane structural elements. The failure mechanisms considered are shown in Figure 2.4.

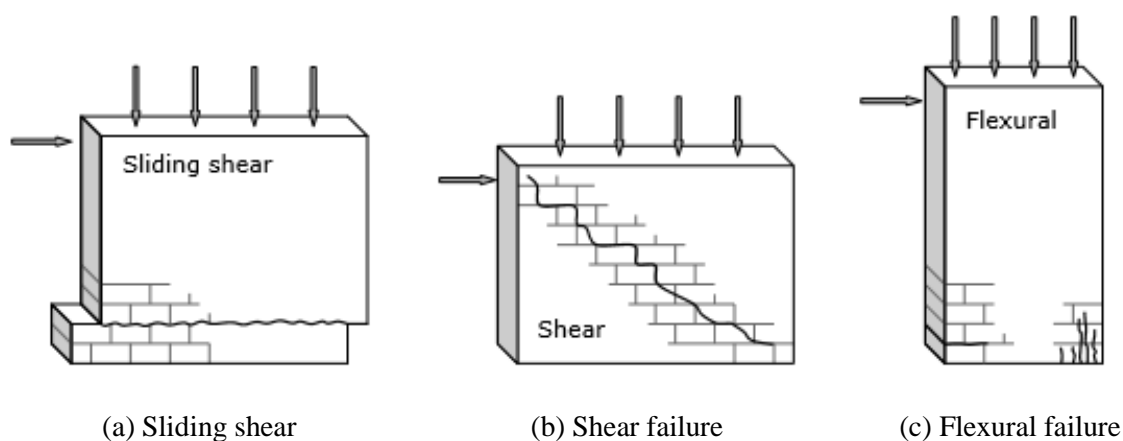


Figure 2.4: In-plane mechanisms of failure of URM shear walls (Tomazevic, 1999).

Shear walls can undergo sliding shear failure when the vertical loads are insignificant, and the mortar bonding strength is low. Shear failure (diagonal tensile failure) is a result of the tensile capacity of the masonry being outweighed by the principle stresses and the mortar having a low bond and shear resistance. Flexural failure (toe crushing and flexural cracking) occurs when the wall has sufficient shear capacity, but the high flexural tensile and compressive zones at the faces of the wall cause the masonry to crack and crush.

2.3 Retrofitting of URM buildings

Retrofitting is a structural intervention that intends to increase the resistance of a building. The purpose of retrofitting is to improve the structural performance and integrity of a building by enhancing the strength, ductility, corrosion protection, as well as its aesthetic appearance and serviceability. This subsection discusses the retrofitting techniques used to enhance the in-plane shear behaviour of URM structures.

2.3.1 Carbon Fibre Reinforced Polymer (CFRP) strips

A study was conducted by Van Zijl et al. (2005) on the enhancement that CFRP strips will have on masonry wall cracking and structural serviceability. The strips are applied as external reinforcement to the URM structures. Placing the strips in different directions and patterns, ensures deformation control by redistributing or eliminating shrinkage cracks. Although the structural safety is not influenced by these cracks, the serviceability can be impaired (Van Zijl and De Vries, 2005). Negative aspects of this retrofitting method are that delamination may occur when subjected to high sustained loads and its aesthetic appearance is unpleasing. Van Zijl et al. (2005) noted that the strips will be equally effective

in preventing single, large crack widths from arising when applied on the inside face of the wall. It must, however be noted that larger crack widths occur on the non-reinforced side than on the reinforced side, ascribed to the eccentric application of the CFRP reinforcement. This may not fully address the displeasing appearance of the wide cracks on the exterior of the internally retrofitted walls.

2.3.2 Near Surface Mounted (NSM) reinforcement including steel mesh

ElGawady et al. (2006) conducted studies on the improvement that NSM overlays will have on URM structures. The retrofitting system entails that a reinforcement mesh (sometimes mechanically anchored to the outer face of the masonry) is covered with shotcrete using a spraying nozzle as shown in Figure 2.5. A significant quantity of shotcrete run off occurs during the spraying process, leading to unnecessary costs.



(a) CFRP strips



(b) NSM with steel mesh reinforcement

Figure 2.5: URM shear walls in-plane retrofitting techniques adopted from Van Zijl et al. (2005) and ElGawady et al. (2006).

2.3.3 SHCC bonded overlays

Lin et al. (2014) and De Beer (2016) have conducted various tests using Strain Hardening Cement based Composite (SHCC) bonded overlays for the retrofitting of masonry and demonstrated the enhancements they provide to shear walls. Lin et al. (2014) demonstrated that on average, the ductility of the in-plane shear response is increased by up to 220% with the application of SHCC as a bonded overlay compared to shear walls, while the shear strength also showed a promising increase between 130% and 510% for the different wall and overlay thicknesses included in their study. The strengthening effects are dependent on the wall and overlay thickness, and their results showed that the strength and ductility enhancement diminished beyond a threshold layer thickness.

The overlays are considered to be ideal due to their significant enhancement of mechanical behaviour, acceptable aesthetic appearance, and relatively simple application. Section 2.2 addressed the need for retrofitting of URM structures due to their brittle response during seismic events. The findings of Lin et al. (2014) were based on a non-optimised shotcrete overlay, and could possibly be improved significantly by improving the material to the level that De Beer (2016) achieved.

2.4 Strain Hardening Cement-based Composites (SHCC)

SHCC is a class of High-Performance Fibre-Reinforced Cement-based Composites (HPFRCC) with ultra-high ductility, which exhibits pseudo strain hardening behaviour during uniaxial tensile loading (Van Zijl et al., 2012). SHCC can undergo large deformations after cracks have formed whilst the tensile resistance is maintained or increased. SHCC can effectively resist tensile strain of more than 3% and in some cases up to 6%, when it is properly designed (De Beer, 2016). This behaviour is due to the crack-bridging ability of the fibres that leads to the formation of multiple fine cracks that are tightly spaced. This crack control behaviour causes significant energy dissipation, whereby it affords ductility and damping to URM buildings during seismic events.

2.4.1 SHCC tensile behaviour

The ductility of SHCC stems from its ability to maintain or increase strength after cracks have formed. In contrast, standard or typical fibre reinforced concrete (FRC) has a strength decrease as the strain increases after initial crack formation, displaying its strain softening behaviour. Van Zijl et al. (2012) describes the highly ductile characteristics of SHCC leading to multiple cracks, which are typically invisible to the naked eye, being formed in a widely spread pseudo-plastic area. FRC generally forms larger localised cracks in weak regions of the structural element or in regions subjected to maximum internal forces.

The typical stress-strain behaviour for the different classes of HPFRCC materials is shown graphically in Figure 2.6 (a), and the crack width control exhibited by the SHCC material is displayed in Figure 2.6 (b). Figure 2.6 (a) contrasts the SHCC strain-hardening behaviour with the strain-softening behaviour of the UHPFRC. The strain-hardening response process is due to crack initiation at the weakest position in the SHCC matrix subjected to direct tensile force. The crack is bridged by fibres with higher capacity than that of the matrix. By increasing the strain, the structural element will be subjected to larger internal forces which will cause cracking of the next weak position in the matrix. This crack-bridging process continues to a point where the ultimate bridging capacity of the fibres at any position is breached, which causes the formation of a localised crack and strain-softening. Standard FRC starts to strain-soften after the formation of the initial crack due to the fibre-bridging capacity being breached by the force forming

the initial crack within the matrix. As the strain increases beyond the first cracking strain, the width of the localised crack increases while stress decreases.

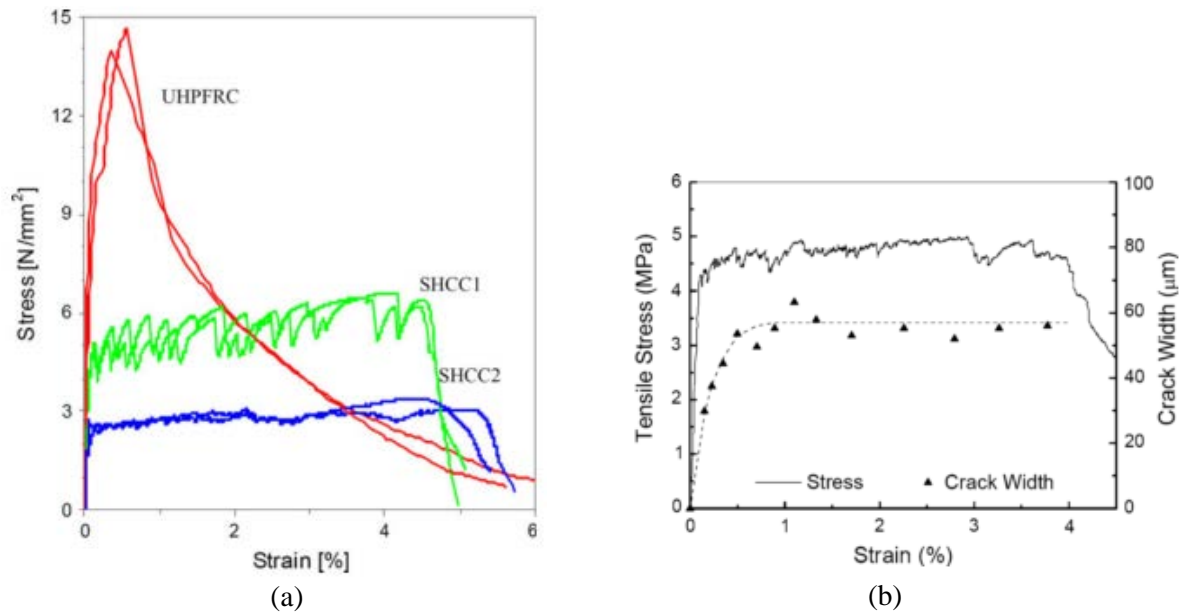


Figure 2.6: (a) Stress-strain behaviour of HPRC materials subjected to uniaxial tensile forces and (b) crack width control exhibited by SHCC adopted from Van Zijl et al. (2012).

The behaviour of SHCC during unloading and reloading is important due to the cyclic motion caused by seismic events. Boshoff and Van Zijl (2007) performed tests at Stellenbosch University (SUN) showing the tensile behaviour of SHCC when subjected to cyclic loading. It was observed that with an increasing tensile strain, the SHCC stiffness decreased during this cyclic loading regime, but its ultimate strength and strain are not significantly affected. The decreasing stiffness property is favourable when URM structures are subjected to seismic loading, as a higher fundamental period will be obtained for the structure, leading to a decreased shear force within the base. Energy dissipation will continue during each loading cycle and the ultimate stress and strain capacity will be maintained. The tensile behaviour of SHCC during unloading and reloading is displayed in Figure 2.7.

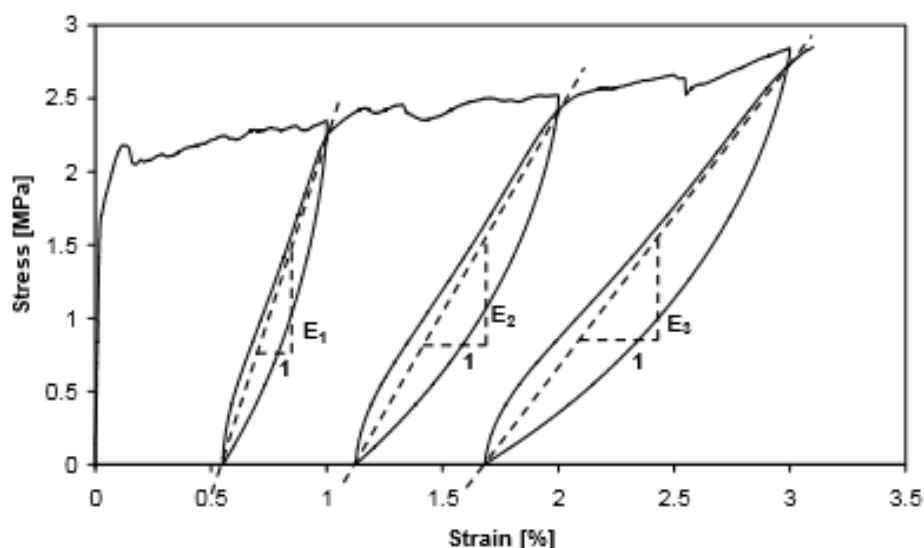


Figure 2.7: Tensile response of SHCC when subjected to cyclic loading (Boshoff and Van Zijl, 2007).

2.4.2 SHCC flexural behavior

Dehghani et al. (2013) performed four-point bending tests on masonry beams according to ASTM E518-10 to evaluate the flexural performance of SHCC material on masonry panels. Ten bricks and nine mortar joints of 10 mm were used to construct the masonry beams vertically. The bricks were grinded on all load bearing faces before the specimens were constructed for full contact to be obtained between the load-applying blocks and supports and the specimen. This is essential to avoid premature shear failure in the mortar joints close to the loading points and supports due to the load concentration resulting in high shear stress (Dehghani et al., 2013).

The test setup and flexural response of the masonry panels are shown in Figure 2.8. One plain specimen, three specimens containing 20 mm SHCC on its tensile face, and three specimens with 20 mm SHCC layer connected to the tensile face with the use of a construction adhesive bonding agent were tested at a 0.3 mm/min displacement control rate. The load was applied by a 100 kN capacity Instron testing machine. Two LVDTs were located under the midspan mortar joint to record the midspan deflection.

From the load-displacement curves shown in Figure 2.8, it can be observed that the flexural strength and ductility increased significantly when SHCC is applied compared to the bare plain specimen. An ultimate load capacity of 5 kN with an associated midspan deflection of 0.2 mm was obtained by the plain specimen. The specimens retrofitted with SHCC overlay observed initial cracking in the overlay at an average strength of 20 kN which is four times more compared to the plain specimen. The ultimate strength obtained by these specimens was higher than the strength of initial cracking and multiple crack formation in the overlay was observed in the inelastic zone. The ductility increased by a factor of 25-30, emphasising on the strain-hardening behaviour exhibited when SHCC overlay is applied.

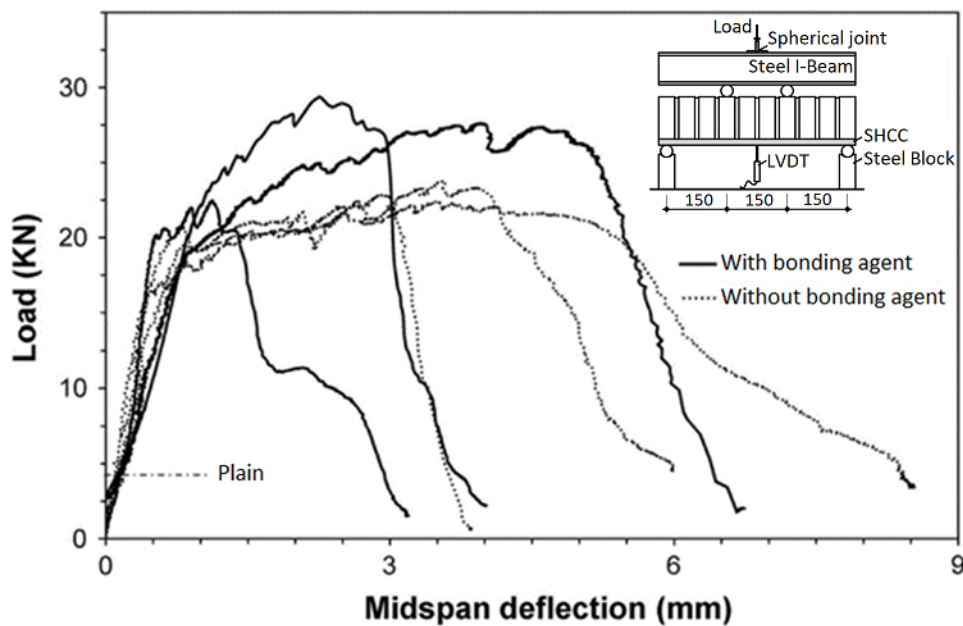


Figure 2.8: Four-point bending test setup and flexure response conducted by Dehghani et al. (2013).

2.4.3 SHCC shear behaviour

Van Zijl (2007) conducted tests on the SHCC shear response, using the Iosipescu shear beam as shown in Figure 2.9 (a). The diagonal strain displayed in Figure 2.9 (b) was measured by placing a Linear Variable Differential Transformer (LVDT) at an angle of 45° over a central strain gauge length of 25 mm. Specimens with different fibre volumes were tested, and diagonal failure was observed for specimens with fibre volume less than 2%, while multiple cracking occurred in the notch area for specimens with fibre volume of 2% and above. The SHCC showed a 50% higher ultimate shear capacity compared to ultimate tensile capacity, which is due to its ability to maintain its tensile resistance beyond crack initiation, allowing the compressive stress to be increased and principle stress rotation (Van Zijl, 2007).

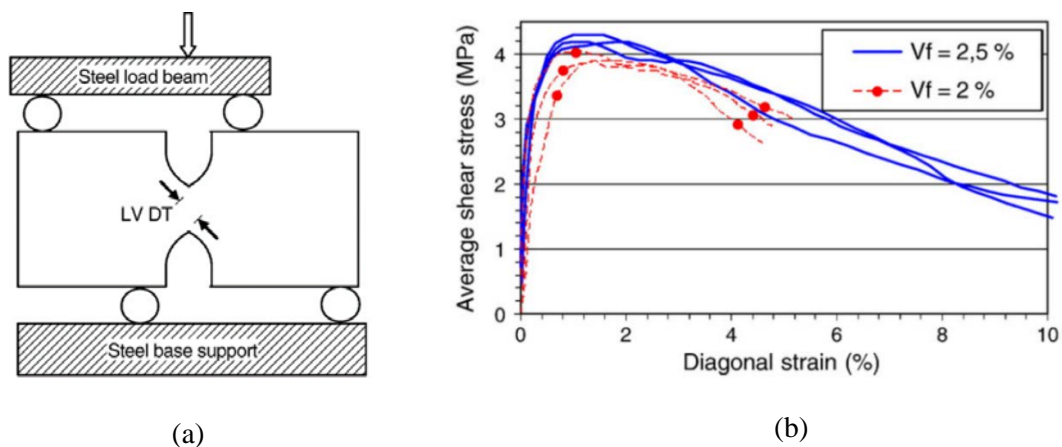


Figure 2.9: (a) Iosipescu shear beam test and (b) shear behaviour of SHCC adopted from Van Zijl (2007).

2.4.4 Compressive behaviour

The SHCC mixtures developed in this research have a cube compressive strength ranging between 20 and 40 MPa, while Wang et al. (2006) developed mixtures with 50 MPa + strengths. SHCC has a similar compressive behaviour to that of concrete with linear elastic behaviour roughly up to 30% to 50% of the ultimate strength and the subsequent reduced stiffness. The peak compressive strength is typically achieved at a larger compressive strain than in normal concrete, and the subsequent softening is less steep due to fibre bridging of splitting cracks (Visser, 2007).

2.4.5 Elastic modulus (E)

The elastic modulus of a SHCC mix is highly dependent on the type, size, volume of the aggregate used (Van Zijl et al., 2005) and air content (Visser, 2007). De Beer (2016) applied the secant method to the results of the direct tensile test to determine that the elastic modulus of normal SHCC ranges from 14-20 GPa. For full computation and formulation of the secant method, the user is referred to De Beer (2016).

2.4.6 Properties of the matrix constituents

The SHCC matrix typically consists of the same ingredients as concrete, namely sand, water, binder, fibres and chemical admixtures. It is, however, necessary to obtain the optimal ratio of these constituents in order to achieve the high ductility of SHCC material. The SHCC matrix contains no coarse aggregate as it impacts on the ductility performance due to the fracture toughness being increased by coarse aggregate. The distribution of fibres and their ability to bridge cracks are also reduced by the presence of coarse aggregate.

Curosu et al. (2016) showed that a higher loading rate leads to increased fibre bonding strength, which may in turn cause a less ductile tensile response of the matrix-fibre interface. Thus, the geometrical and mechanical characteristics of the matrix, fibres and matrix-fibres interface are important to obtain optimal proportioning which will ensure a ductile SHCC material.

2.4.6.1 Fibres

Polyvinyl Alcohol (PVA) fibres are used in SHCC research at SUN. These high-tensile capacity fibres enable the strain-hardening behaviour discussed in Section 2.4.1. It is important to obtain a fibre-matrix combination that allows gradual fibre-slip and pull-out, which prevents fibres from rupturing and the consequential brittle fracture of the composite. Slipping is more likely to occur with the use of short fibres due to its shorter bonding length.

Fibres with a 12 mm length are commonly used due to their ability to disperse well. For the aim of this research however, a fibre length of 8 mm is used to allow for a favourable spray-ability and pumpability as discussed in Section 2.5. The properties of the PVA fibres used in this research are shown in Table 2.2.

Table 2.2: PVA-fibre properties adopted from Stander (2007).

| Type | Diameter (mm) | Length (mm) | $f_{t,f}$ (GPa) | E (GPa) | $\epsilon_{u,f}$ (%) |
|-----------|---------------|-------------|-----------------|---------|----------------------|
| PVA-REC15 | 0.04 | 8 | 1.6 | 37 | 6 |

2.4.6.2 Binder, Additives and Fine Aggregate

The binder used by De Beer (2016), consists of a combination of fly-ash (FA) and Portland Cement (CEM I 52.5 N). Superplasticiser (SP) and methyl cellulose, also known as Viscous Agent (VA), are used as additives in this research to increase the fresh and hardened state performance. The SP chemical ensures a higher workability while the VA prevents bleeding and segregation, assisting in achieving uniform fibre dispersion. Both these admixtures are added during the mixing. Fine silica sand is used as the fine aggregate in this research, following De Beer (2016) and Paul and Van Zijl (2014) at SUN. The well-graded sand with a maximum particle size of 0.2 mm, leads to better matrix compaction and reduces the matrix fracture toughness. The reduction of the matrix toughness leads to strain-hardening behaviour.

2.5 Development of a sprayable SHCC mix

Shotcrete is the process by which a pump and high-pressure nozzle is used to project a retrofitting composite onto a substrate, in this case a masonry wall, at a high velocity. Shotcrete can be pumped through a hose to the nozzle in a wet or dry state. When dry concrete is conveyed through the hose, air and water are applied at the nozzle. This process is typically used in mining and slope stabilisation applications and is not discussed in this thesis. The following section discusses the development of a sprayable SHCC mixture. This wet-mixture is favourable for the shotcrete process of SHCC.

2.5.1 Considerations for a sprayable mix

The rheological and micro-mechanical characteristics need to be carefully considered for a SHCC mixture for it to be successfully sprayed onto masonry in its fresh state in order to maintain its strain-hardening properties in the hardened state. The rheological aspects need special attention for the mixture to be sprayed successfully. Kim et al. (2004) were the first researchers to conduct studies on the

adjustment of composite matrix to obtain its optimal rheological properties, while maintaining its ductile strain-hardening performance. The objective was to avoid segregation when the mix is pumped to the nozzle, and to increase its viscosity and cohesiveness after it has been sprayed on the masonry. These qualities of high viscosity and cohesion avoid segregation and runoff of the sprayed SHCC from the substrate.

Kim et al. (2004) focussed on controlling the initial deformation of the mixture by modulating the flocculation of the cement particles. The introduction of Calcium Aluminate Cement (CAC) as a SHCC constituent contributed to the deformation rate and controlled particle flocculation. Kim et al. (2004) conducted tests which enabled the rheological properties of a mix to be controlled in two phases. The initial phase allowed the mix to be pumped easily by increasing its deformability. The second phase starts after the SHCC is sprayed on the masonry. During this phase, the particle flocculation rate increases, allowing the deformability to decrease by enhancing the viscosity.

2.5.2 Adopted sprayable mix

De Beer (2016) adopted the tests performed by Kim et al. (2004), to produce a SHCC mix with optimal enhanced rheological and micromechanical properties. The adopted mix is specifically designed to have high deformability during pumping, while maintaining its significant ductile behaviour and strain-hardening response when subjected to tensile loading.

The constituents of the final mix produced by De Beer (2016) are shown in Table 2.3. The optimum FA/cement ratio is 140% and the CAC/cement ratio is 5%. PVA fibres, with properties shown in Table 2.2, are added at 2% total volume fraction to ensure crack bridging.

Table 2.3: SHCC mix for spray-ability adopted by De Beer (2016).

| Cement | Fly-Ash | CAC | Sand | Water | Fibres | SP | VA | Total (kg/m³) |
|---------------|----------------|------------|-------------|--------------|---------------|-----------|-----------|-------------------------------------|
| 420 | 620 | 21 | 540 | 365 | 2% | 2.2 | 0.8 | 1995 |

2.5.3 Direct Tensile Test (DTT)

De Beer (2016) performed two types of tensile tests similar to Boshoff (2007) (method 1) and Zang (2015) (method 2) for the determination of the ultimate tensile strength. Dumbbell shape moulds, with dimensions as shown in Figure 2.10 (b), were used to cast the SHCC specimens of method 1.

In method 1, the specimens were subsequently cured for 13 days, after which they were clamped at the bottom and top in a Zwick Z250 Universal Materials Testing Machine (MTM) as shown in Figure 2.10

(a). The bottom and top clamps constrain the specimens as fully fixed and pinned respectively. The MTM, with a tensile capacity of 250 kN, was set to induce a crosshead speed of 0.5 mm/min. An extensometer with dimensions shown in Figure 2.10 (b), was used to measure the strain.

Method 2 contained larger specimens than those of method 1. Dumbbell shaped specimens with a $d = 40 \text{ mm} \times w = 80 \text{ mm}$ cross-section and a 90 mm gauge length (l_g) were used. The same curing conditions as discussed in method 1 were used to cure the samples. Pneumatic clamps were used to clamp the edges of the sample to provide a fully fixed constraint shown in Figure 2.10 (d). More reproducible results were obtained from method 2. The reader is referred to De Beer (2016) for more details regarding the DTT.

The optimum CAC/cement and FA/cement ratios were obtained by performing a series of trial tests. The tensile capacity of SHCC was not significantly influenced by CAC. From the test results, a cement replacement by 5% CAC was selected, solely for successful spray-ability. The mix consisting of 140% fly-ash was selected for its significant strain capacity.

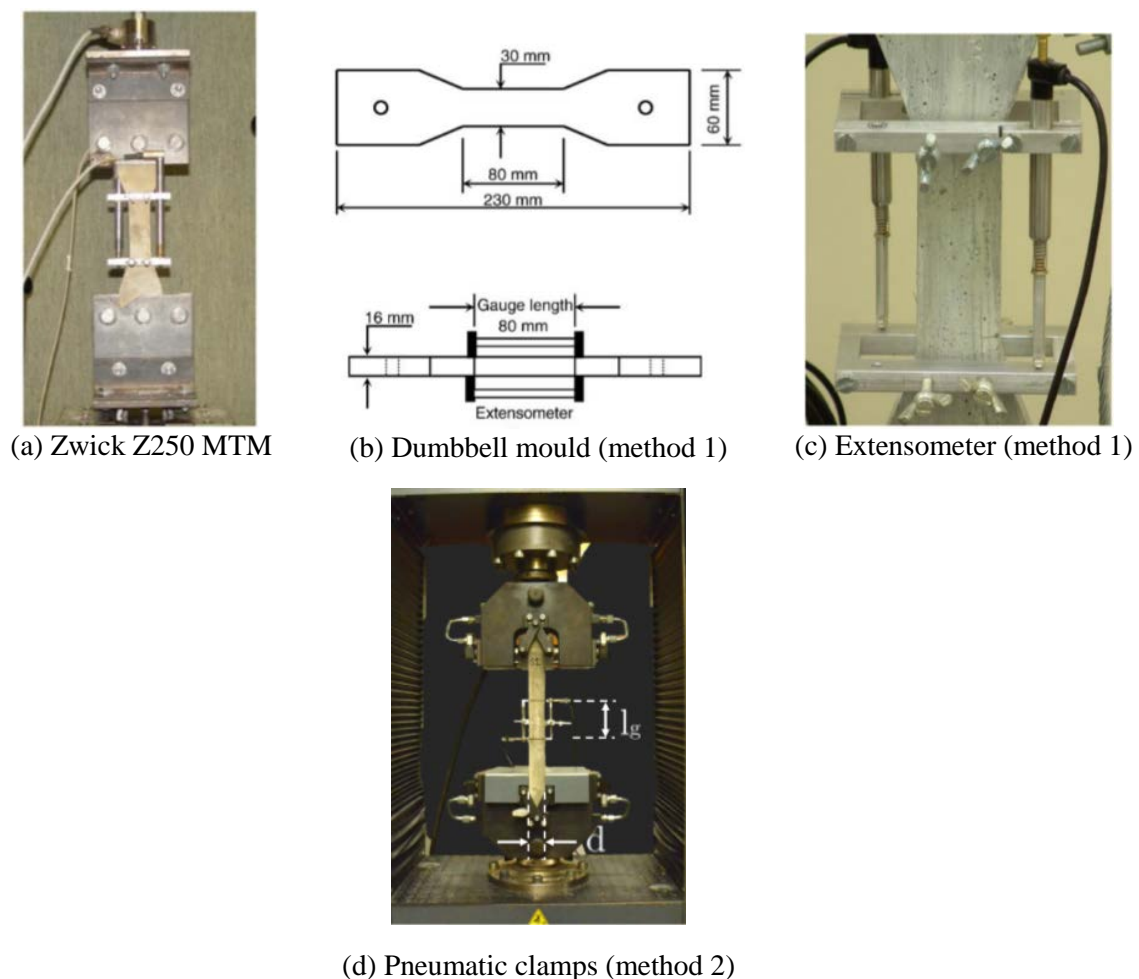


Figure 2.10: DTT adopted from Boshoff (2007).

2.5.4 Cast vs sprayed specimens

Table 2.4 summarises the DTT results by De Beer (2016), comparing the tensile behaviour of cast SHCC with sprayed SHCC. The sprayed SHCC showed a decrease in ultimate tensile capacity (f_{tu}) of 25.9%, while its tensile stress at crack initiation (f_c) decreased by 16.4%. The elastic modulus of the cast and sprayed SHCC showed similar results, while the ultimate tensile strain capacity decreased with 32.1% when sprayed. However, the 2.26% ultimate strain capacity of the sprayed SHCC is sufficient, as it will still pose a significant ductility increase for retrofitting applications.

Table 2.4: Tensile behaviour of casted SHCC compared to sprayed SHCC (De Beer, 2016).

| | No. of samples | f_c (MPa) | f_{tu} MPa | ϵ_u (%) | E (GPa) |
|----------------|----------------|-------------|--------------|------------------|---------|
| Cast | 3 | 2.62 | 2.97 | 3.33 | 15.25 |
| Sprayed | 8 | 2.19 | 2.2 | 2.26 | 15.27 |

2.6 Shrinkage

Shrinkage is caused by water loss from cement-based materials (CBM) due to the hydration process and/or the conditions of the surrounding environment, resulting in volume reduction (Alexander et al., 2009). This dimensional instability may cause stresses within the concrete matrix if it is restrained, which may result in shrinkage cracking and/or delamination. Thus, the characteristics of the CBM must be carefully considered in order to restrict this detrimental behaviour. In the section that follows, a discussion of shrinkage mechanisms is given, followed by the behaviour of retrofitting overlays when subjected to restrained shrinkage.

2.6.1 Shrinkage mechanisms

Both internal and external factors will have an influence on the rate and severity of shrinkage. The internal factors include the properties of the concrete constituents, while the external factors include the geometry of the concrete specimen and the conditions of the surrounding environment. Shrinkage can be categorised into four different types namely drying shrinkage, autogenous shrinkage, carbonation shrinkage and plastic shrinkage.

Drying shrinkage is a result of capillary moisture being lost through evaporation. This is caused by the temperature and humidity variations between the surrounding environment and the constrained concrete matrix. Autogenous shrinkage occurs at an early stage and is caused by the internal moisture being reduced due to its consumption for the hydration process to take place. Carbonation shrinkage occurs due to a reaction between carbon dioxide (CO₂) and hardened concrete, resulting in volume reduction.

This reaction takes place when the hardened cement paste is exposed to air containing CO₂. Plastic shrinkage occurs when the evaporation rate at which the concrete is subjected to, exceeds the rate at which bleeding takes place. This may result in tensile strains due to the rapid removal of its surface moisture. Drying shrinkage and autogenous shrinkage are the main contributions of the overall shrinkage.

2.6.2 Bonded overlays subjected to restrained shrinkage

Restrained shrinkage occurs when concrete is restrained against free movement, including shrinkage or expansion. A retrofitting overlay is prone to shrinkage during its lifespan and will be subjected to tensile stresses due to its bonded, restrained condition. When the tensile capacity of the overlay is breached by these stresses, crack initiation will occur.

De Beer (2016) conducted studies on the behaviour of SHCC bonded overlay when subjected to restrained shrinkage. SHCC was sprayed onto specimens with dimensions of 1030 x 220 mm for the first test setup. The specimens were restrained in the vertical direction when applied to the grooved face of the masonry, while they were restrained horizontally when applied to the smooth face, as shown respectively in Figure 2.11 (a) and (b). The shrinkage of the restrained 30 mm specimen was measured by attaching an LVDT one day after casting. For the second test setup, SHCC (15 mm and 30 mm) was sprayed onto specimens with dimensions 1150 x 935 mm as shown in Figure 2.11 (e). The specimens were cured for 7 days after casting, after which they were wetted until the 14th day, by which the restrained shrinkage was measured. The reader is referred to De Beer (2016) for more details regarding the test setup.

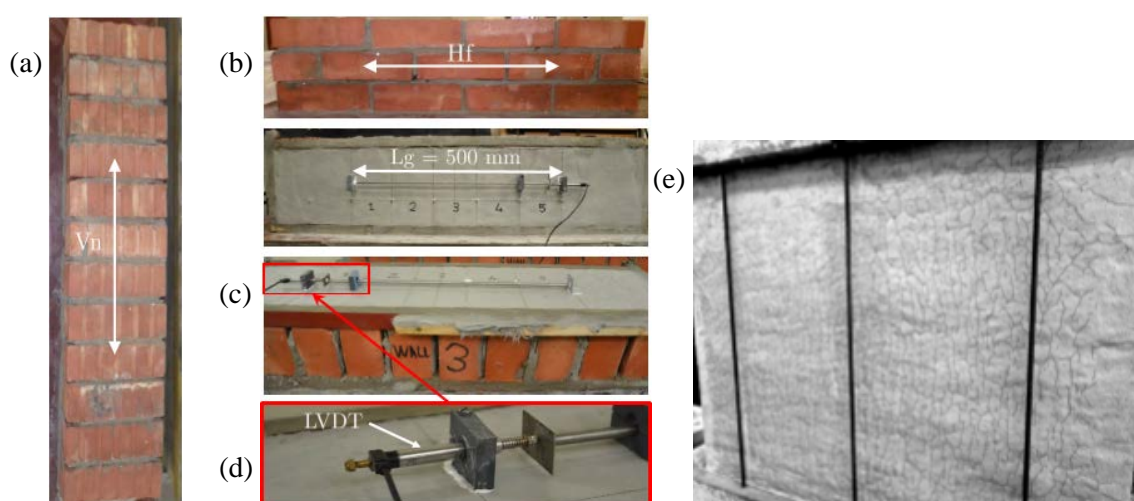


Figure 2.11: Restrainted shrinkage tests where (a) vertically restrained, (b) horizontally restrained, (c) SHCC specimen, (d) LVDT, and (e) 1150 x 935 mm specimen (De Beer, 2016).

The specimens of the first test setup showed an average shrinkage strain of 595 micro strain. For the second test setup, the wall had to be wetted for the cracks to become visible. Crack formation was primarily in the vertical direction, while the cracks reduced towards the vertical edges. For the 15 mm overlay, cracks with a vertical spacing of 44 mm were observed. For the 30 mm overlay cracks with a vertical spacing of 33 mm were observed. For both these overlays, a maximum crack width of 10 μm was observed. No delamination or formation of localised cracks were observed in both test setups. The high tensile capacity and relaxation potential exhibited by SHCC makes it a suitable bonding composite. From the results of the study conducted by De Beer (2016), it can be stated that restrained shrinkage will not pose a detrimental threat to masonry with SHCC overlays.

2.7 Computational Modelling

A finite element analysis (FEA) is performed to obtain a better approximation of the integration issues that the structure may be subjected to. In this type of analysis, a structural element is subdivided into smaller elements, known as finite elements. Thus, an FEA will be appropriate for modelling the strain-hardening response of the nonlinear SHCC material when subjected to seismic loading. The development of computational modelling started in the 1960s when concrete fracture was analysed with the use of smeared cracking and discrete cracking models. A comparison of the models regarding the SHCC fracture response are now discussed.

2.7.1 Discrete crack modelling

Discrete modelling refers to the analysis of a geometrical discontinuity model. This is a result of node splitting by a localised crack due to propagating between nodes, causing increased cracking energy. It is difficult to perform an FEA on the geometrical discontinuity model due to the nodes continuously moving relatively to one another. Difficulties were experienced with the implementation of the complex algorithm solutions needed for the regeneration of the mesh and for elements on the cracking path to be divided, leading to the elimination of discrete modelling (Rots and Blaawendraad, 1989).

2.7.2 Smeared crack modelling

The smeared cracking approach refers to a continuum model in which inelasticity arises once the elastic limit is exceeded and is considered to be spread over the full element. The isotropic stress-strain behaviour this modelling approach is subjected to in the elastic stage, changes to an inelastic orthotropic behaviour, allowing for the elastic response arising orthogonal to the direction of crack formation to be accounted.

In this research, SHCC is sprayed onto masonry shear walls to provide higher ductility and in-plane shear resistance when subjected to seismic loading. This enhanced performance is made possible by the crack bridging ability of the PVA fibres in the SHCC matrix and the composite's ability to undergo significant deformations whilst maintaining its shear and tensile capacity. Boshoff and Van Zijl (2007) developed a continuum damage model, which is related to the basis of a smeared cracking approach when large scale elements are analysed, for masonry walls with SHCC overlay to be computationally modelled. The approach represents the nonlinearity of the SHCC material and is based on the stiffness reduction of the material during the arising of damage.

2.8 Nonlinear Structural Analysis using DIANA

It is essential to have a sufficient understanding of the engineering problem when a finite element analysis is established for solving the problem. The analyst must understand the fundamental background of the procedures available to execute an FEA because the solution methods, material models, and formulations of kinematics need appropriate selection.

The mass and stiffness distribution of a structural element subjected to seismic loading, need to be modelled accurately to ensure that the base movement response is simulated to sufficient accuracy. However, in the case of modelling the masonry with SHCC overlay, push-over forces are applied at its top, satisfying equivalent behaviour as has become a customary simplification in seismic analysis and design. DIANA 10.1 software is used in this research as it contains the necessary nonlinear finite element solution methods needed for the modelling of the masonry with SHCC overlay.

2.8.1 Convergence issues

More challenges are dealt with in the execution of a nonlinear analysis as opposed to a linear elastic analysis. The analyst can typically rely on default procedures when a linear elastic analysis is used for modelling, whereas the selection of an appropriate solution procedure is essential when working with a nonlinear engineering problem. The selection of an inappropriate solution method may result in inaccurate results or unsuccessful execution.

Palacio (2013) identified three types of nonlinear issues which can arise in DIANA relating to convergence, i.e. failing to obtain global equilibrium, local stress-return mapping iterations and errors occurring within the iterative solution procedure. Convergence issues regarding iterative global equilibrium arises when the user specifies an inappropriate solution procedure, which will result in the failure in obtaining global equilibrium.

The following equation specifies how global equilibrium is obtained:

$$[K] \cdot \{v\} = \{w\} + \{Q\} \quad (2.1)$$

Where

| | |
|---------|--------------------------------|
| $[K]$ | is the global stiffness matrix |
| $\{v\}$ | is the displacement vector |
| $\{w\}$ | is the load vector |
| $\{Q\}$ | is the reaction force vector |

Convergence issues regarding the iterative local stress increments will arise when DIANA internally specifies an inappropriate solution scheme, resulting in incorrect stress incrementation at the integration points (Palacio, 2013). This is due to the insufficient mathematical solution of the differential equations when subjected to nonlinear difficulties.

2.8.2 Input data affecting nonlinear analysis

2.8.2.1 Material input

When a variation of stiffness parameters is prescribed to a material, numerical inaccuracies may arise due to significantly different magnitudes on the diagonal of the stiffness matrix. An example of this is when a structural element with a high stiffness is connected to an element with a relatively low stiffness. Convergence issues are also prone to arise when the gradient of the stress-strain curve becomes zero. The stress will remain constant after yielding while the strains will continue to increase, which may cause numerical problems if a force-controlled solution procedure has been selected.

2.8.2.2 Geometry

The local axis of an interface element must be defined to have the correct orientation as this will have an influence on the results of the interface element. If the local axis of the interface element is not in the same direction as that of the continuum element, the results of the elements will have opposite signs which will cause errors.

2.8.2.3 Mesh input

Mesh independency is important for capturing crack paths in a finite element analysis. Thus, the accuracy of the results is dependent on the selected size and/or type of meshing elements used to analyse

crack formation. Computationally, crack formation is prone to follow element edge orientations. A solution may be to select cross-triangle elements, which offer more possible crack orientations computationally. More objectivity problems involve cases where large meshing sizes are selected, because several integration points are required for calculating the stresses and strains in a nonlinear analysis. Thus, the mesh-sensitivity needs to be carefully assessed by analysing at least three different meshing sizes, and comparing the results obtained to find an element size that leads to objective results, that do not significantly change when smaller elements are used. This will enable the analyst to select the appropriate element size for obtaining accurate results.

2.8.3 Analysis procedures

When performing a nonlinear analysis, it is of high importance to select the appropriate incremental load method, iterative solution procedure, and convergence criteria (Palacio, 2013). The correct selection of these three categories is required to ensure that the analysis solution remains on the equilibrium path.

2.8.3.1 Incremental load method

It is fundamental for the correct incremental load procedures to be selected for a valid solution to be obtained. DIANA has three types of incremental methods available for selection i.e. force control, displacement control, as well as arc length. The selection of one of these methods is dependent on the equilibrium path the structure is subjected to.

The force control procedure is a method in which the structural analysis is controlled by applying force increments to the structure. This method, shown in Figure 2.12 (a), is used when the structure is subjected to a continuous increased load without a post-peak softening response. Thus, it is not recommended for this research, as the model will undergo a strain-softening behaviour after crack localisation. Displacement control is when a displacement is incrementally prescribed in a degree of freedom direction at a reference point. This method, shown in Figure 2.12 (b), is applicable for this research as it can evaluate an analysis beyond crack initiation. The arc-length method, Figure 2.12 (c), is recommended when the methods mentioned above are inappropriate. All the equilibrium paths are taken under consideration when this incremental load method is used to perform an analysis.

An automatic incremental load procedure is also an option DIANA offers. This allows DIANA to choose suitable step sizes to avoid convergence issues, as opposed to manual selection by the analyst. This automatic incremental procedure provides the most robust step size that will offer a better chance of obtaining equilibrium, leading to successful convergence.

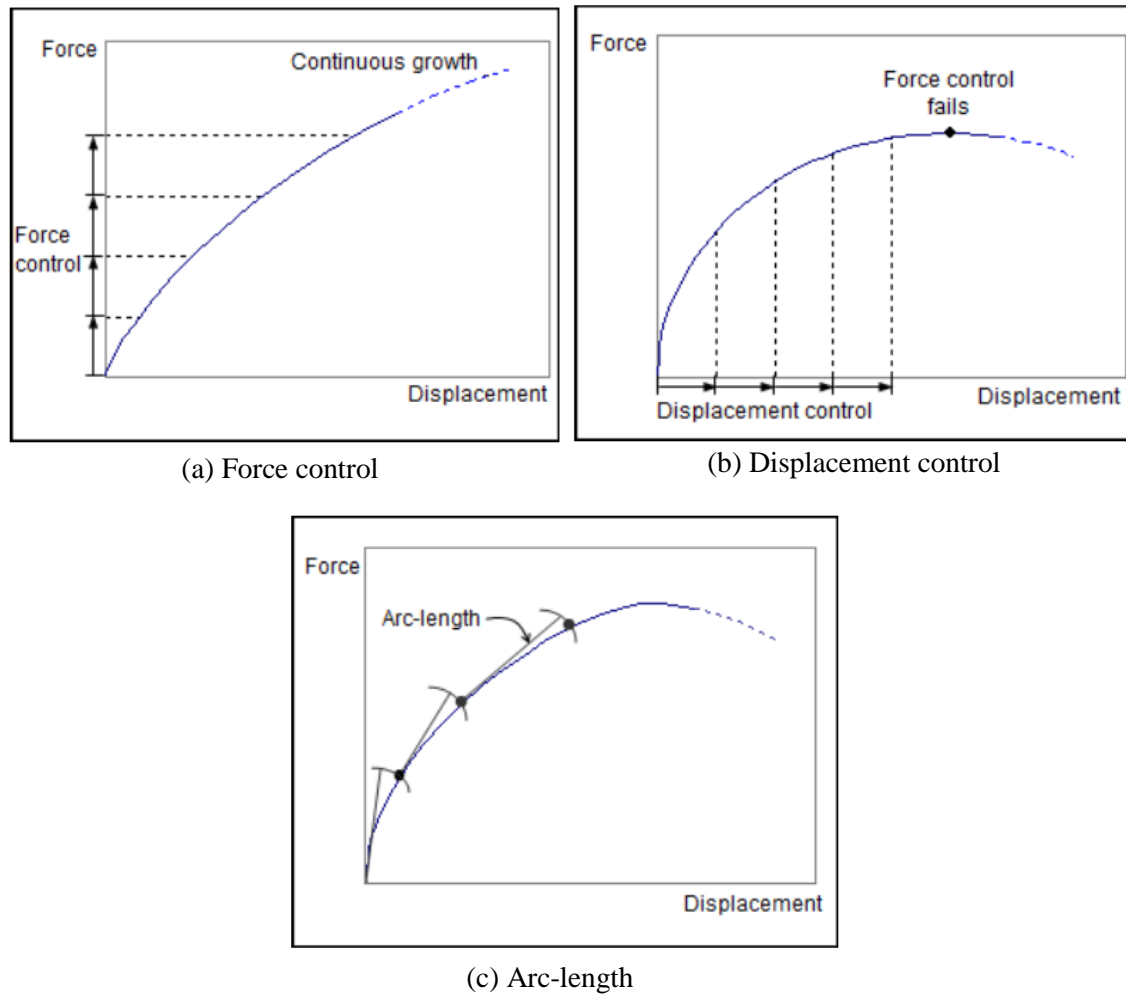


Figure 2.12: Incremental load methods (Palacio, 2013).

2.8.3.2 Iterative solution procedures

After the incremental load method is determined, the global equilibrium equation (Equation 2.1) is satisfied by an appropriate iterative solution procedure. The user has four iterative solution method options when working with DIANA i.e. regular Newton-Raphson, modified Newton-Raphson, Secant, and the constant iterative stiffness method. Figure 2.13 shows a graphical idealisation of these four methods.

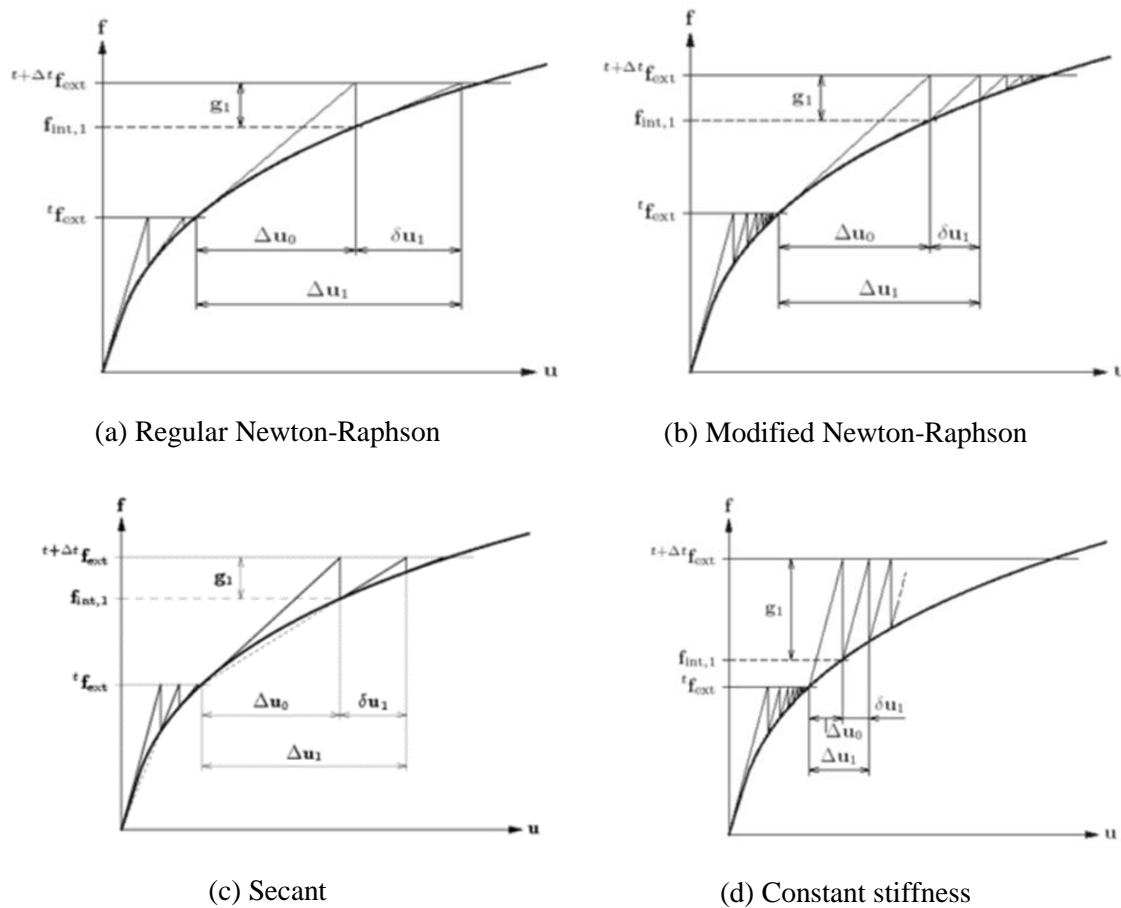


Figure 2.13: Iterative solution procedures (Palacio, 2013).

2.8.3.3 Convergence criteria

The convergence criteria are a measurement of the accuracy of the solution, compared to the exact solution, after each incremental force (displacement or load) step. It is important for the user to specify a suitable tolerance, as a large tolerance will cause offset from the equilibrium path, resulting in inaccurate results and eventual divergence, while a small tolerance can result in a time-consuming analysis. DIANA offers different norms by which the convergence criteria can be controlled, including a displacement, force, and energy norm. An option is also available for any pair, or all three these norms to simultaneously be used as a combination. The behaviour of the structure under consideration should be fully understood by the analyst to ensure that a suitable convergence tolerance and norm are selected.

The energy norm is suitable for this research and combines displacement and force changes from the previous iteration into a normalised energy deviation from the previous iteration with requirement that it reduces to below the selected tolerance. For this larger scale structure, a relatively large tolerance is opted for to balance computational effort with acceptable accuracy. However, the user should check if a correct equilibrium path is followed regarding the tolerance, as a lenient tolerance is prone to divergence.

2.9 Bonded SHCC Overlay Systems

The strain-hardening behaviour exhibited by the SHCC material enables cracks to be bridged, leading to higher ductility. In addition to this, the interface behaviour significantly influences the failure behaviour. Thus, it is needed to consider the mechanical response of the interface between the SHCC overlay and the substrate it is bonded to, as this will influence the crack widths and spacings that will form within the SHCC overlay. The overlay durability will consequently be affected by the interface properties.

It is possible to attain a well-balanced relationship between crack formation within the SHCC overlay and the delamination thereof by means of varying the bond strength and roughness of the interface surface. This will ensure both the crack widths within the overlay to be significantly small and the structure to undergo a monolithic mechanical response. The decrease in crack widths also enables an increased potential of the cracks to heal by themselves and reduce the permeability (Van Zijl et al., 2012).

The following sections discuss why a weaker bond will be more beneficial when the shear wall is subjected to a mechanical load, whereas a stronger bond will be more beneficial in the case when drying shrinkage is considered.

2.9.1 Bonded SHCC overlay subjected to mechanical loading

Luković et al. (2014) conducted mesoscale tests to investigate the fracture response when an SHCC overlay with different substrate surface profiles is subjected to a mechanical load. Numerical analysis of beams subjected to three-point bending were performed in 3D. Three concrete beam specimens, with dimensions of 12 x 16 x 62 mm, had different surface profiles on its one face. The uncracked beams had a 5 mm SHCC overlay applied to its tension surface. An overlay material without any fibres was also applied to all of the beams as a reference case, for comparison with the SHCC material.

Figure 2.14 displays the crack patterns of the beams with three different surface profiles and SHCC overlay on the left, with the models containing overlays with no fibres displayed on the right. A longer debonded area in which distributed cracks are present occurs in the case of the smooth surface. The additional cracks present in the smooth surface will be beneficial for the durability of the structure since the cracks will be finer compared to those formed in a more localised area as in the case of the rough surface. It can also be seen that in the case of a rough surface the cracks propagate more localised into the concrete substrate than in the case of the smooth profile, making localised cracking failure more vulnerable.

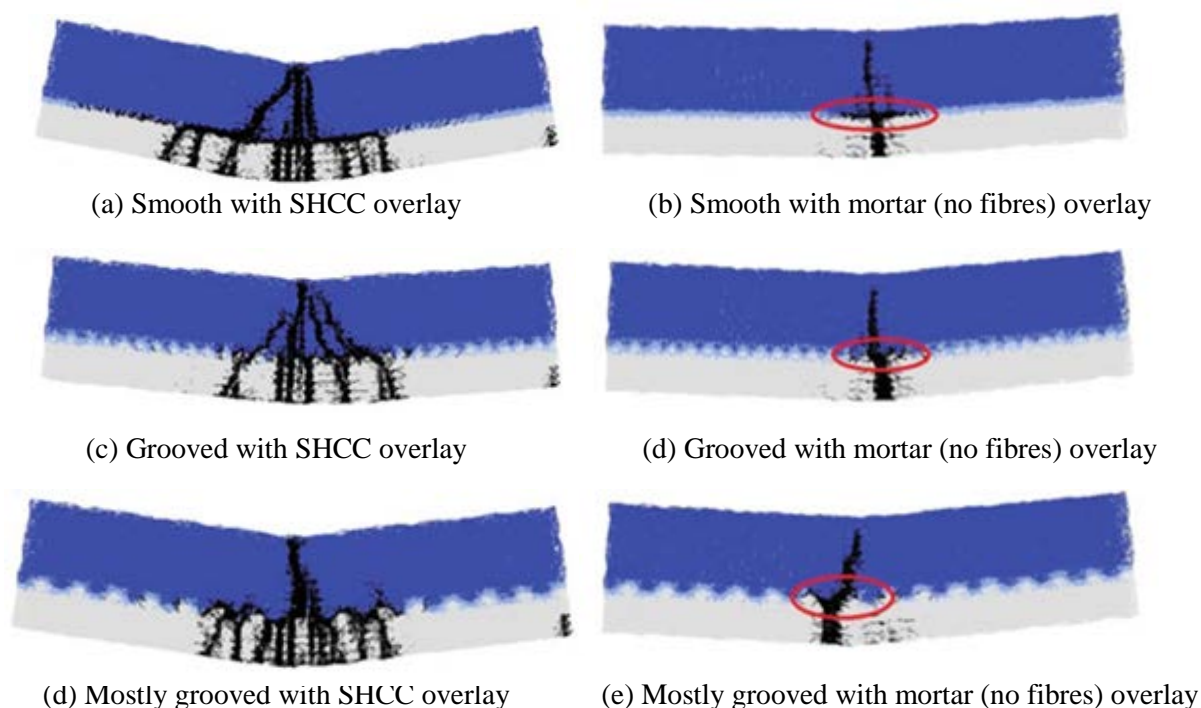


Figure 2.14: Simulations of the beams subjected to three-point bending showing the crack patterns with the SHCC at the bottom (Luković et al., 2014).

Luković et al. (2014b) performed similar simulations on pre-cracked beams with dimensions 42 x 42 x 150 mm, by which a 15 mm SHCC overlay is applied to the compression face. The simulations were performed as a comparison with the results of the above simulations. Smooth and grooved profiles are compared and both an SHCC material and overlay material without fibres are used for investigation. From Figure 2.15, it can be seen that the smooth profile (right) shows a similar response to the results mentioned above, relative to the results of the grooved profile (left). From these results it can be stated that a smooth surface will be more beneficial when the structure is subjected to a mechanical load. However, one must keep in mind that there is a minimum value the bond strength can be below which the global failure behaviour will be due to complete delamination of the SHCC overlay.

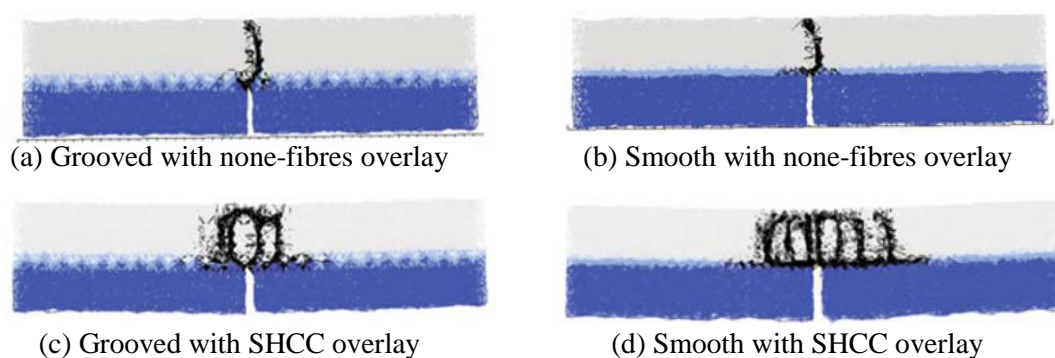


Figure 2.15: simulations showing the crack patterns where the overlay is applied at the top compression face of the three-point bending test (Luković et al., 2014).

2.9.2 Bonded SHCC overlay subjected to drying shrinkage conditions

The tests discussed in the previous section indicate that a smooth profile is more beneficial under a mechanical load. However, the effects of drying shrinkage were not taken into consideration during the simulations. The interface properties need to be carefully considered in cases where the drying shrinkage of the SHCC overlay varies with that of the concrete substrate. Drying shrinkage may result in uncontrolled delamination of the overlay in cases where the surface is too smooth with a low bonding strength, causing failure before any strain-hardening response is utilized. Therefore, it is important to ensure a sufficient surface roughness to reduce the risk of the damage potential the drying shrinkage holds.

SHCC is prone to higher strains caused by drying shrinkage due to its smaller size and lower content of aggregate and the high cement/binder content. However, Luković et al. (2014) performed simulations showing that SHCC material has smaller drying shrinkage crack widths than that of normal mortar overlays when subjected to the same surface profile and environmental conditions. More cracks will form in the SHCC overlay with a reduced crack spacing due to its strain-hardening behaviour. Figure 2.16 shows the simulations performed by Luković et al. (2014), from which it is clear that a higher surface roughness with a higher bond strength, or a lower overlay thickness, will result in a more beneficial crack distribution.

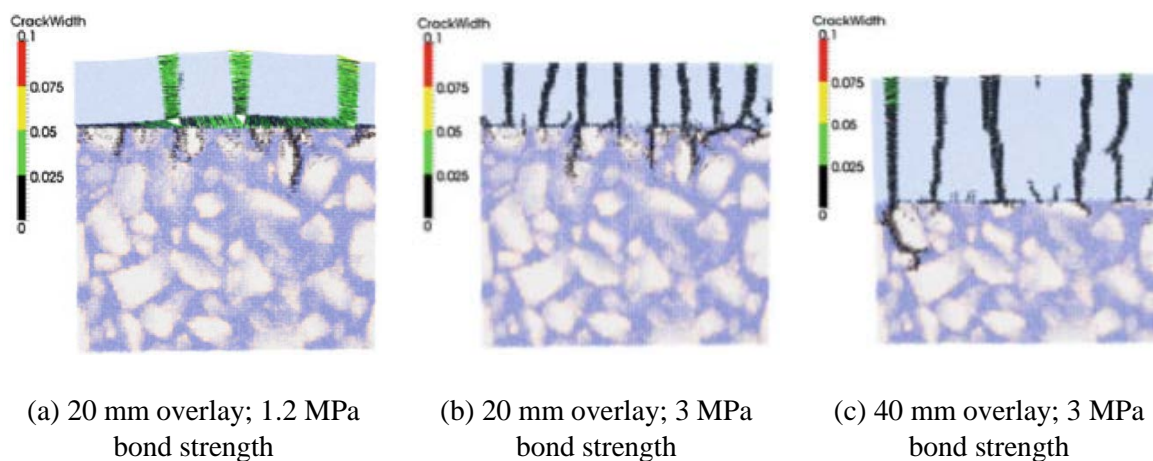


Figure 2.16: Crack distributions of simulations obtained by drying the top surface of the SHCC material (Luković et al., 2014).

From the simulations discussed above it is clear that a smooth profile with a relatively low bonding strength will be more beneficial conditions when the structure is subjected to mechanical loading, however, under drying shrinkage circumstances, a rough profile with a relatively high bonding strength will be more beneficial.

2.9.3 Balanced interface behaviour

A balanced relationship between the surface roughness, favourable for mechanical loading and drying shrinkage, may lead to optimal performance of the SHCC overlay. The goal is to obtain a surface profile rough enough to avoid delamination, but also as smooth as possible for beneficial crack distribution, increasing the ductility performance of the structure.

Van Zijl and Stander (2009) performed experimental flexural tests and simulations of a concrete substrate retrofitted with an SHCC overlay, with an artificial crack in the beam and a 50 mm debonded strip. The simulations and experimental tests showed similar global flexural results. The strain diagrams of the simulations, seen in Figure 2.17 (c) and (d), showed that an increased strain distribution is obtained when applying a debonded strip. This indicates the possibility of obtaining a higher crack distribution area without delamination when SHCC overlay and debonded strip interfaces are applied to masonry shear walls. A similar balanced interface relationship approach will be used in the testing of the shear walls with SHCC overlay subjected to a pull-over force for the scope of this study.

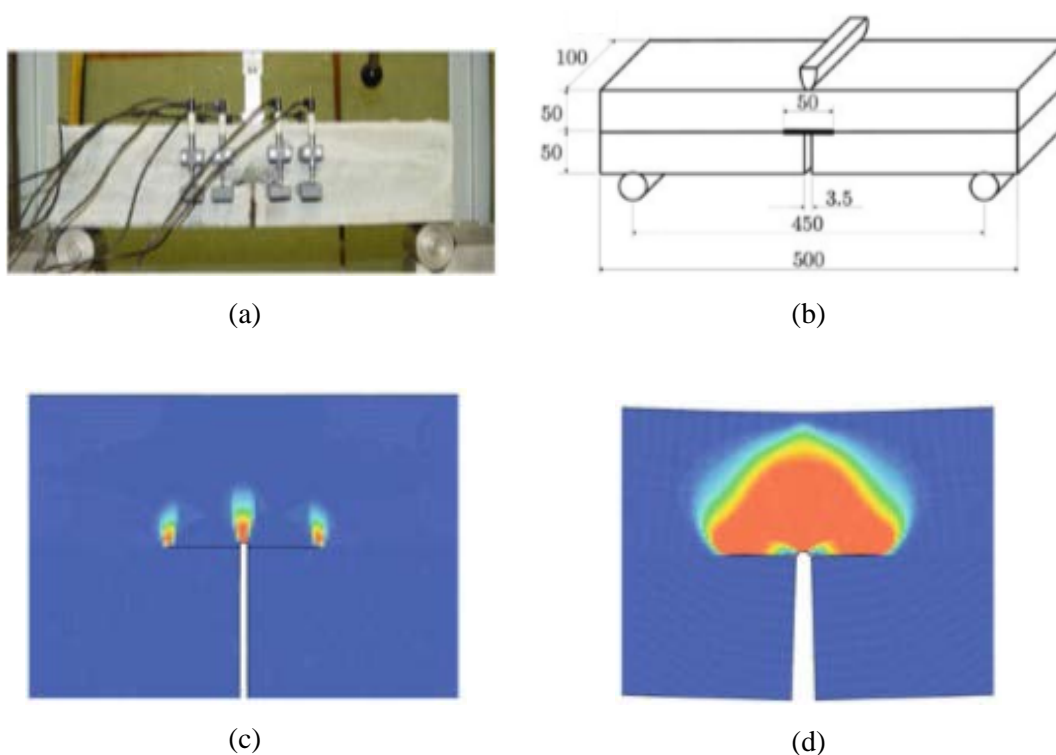


Figure 2.17: (a) and (b) flexural experiments with SHCC on a concrete substrate, followed by the simulations with (c) 55% of maximum load and (d) maximum load (Van Zijl and Stander, 2009).

2.10 Earthquake Displacement Demand

Le Roux and Wium (2012) demonstrated the determination of earthquake displacement demand, which a structure's shearing deformation capacity should exceed for its structural safety in the event of an earthquake in the particular seismic region and founding soil. The earthquake demand is beyond the scope of research performed here. Consider the ductility factor (μ) expressed by

$$\mu = \frac{\delta u}{\delta y} \quad (2.2)$$

where δu is defined as the in-plane shearing deformation when the post-peak shearing resistance has reduced to 80% of the peak, and δy is the 'yield' shearing deformation defined by Mahmood and Ingham (2014) as the shearing deformation at the intersection of an elastic-plastic bilinear approximation of the load-deformational response. Previously, Prota et al. (2006) proposed the displacement at peak as the denominator in eq. (2.2), instead of the yield displacement, but this leads to poor representation of the ductility in cases of highly nonlinear response. The ductility factor for the walls tested by De Beer (2016) was on average 1.8 (CoV 0.187). This is low compared with ductility factor of 5.2 reported by Lin et al. (2014), but their CoV=0.52 raises concern about the reliability with which the deformation demand of an earthquake can be met by the deformation capacity of their retrofitted walls.

In order to improve the SHCC retrofitted shear wall ductility, the concept of debonded regions in the SHCC/masonry interface is investigated here, to prevent reflective cracking of a crack in the substrate through the overlay, whereby multiple cracking characteristic of SHCC as overlay is suppressed (Van Zijl and Stander, 2009). In presence of a debonded region, kinked-crack trapping is enabled in an SHCC overlay (Lim and Li, 1997), whereby reflective cracking is prevented and multiple cracks form in the SHCC overlay instead. Note, the ductility factor is not determined for the experimental walls tested in this research as it does not account for the shear strength. A new factor showing the energy increase from the walls with debonded strips to the reference wall without debonded strips is introduced.

Chapter 3

Nonlinear Computational Modelling of Shear Walls

This chapter documents the computational models developed to describe the behaviour of masonry shear walls, bare and retrofitted with an SHCC overlay, when subjected to a pull-over load. Figure 3.1 is a representation of the practical setup previously used at SUN to perform experimental tests on the shear walls. The tests contained specimens with different masonry and overlay thickness. DIANA FEA software is used for the execution of the structural nonlinear FEM analyses. Analyses are performed to obtain results on bare masonry of single, double and triple leaf thickness (110 mm, 220 mm and 330 mm thickness respectively). A model with 220 mm thick masonry retrofitted with a 15 mm SHCC overlay is analysed and calibrated to the experimental tests. Thereafter, different thickness masonry and overlays are analysed and discussed. Computational modelling discussed in this chapter is divided into three sections:

1. DIANA FEA shear wall model setup.
2. Results and discussions of shear wall computational models.
3. Conclusions and recommendations.

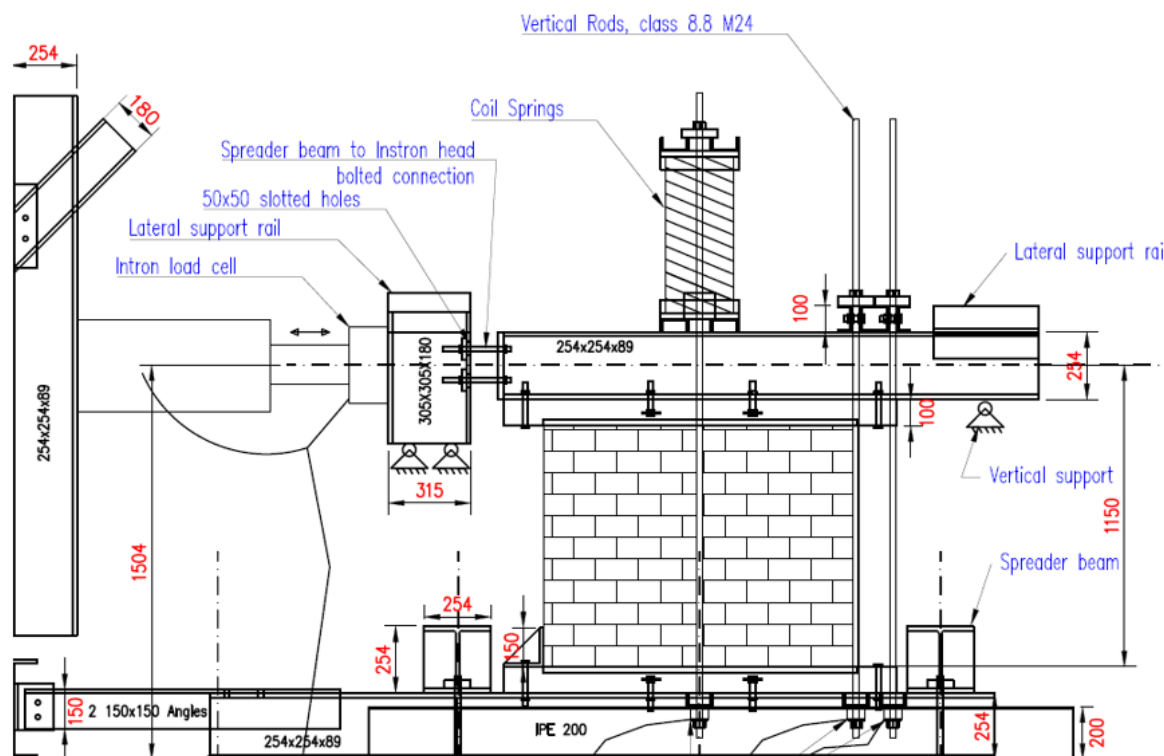


Figure 3.1: Experimental masonry shear wall setup (De Beer, 2016).

3.1 DIANA FEA Shear wall model setup

3.1.1 Geometry

The shear wall setup, shown in Figure 3.2, consists of five structural elements i.e. masonry, SHCC, steel rods, concrete beam, and a steel beam. The geometry of the elements, excluding the rods, is defined as sheets with an element class of 3D membranes assigned to it. The three steel rods are defined as 3D line elements. A structural masonry-SHCC interface is also included in the model. Although only in-plane membrane action is considered, provision for layers of masonry, an overlay and the interface between them, necessitates a 3D approach.

The SHCC and masonry have similar plane dimensions with varying thicknesses as shown in Figure 3.2. The reinforced concrete (RC) beam with dimensions shown, varies in thickness depending on the thickness of the masonry wall. A 400 mm thick RC beam is used with the use of a 220 mm and a 330 mm thick masonry wall, whereas a 280 mm thick concrete beam is used with a 110 mm single leaf masonry wall. An H-profile load spreader steel beam, with dimensions shown in Figure 3.2, is placed on top of the concrete beam with the prescribed pull-over load applied to its centre.

Three rods are connected to the top of the H-beam and pre-tensioned as shown in Figure 3.1 and indicated by arrows on the spreader beam in Figure 3.2, in order to prevent the shear wall from tipping over due to the horizontal pull-over force. Further discussions of the loading conditions that the structure is subjected to are presented in Section 3.1.4.

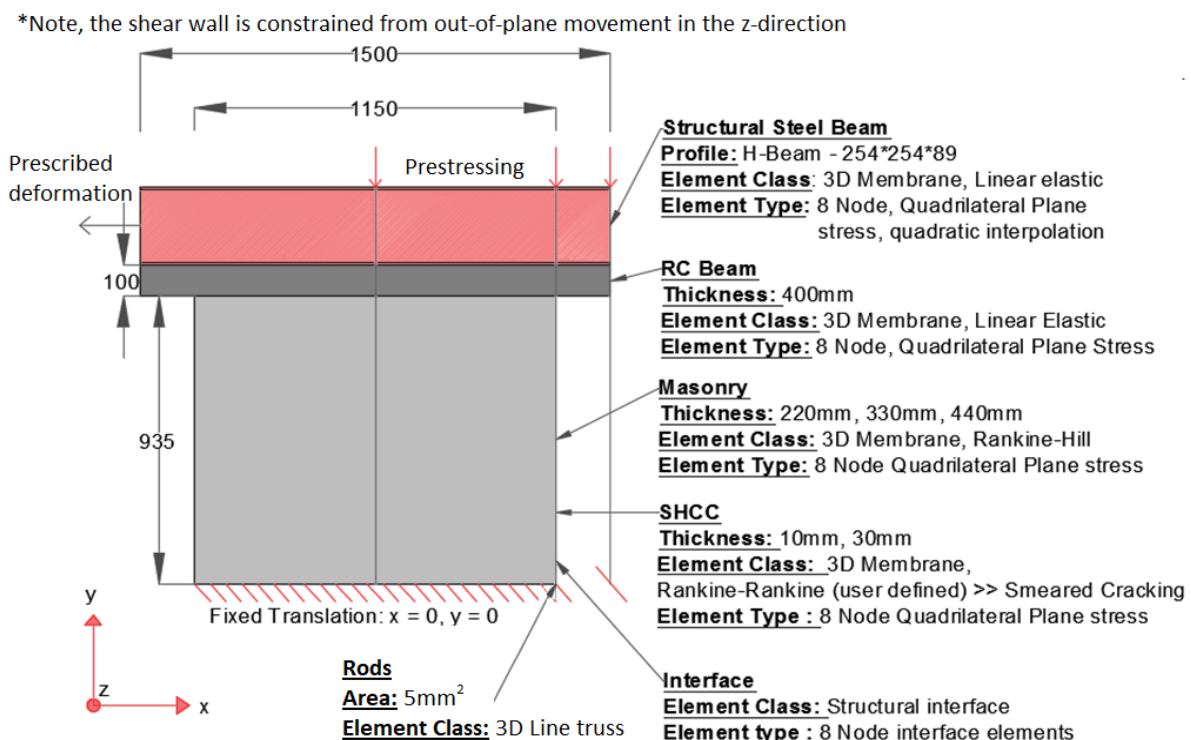


Figure 3.2: Geometrical setup of computational shear wall model.

3.1.2 Material Properties

Various tests were performed by De Beer (2016) at SUN, for the determination of the material properties used in the computational models presented in this section. A standard sprayable mix and clay brick wall parts were used for the determination of the SHCC and masonry characteristics respectively. The material models and parameters for each structural element used in the computational models are discussed in the following subsections.

3.1.2.1 Masonry

The masonry wall is schematised as a nonlinear continuum model. This is done to avoid detailed account of the masonry units and mortar joints. Damage in the form of crushing, cracking and shear-slip is accounted for in a smeared way within the continuum model. A plane stress Rankine-Hill plasticity model is used, which accounts for elastic and inelastic orthotropy exhibited by the masonry shear walls. The model incorporates strain-softening response in tension, and strain-hardening followed by strain-softening in compression. The model is formulated in a framework of multi-surface plasticity, combining an anisotropic Rankine yield limit function for tension with an anisotropic Hill limit surface for compression. The yield conditions of a Rankine-Hill continuum model are displayed in Figure 3.3. The parameters used as input for the masonry material are summarised in Table 3.1. Full details of the Rankine-Hill model are given by Lourenco (1996) and Van Zijl (2000).

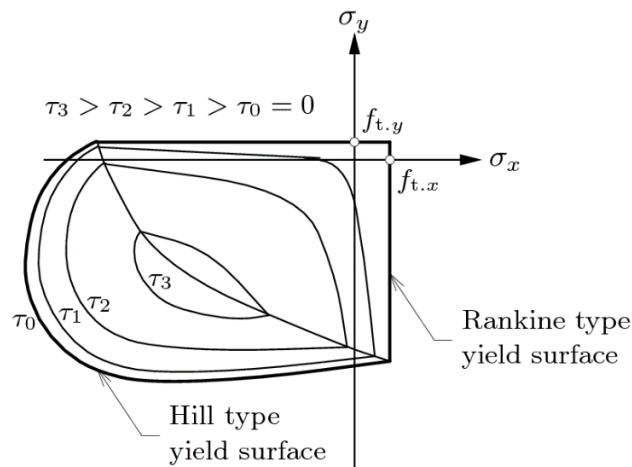


Figure 3.3: Yield conditions of a Rankine-Hill material model.

Table 3.1: Masonry Rankine-Hill material properties input.

| Symbol | Unit | Definition |
|--------------|--|--|
| E | 1800 N/mm ² | Young's Modulus |
| ν | 0.22 | Poisson's ratio |
| P | 2.1×10^{-9} T/mm ³ | Mass Density |
| f_{t_x} | 0.35 N/mm ² | Tensile Strength (x) |
| f_{t_y} | 0.22 N/mm ² | Tensile Strength (y) |
| $f_{c_{ux}}$ | 20 N/mm ² | Compressive Strength (x) |
| $f_{c_{uy}}$ | 20 N/mm ² | Compressive Strength (y) |
| Gf_x | 0.15 N/mm | Fracture Energy in Tension (x) |
| Gf_y | 0.1 N/mm | Fracture Energy in Tension (y) |
| Gc_x | 2 N/mm | Fracture energy in compression (x) |
| Gc_y | 2 N/mm | Fracture energy in compression (y) |
| ϵ_u | 0.001 | Ultimate compressive strain i.e. strain at ultimate compressive stress |

3.1.2.2 SHCC

SHCC provides significant ductility to a structural element due to its strain-hardening behaviour in tension, as previously described in Section 2.4. Research on this retrofitting material has started in the early 1990's, and the concrete material has improved ever since. De Beer (2016) developed an SHCC mix for optimized spray-ability, shown in Table 2.3, which is adopted for the computational modelling of this research.

A smeared rotational cracking model is used for the material model of the SHCC overlay, and elastic perfectly-plastic behaviour is simulated by a high fracture energy. This material model is chosen to reasonably simulate the experimental results documented by De Beer (2016). The simple straight line softening curve (Figure 3.4) is selected with the tensile properties shown in Table 3.2. Linear elastic behaviour is chosen for capturing the compressive behaviour, because compressive inelasticity is not expected in the overlay.

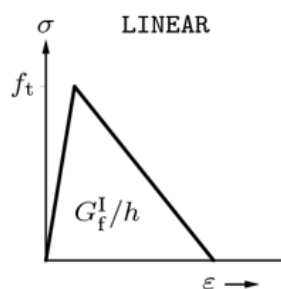


Figure 3.4: Linear-crack fracture energy curve

The material parameters input of the smeared rotational cracking material model is shown in Table 3.2. The tensile parameters were determined from the DTT performed by De Beer (2016) as discussed in Section 2.5.3. Note, the tensile strength until first cracking (f_c) is used as the tensile strength input instead of the tensile strength until ultimate failure (f_{tu}). As previously mentioned, a high fracture energy of 10 N/mm is used to obtain an elastic-perfect plastic response in tension, which is similar to the post cracking behaviour as those of the results of De Beer (2016), excluding the stress-strain wiggles.

Table 3.2: Smeared rotating crack material model input.

| Symbol | Unit | Definition |
|----------|--|-------------------------------|
| E | 15000 N/mm ² | Young's modulus |
| ν | 0.2 | Poisson's ratio |
| ρ | 2.1×10^{-9} T/mm ³ | Mass density |
| f_t | 2.00 N/mm ² | Tensile Strength |
| G_{ft} | 10 N/mm | Modified fracture energy |
| - | - | No damage reduction curve |
| - | - | Elastic compressive behaviour |

3.1.2.3 Masonry-SHCC Interface

The structural interface, describing the bond between the masonry wall and the SHCC overlay, is modelled as a 3D plane interface with Coulomb-friction behaviour. De Beer (2016) performed triplet tests on single leaf masonry walls to determine the average adhesive bond strength (c_j) and the coefficient of friction (ϕ). The bond strength and friction coefficient were determined as 2.25 MPa and 1.07 respectively. The structural interface is also assigned a small dilatancy angle of 0.1 radians. For full details of the Coulomb-friction interface model, the reader is referred to Van Zijl (2000).

3.1.2.4 Concrete beam

The RC beam represents the upper story floor slab of the masonry building. Floor slabs act as diaphragms to transfer lateral forces caused by wind or earthquakes to the masonry shear walls. Linear elastic material parameters are prescribed to the RC beam to limit the level of complexity. De Beer (2016) specified a compressive strength for the concrete beams used in the shear wall experiments. The following material parameters are selected: The Young's modulus is 28 GPa, with an 0.15 Poisson's ratio and 2350 kg/m³ mass density.

3.1.2.5 Steel beam

An Instron MTM with a 500 kN hydraulic actuator was used in the experimental shear wall tests. The Instron head was connected to the steel beam at which the prescribed deformation load was applied. In the finite element model, the H-section steel beam with dimensions 254 mm x 254 mm x 89 kg/m is modelled in plane stress and assigned linear elastic material properties of a 200 GPa Young's modulus, 0.3 Poisson's ratio and a mass density of 7850 kg/m³.

3.1.3 Boundary Conditions

The boundary conditions applied to the shear wall models represent the movement restrictions a shear wall is subjected to in an URM building. A ground floor shear wall is generally fixed at its foundation, preventing translation in any direction. The upper story floor slabs in a multi-story masonry building convey vertical floor loads of the upper story to the shear wall, and transfer lateral loads to the wall through diaphragm action. Through their flexural stiffness, the floor slabs also restrict vertical displacement of the shear walls. Thus, the shear walls in the computational models are restricted by the following constraints:

- Foundation fixed against in-plane horizontal and vertical translation, $u_x = u_y = 0$.
- Lateral out of plane translation constraint for all structural elements, $u_z = 0$.
- Prescribed deformation at a node on the upper beam for horizontal constraint in the displacement-controlled pull-over, $u_x = -20$ mm. (Note that in execution of the nonlinear analysis, this is applied incrementally, and the final total displacement may be lower than, or exceed this value.)
- Steel rods are pre-stressed to limit vertical movement as well as rotating motion. However, these constraints are not modelled as boundary conditions, but rather as an initial pre-stressing force applied to the rods.

3.1.4 Loadings

The masonry shear wall is subjected to self-weight as well as external loads. Horizontal and vertical categories are used to set up the phases in which the loading regimes are performed during the analysis as discussed in Section 3.1.6. Load combinations 1, 2 and 3 represent the two vertical loads of self-weight and pre-stressing of the steel rods, and the one horizontal load respectively.

The vertical loads of combination 1 are a representation of the constant pressure created by the mass of the slabs and the rest of the building above the shear wall. Three vertical steel rods are pre-stressed for the pressure to be modelled, instead of applying a pressure to the top. This is preferred, because

subsequent to the pre-stressing, the rod forces change according to the shear wall deformation, in a simplified simulation of the upper floor flexural stiffness and restraint. An initial tensile force of 28 kN is applied to the rod at midsection, while an 18 kN force is applied to the rods on the right-hand flank.

Combination 2 represents the own weight of all the structural elements. The own weight is calculated by $-9.81 \text{ m/s}^2 \times \text{volume} \times \text{mass density (kg/m}^3\text{)}$.

A horizontal displacement of -20 mm is prescribed as combination 3. The load is applied on the left-hand side at mid-height of the steel beam and represents the horizontal pull-over load applied by the Instron head. The load combinations prescribed in the computational simulations are shown in Table 3.3.

Table 3.3: Load combinations.

| | Pre-tensioned Rods | Own Weight | Prescribed Deformation |
|---------------|--------------------|------------|------------------------|
| Combination 1 | 1 | | |
| Combination 2 | | 1 | |
| Combination 3 | | | 1 |

3.1.5 Mesh

3.1.5.1 Finite elements

Isoparametric 3D plane stress finite elements are used by Diana FEA when working with 3D plane stress membranes. Triangular elements are used for the scope of this study as they provide a better alignment of crack formation on the diagonal. The integration of equations in these six-node finite elements, described by a CT18GM notation in DIANA, is solved by Gauss numerical integration and interpolating quadratically over the surface area as shown in Figure 3.5 (a). The nodes have an enumeration spanning positively in the x-direction. The x-direction strains (ϵ_{xx}) and forces in the membranes (η_{xx}) have a linear variation in the x-direction, and in the y-direction it varies quadratically, while the y-directional strains (ϵ_{yy}) and membrane forces (η_{yy}) have vice versa variations.

3.1.5.2 Interface elements

DIANA FEA describes the 3D plane structural interface elements with a CT36I notation. The nodes of the six-node finite element planes mentioned are shared by the interfacial element as shown in Figure 3.5 (b). Thus, the selected interface element is a triangular twelve-node element.

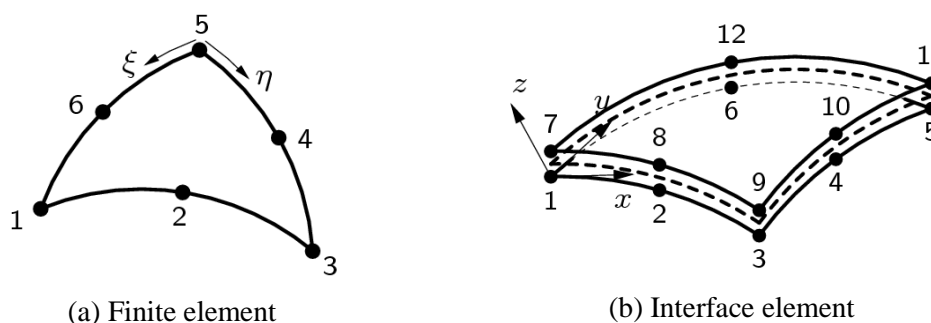


Figure 3.5: Triangular finite membrane and interface elements.

3.1.5.3 Mesh dependency

A mesh dependency test is performed on the 220 mm masonry wall with a 15 mm SHCC overlay (SW220-15). The test started with a 15 mm element size and ended with a 105 mm element size with 15 mm increments. From Figure 3.6, it appears that mesh independence is obtained for element sizes of 30 mm and smaller. For the computational models discussed in this research, an element size of 30 mm is selected, considering that a 15 mm element size requires more than double the analysis time. Note that the steel rods are modelled as one element each, only connected at their lower end to the coinciding wall foundation node, and at their upper end to the coinciding steel beam node. The 30 mm triangular mesh of the SW220-15 is displayed in Figure 3.7.

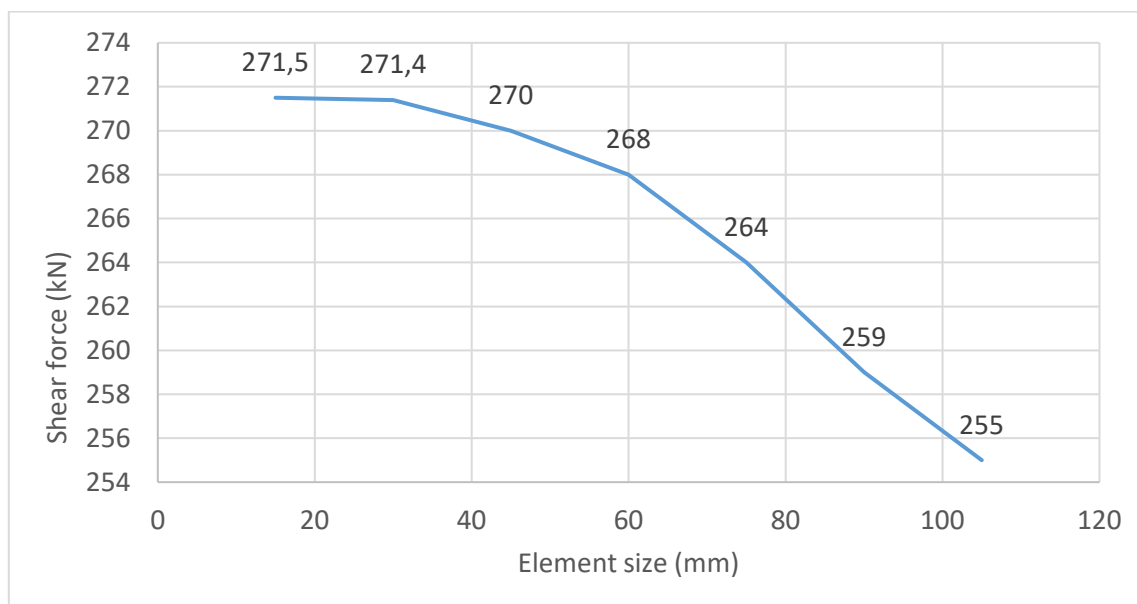


Figure 3.6: Mesh dependence test performed on 220 mm masonry wall with 15 mm SHCC overlay (SW220-15).

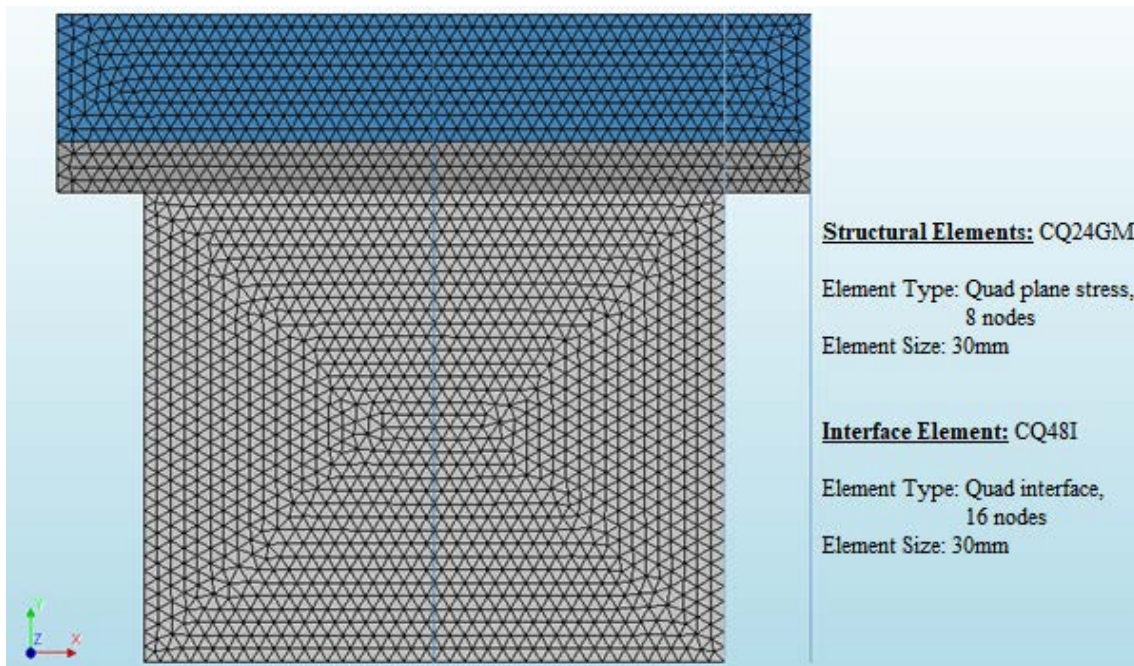


Figure 3.7: Triangular 30 mm mesh of elements.

3.1.6 Analysis

A phased analysis is performed to analyse the performance of the shear wall retrofitted with SHCC overlay. This type of analysis allows for the execution of different calculations in different phases, by which the calculations of one phase switch over to that of a different phase after each phase break. There are options to change the loads, constraints, and structural elements from one phase to the next (Manie and Kikstra, 2017).

The vertical forces, as described in Section 3.1.4, are prescribed as phase one and the horizontal forces as phase two, Figure 3.8 (a). Phase one and two are prescribed as “Phased” and “Phased 1” respectively.

The vertical stresses calculated during phase one are the initial stresses at the start of phase two. This is activated by using the loads in the previous phase in the execution of the start steps of the second phase. The stress initialization of the second phase is shown in Figure 3.8 (b). Note that the selection of the initial stress box is during phase one, representing the stresses at the start of the analysis.

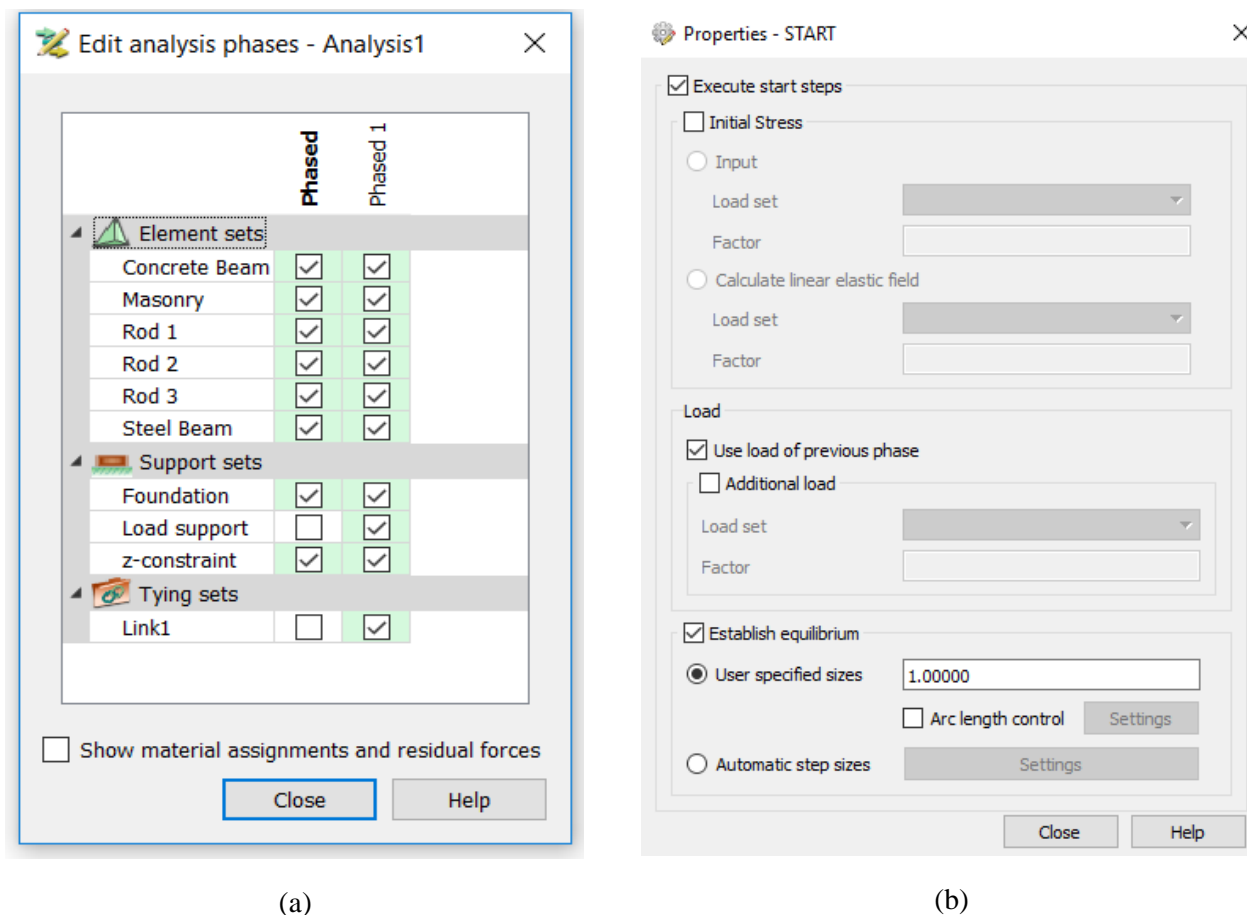


Figure 3.8: Procedures with (a) Phase analysis; (b) Stress initialization.

3.1.6.1 First Phase – Vertical Forces

Two nonlinear analyses are executed during the first phase of which the first is the constant pressure created by the vertical rods (Combination 1, Table 3.1). The application of the self-weight (Combination 2) follows thereafter. After application of load combination one, the pressure remains constant during the execution of the self-weight. This analysis phase is relatively simple, as only two steps are executed, with no incremental load steps.

The Secant (Quasi-Newton) method described in Section 2.8.3, Figure 2.11 (c) is used as the iterative solution procedure. An energy convergence norm with a tolerance of 0.0001 is used to obtain full convergence, but also a trustworthy solution path. The parallel direct sparse method is selected in both the nonlinear analysis. After execution of the first phase, the results are used as the initial step of the second phase.

3.1.6.2 Second Phase – Horizontal Forces

The incremental prescribed horizontal displacement is applied in phase two, while the vertical forces of combination 1 and 2 are retained from the initial step. All the constraints and structural elements are active during this phase as seen in Figure 3.8 (a). The main objective of this phase is to calculate the shear force reaction due to shear deformation occurring in-plane.

This phase consists of two blocks of execution, of which the first block comprises of the initial stresses created during phase one. The prescribed deformation of combination 3, is applied incrementally by nonlinear load iterations during execution of block two. The Secant method is again selected as the iterative solution procedure.

Line search is also selected to optimise convergence due to high level of nonlinearities exhibited by the masonry wall with SHCC overlay. The line search function is an algorithm in which the potential energy in each increment is reduced by scaling the displacement increment. The convergence procedure is shown in Figure 3.9 with the symbols of the incremental procedure discussed in Figure 3.10 (b).

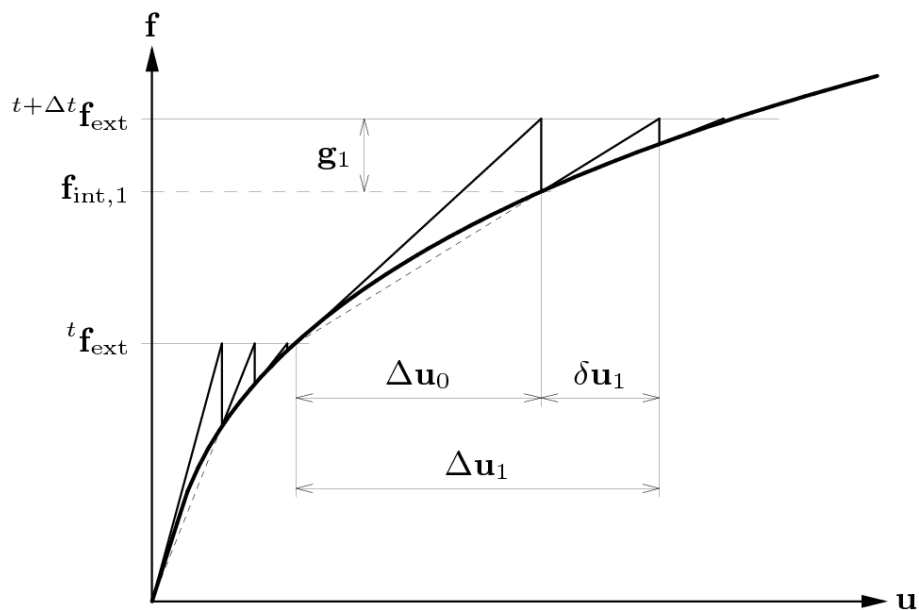
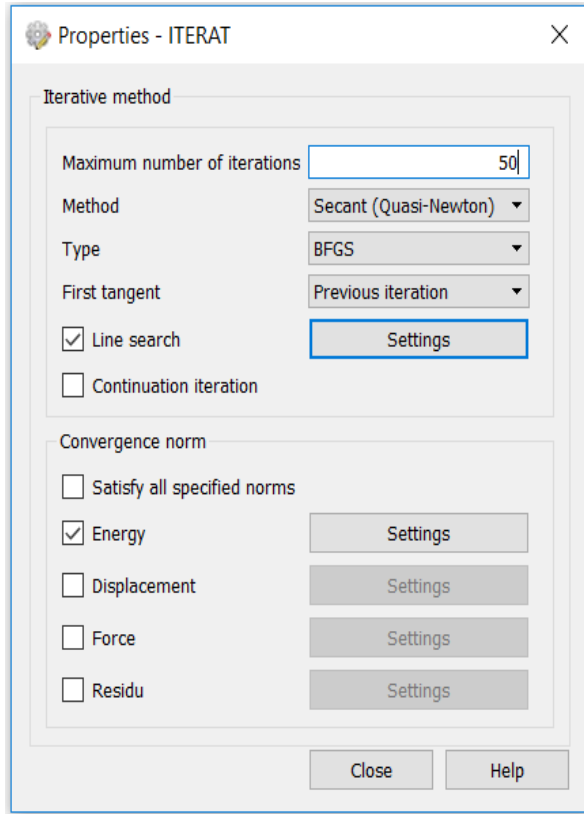
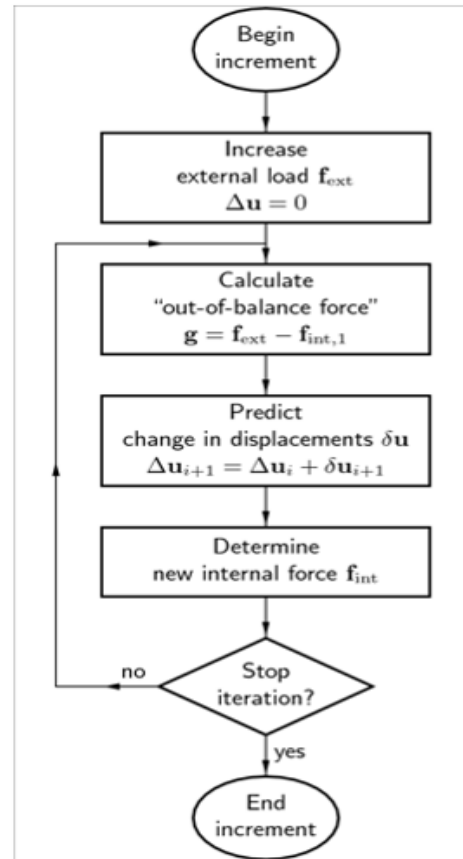


Figure 3.9: Convergence procedure (Manie and Kikstra, 2017).

The properties of the iterative method are shown in Figure 3.10 (a), with Figure 3.10 (b) indicating how the Secant solution procedure works in general.



(a)



(b)

Figure 3.10: (a) Properties of iteration method, (b) Solution procedure.

3.2 Results and Discussions of Shear Wall Computational Models

This section presents the results of the analyses performed with the computational model setup discussed in Section 3.1. The behaviour of the masonry shear walls (SW) under seismic loading regimes without SHCC overlay is tested first. However, the aim is to investigate the increased performance of shear walls retrofitted with an SHCC overlay.

The computed results are compared with the experimental tests previously performed at SUN. The shear force vs horizontal displacement response of the shear walls when subjected to prescribed displacement loading regimes are plotted and illustrated diagrammatically.

A total of twelve nonlinear analyses are executed and discussed in this section. Table 3.4 lists the notations with their description of the executed computational models.

Table 3.4: Notations of computational models.

| Notation | Description |
|----------|---|
| SW110-0 | Shear wall specimen wall thickness 110 mm, no overlay |
| SW110-10 | Shear wall specimen wall thickness 110 mm with 10 mm SHCC overlay |
| SW110-15 | Shear wall specimen wall thickness 110 mm with 15 mm SHCC overlay |
| SW110-30 | Shear wall specimen wall thickness 110 mm with 30 mm SHCC overlay |
| SW220-0 | Shear wall specimen wall thickness 220 mm, no overlay |
| SW220-10 | Shear wall specimen wall thickness 220 mm with 10 mm SHCC overlay |
| SW220-15 | Shear wall specimen wall thickness 220 mm with 15 mm SHCC overlay |
| SW220-30 | Shear wall specimen wall thickness 220 mm with 30 mm SHCC overlay |
| SW330-0 | Shear wall specimen wall thickness 330 mm, no overlay |
| SW330-10 | Shear wall specimen wall thickness 330 mm with 10 mm SHCC overlay |
| SW330-15 | Shear wall specimen wall thickness 330 mm with 15 mm SHCC overlay |
| SW330-30 | Shear wall specimen wall thickness 330 mm with 30 mm SHCC overlay |

Strain diagrams of the shear walls are displayed, presenting mechanisms under which the shear wall specimens (SWS) fail. Failure mechanisms such as shear failure on the diagonal and flexural failure, which include toe crushing as well as corner tearing are observed.

3.2.1 Bare masonry shear walls without retrofitting overlay

The shear force vs displacement diagrams of masonry walls with varying thicknesses and no SHCC overlay are presented in Figure 3.11. The dashed lines present the experimental results of the SW110-0 and SW220-0 obtained by De Beer (2016). It is observed that an increase in masonry thickness leads to a higher shear wall resistance as expected.

The computed results are in reasonable agreement with the experimental results. The SW220-0 model displays a good average between the two experimental results. A slight delayed strain-softening

response of the SW110-0 computational model is observed. Note that only one experimental test was performed on the SW110-0, whereby further calibration of this wall model is not justified. Thus, the results obtained from the computational models on the masonry walls with no retrofitting overlay are believed to represent the actual walls to a sufficient level of accuracy. Note that no experimental tests were performed on the SW330-0, but a computational analysis is nevertheless performed, as triple leaf masonry walls are regularly present in four-story ULM buildings.

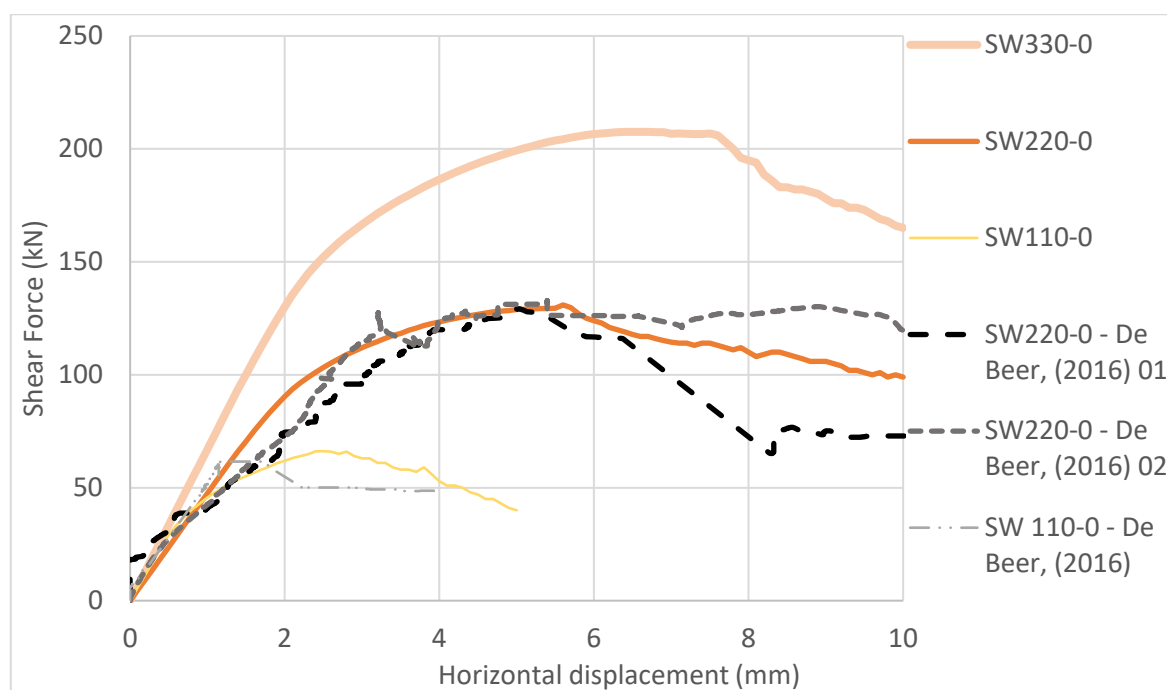


Figure 3.11: Shear force-displacement diagram of shear wall with no retrofitting overlay.

For the SW110-0 model, a maximum shear resistance of 66.2 kN is computed at a displacement of 2.5 mm, SW220-0 has a maximum of 130.94 kN at 5.6 mm, while the SW330-0 is computed to have a peak shear resistance of 208.55 kN at 7.4 mm. The computed and experimental peak shear forces and their corresponding displacement values are tabulated in Table 3.5.

Table 3.5: Peak shear force with its corresponding displacement values of shear wall with no retrofitting overlay.

| | Shear Force (kN) | Displacement (mm) |
|------------------------------|------------------|-------------------|
| SW110-0 | 66.20 | 2.52 |
| SW220-0 | 130.94 | 5.61 |
| SW330-0 | 208.55 | 7.43 |
| SW110-0 – De Beer, (2016) | 62.14 | 1.72 |
| SW220-0 – De Beer, (2016) 01 | 129.24 | 5.03 |
| SW220-0 – De Beer, (2016) 02 | 132.84 | 5.39 |

The computational shear walls show a 97% increase in shear force from the 110 mm wall thickness to the 220 mm thickness, whereas a 60% increase is observed from the 220 mm wall thickness to the 330 mm thickness.

3.2.1.1 Failure mechanisms

The failure mechanisms of the SW220-0 are presented in this section. Similar failure mechanism diagrams of the SW110-0 and SW330-0 are shown in Appendix A. The diagrams of the masonry wall on its own, i.e. without SHCC overlay are displayed.

Figure 3.12 shows the failure mechanisms observed from one of the SW220-0 experimental specimens tested by De Beer (2016). Crack formation is visible on the diagonal indicating the presence of shear failure. A crack also formed in the bottom right hand corner, indicating tip over response.

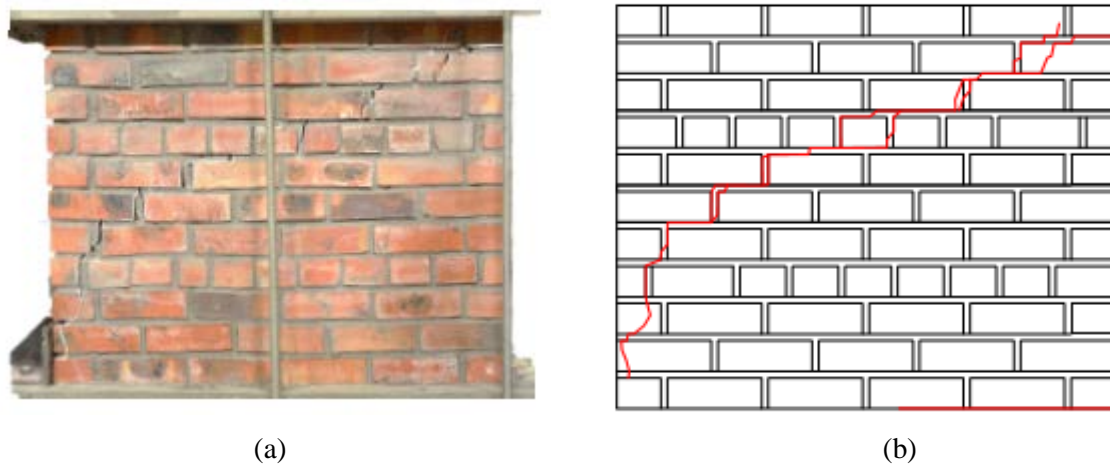


Figure 3.12: Failure mechanisms of SW220-0 experimental test; (a) Cracked experimental specimen; (b) Documented visualisation of the crack formation (De Beer, 2016).

Figure 3.13 shows the principle strains ($E1$) of the SW220-0 at different load steps (displacements). The computational model illustrates similar results to those of the experimental tests. The formation of flexural strains in the top left and bottom right-hand corners are observed, with high diagonal strains forming as the displacement increases. The computed principle strains increase with increasing wall thickness, Appendix A.

Figure 3.13 (a) shows the principle strains at a displacement of 1.5 mm, whereas (b) is at the ultimate shear strength at a displacement of 5.6 mm. The strain diagrams of Figure 3.13 (c), (d) and (e) represent the strain softening zone of the force-displacement curve. A maximum principle strain of 0.42 is obtained at 10 mm displacement, Figure 3.13 (e).

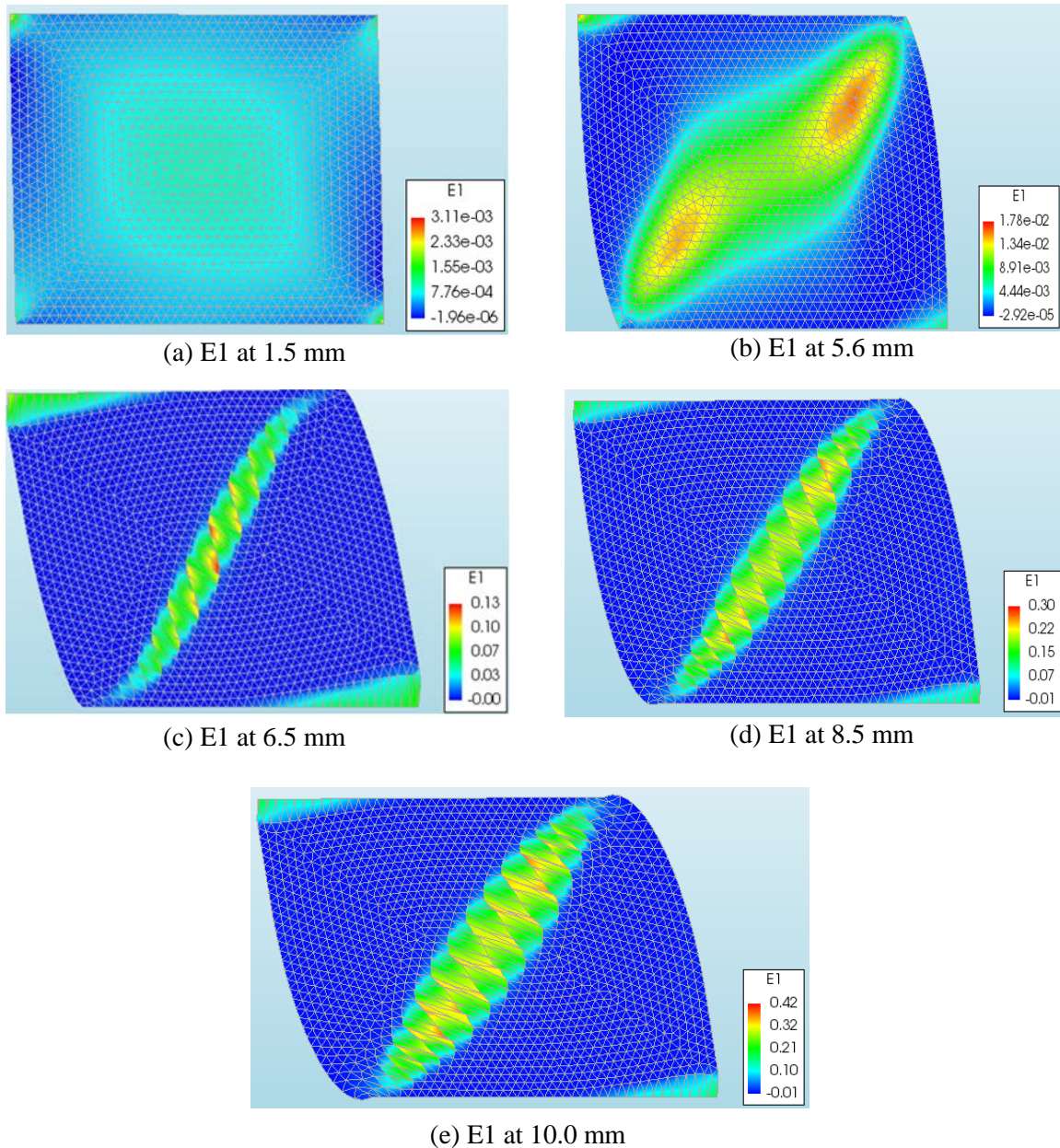


Figure 3.13: Principle strains (E1) of SW220-0 at different top horizontal displacements.

The vertical pre-stressing forces in the rods should exceed the tip-over moment created by the horizontal load, while flexural forces are limited for the shear force to distribute through the diagonal. High rotation forces may cause toe crushing of the masonry without any shear failure on the diagonal. Therefore, care should be given on the pre-tension forces to limit the occurrence of tip-over and hereby toe crushing.

The experimental results on the SW220-0 display limited crushing on the toes of the wall, but with it being observed to a larger extent on the SW110-0. Limited toe crushing is computed in the nonlinear analyses of this research. A moderate increase in toe crushing is observed from the SW110-0 model, Appendix A.

The vertical compressive stress (S_{yy}) diagrams of the SW220-0 model are displayed in Figure 3.14. The maximum compressive stress of 20 MPa is not breached in the 10 mm displacement. At a lower displacement, higher concentrated stresses on the corner are observed, with the stresses distributing more towards the inside of the wall as the displacement increases.

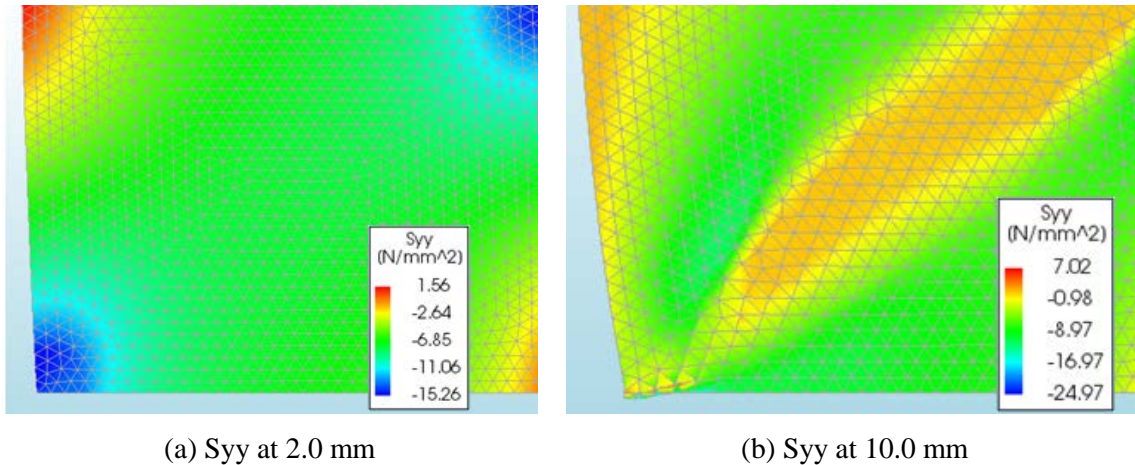


Figure 3.14: Compressive stress (S_{yy}) diagrams of the SW220-0 model at different pull-over displacements.

The principle vertical stress (S_2) diagrams of the SW220-0 at 2 mm and 10 mm displacements are displayed in Figure 3.15 (a) and (b) respectively. The minimum principle stress (maximum principle compressive stress) in the masonry wall is less than its compressive resistance of 20 MPa. Due to these observations on the maximum compressive stress, the pre-tension forces in the steel rods can be validated to limit rotational movement of the masonry shear wall. Similar stress diagrams of the SW110-0 and SW330-0 models are present in Appendix A. Note, the negative sign convention in the S_{yy} and S_2 diagrams indicates compression.

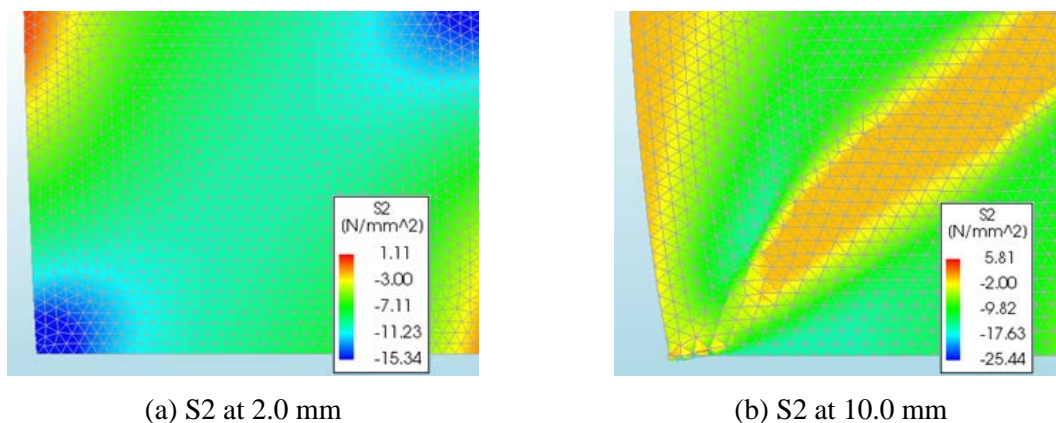


Figure 3.15: Principle Vertical stress (S_2) in SW220-0 at varying pull-over displacements.

3.2.2 Masonry shear walls retrofitted with SHCC

In this section, the computational results of the double leaf masonry shear wall retrofitted with 15 mm SHCC overlay are compared with the experimental results obtained by De Beer (2016) and discussed. Computational models with the same masonry and SHCC thickness, including models with different thicknesses are presented. Shear force vs horizontal displacement diagrams as well as diagrams displaying the failure mechanisms are presented.

3.2.2.1 SW220-15

Figure 3.16 displays the results of the 220 mm masonry shear walls retrofitted with 15 mm SHCC overlay. The dashed lines present the experimental results obtained by De Beer (2016), while the solid line presents the computed results of the computational model. A large variation in the second rising branch, a result of stiffness reduction, is observed for the three identical shear walls tested by De Beer (2016). The computed response of the SW220-15 analysis does not capture similar behaviour within this region. However, a reasonable representation of the mean ultimate shear strength with its associated displacement is obtained by the computed results. The computed post-peak behaviour of the analysis displays a reasonably similar response to the experimental results.

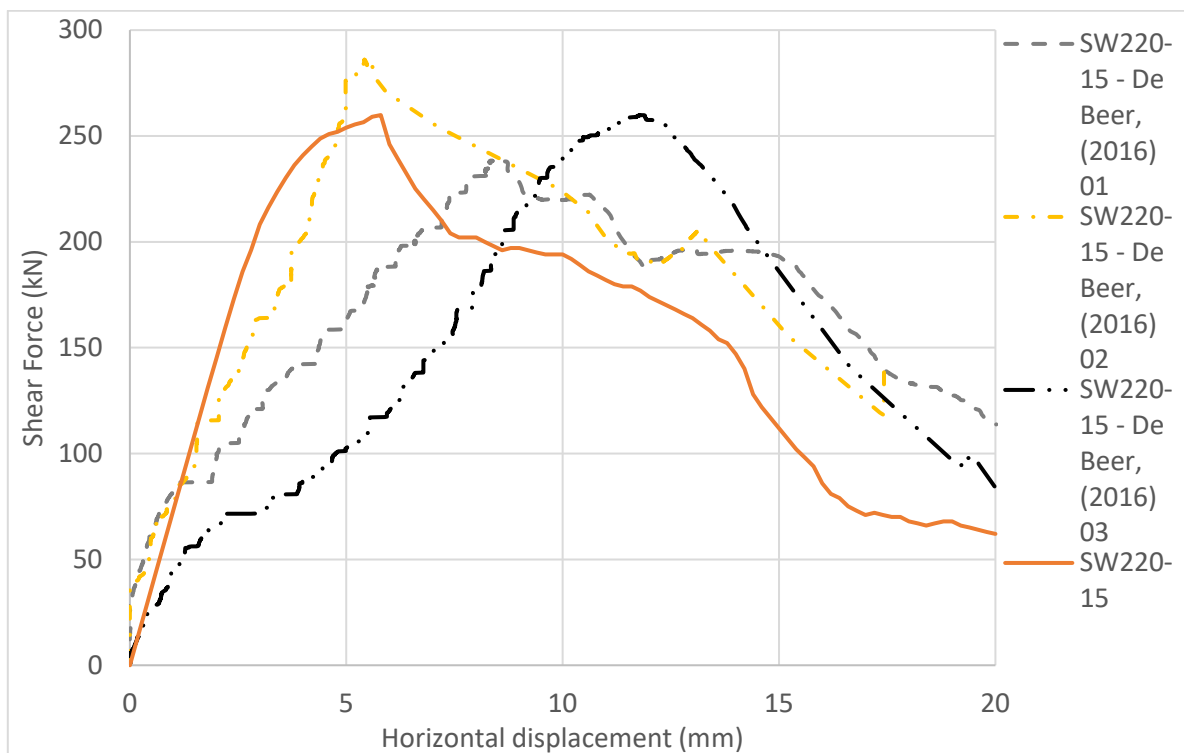


Figure 3.16: Shear force vs horizontal displacement diagram of 220 mm thick shear wall retrofitted with 15mm SHCC overlay.

The computational SW220-15 model reaches an ultimate shear resistance of 259.88 kN at a displacement of 5.8 mm. The ultimate shear strength and associated displacement are increased by 128.94 kN and 0.2 mm with the provision of a 15 mm SHCC overlay. The maximum shear resistance shows a 98.5% rise with its associated displacement showing a 3.6% rise.

Due to the reasonable agreement between the computed and observed responses, the finite element models to analyse the reference wall as well as the enhanced shear performance with the application of an SHCC overlay as a retrofitting strategy are considered to be calibrated to an acceptable degree.

The principle strain (E1) diagrams of the 220 mm masonry wall retrofitted with 15 mm overlay are presented in Figure 3.17. Only the strains of the SHCC overlay are displayed. Figure 3.17 (a) presents the strains at 3.5 mm displacement with the strains obtained at the ultimate shear force of 259.88 kN with its associated 5.8 mm displacement, being presented in Figure 3.17 (b). Figure 3.17 (c), (d), (e) and (f) present the strains in the descending softening phase at 9 mm, 12 mm, 17.5 mm and 20 mm. At 20 mm displacement the maximum strain is 0.5.

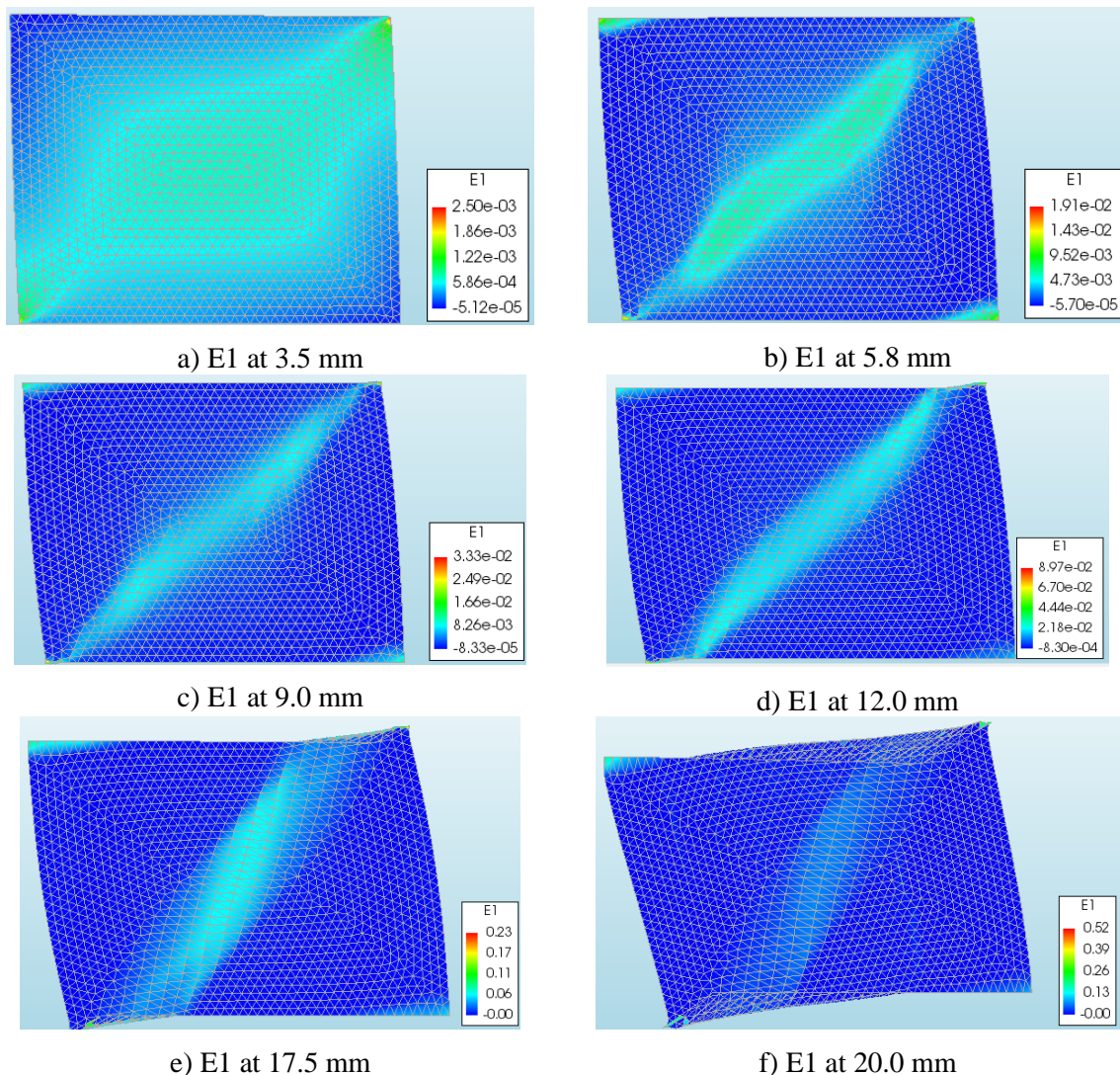


Figure 3.17: Principle strains (E1) of SW220-15 at different horizontal displacements.

The principle vertical stress (S_2) and vertical compressive stress (S_{yy}) in the SHCC overlay of the SW220-15 model are displayed on the left and right of Figure 3.18. The top row, Figure 3.18 (a) and (b), is the presentation at 5.5 mm displacement, while the analysis is still in the hardening phase. The compressive stress of 20 MPa is not yet breached in this stage. The middle row displays the stresses in the softening phase at a displacement of 7.5 mm. Higher principle vertical stresses and compressive stresses are obtained in this region, but the shear wall is still only subjected to shear and flexural failure. The bottom row presents the diagrams in the second descending branch of the force-displacement diagram, Figure 3.16, at a displacement of 19.5 mm. In this region the ultimate compressive resistance is breached. Figure 3.18 (e) shows a principle vertical stress of 22.31 MPa, indicating the occurrence of toe crushing to a limited extent. It can also be seen that the compressive stresses, originated in the bottom left and top right corners, move towards the middle of the shear wall as the load increases.

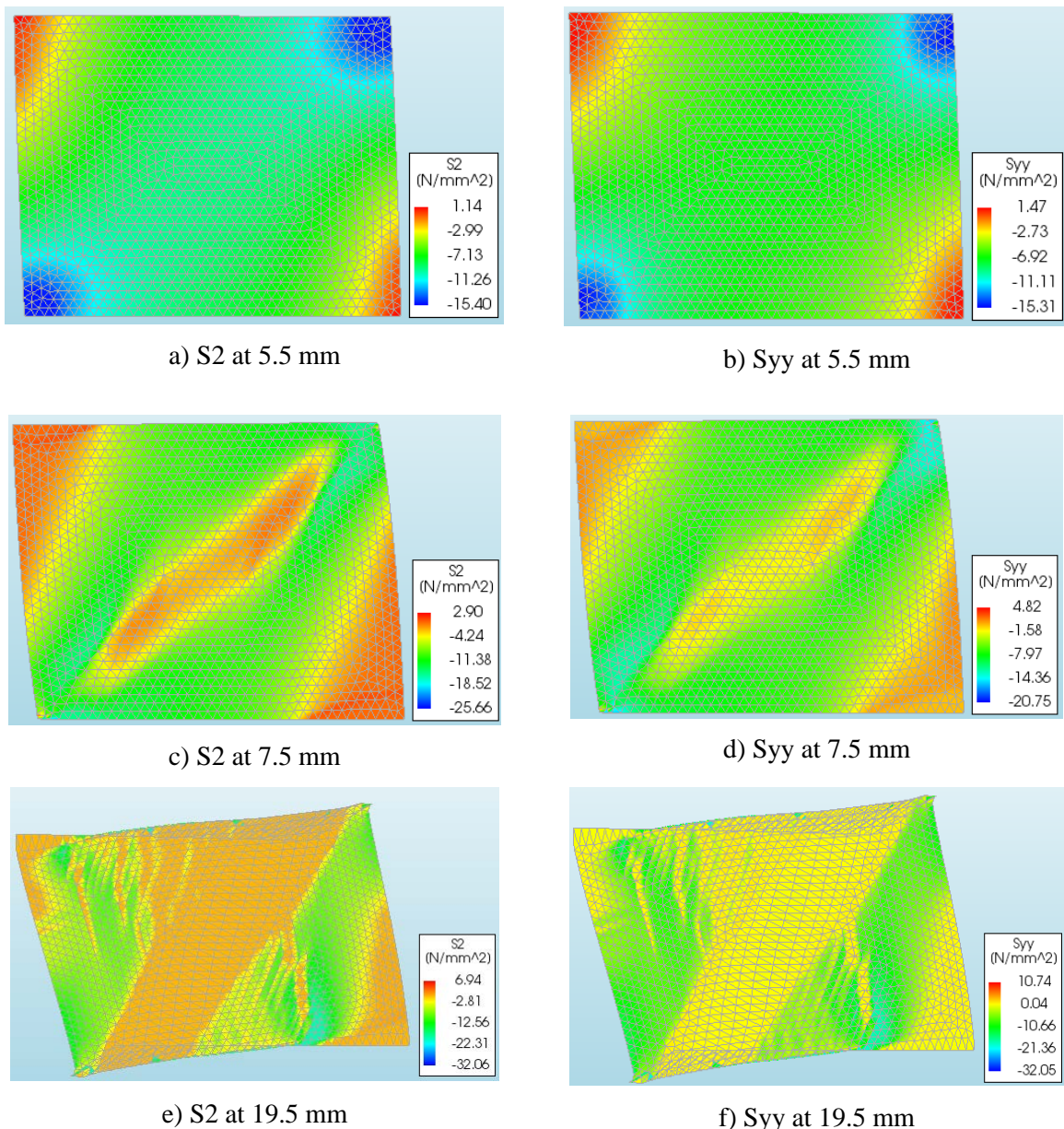


Figure 3.18: The principle vertical stress (S_2) and compressive stress (S_{yy}) of the SW220-15 model.

3.2.2.2 SW220-10, SW220-15 and SW220-30

This section presents the results of a 220 mm double leaf masonry wall retrofitted with different SHCC overlay thicknesses. A 10 mm and 30 mm SHCC overlay are analysed and compared to the results of the SW220-15 mentioned above. Note, De Beer (2016) did not perform experimental tests on the SW220-10 and SW220-30 models presented in this section. The scope of this section is to computationally investigate the behaviour of a 220 mm masonry wall when retrofitted with SHCC overlay thicknesses varying from that of the experimental study performed by De Beer (2016).

Figure 3.18 presents the shear force-displacement behaviour of the 220 mm masonry wall retrofitted with varying SHCC overlay thicknesses. As expected, an increase in shear force is obtained with an increase in overlay thickness. The SW220-10 model has a maximum shear resistance of 243.45 kN at a displacement of 5.2 mm with the SW220-30 model obtaining a maximum shear resistance of 279.64 kN at a displacement of 6.0 mm. Higher ultimate shear strength and associated displacement of 16.43 kN and 0.6 mm are obtained from the SW220-10 to SW220-15 models. From the SW220-15 to SW220-30 models, higher ultimate shear resistance of 19.76 kN and 0.2 mm associated displacement are obtained.

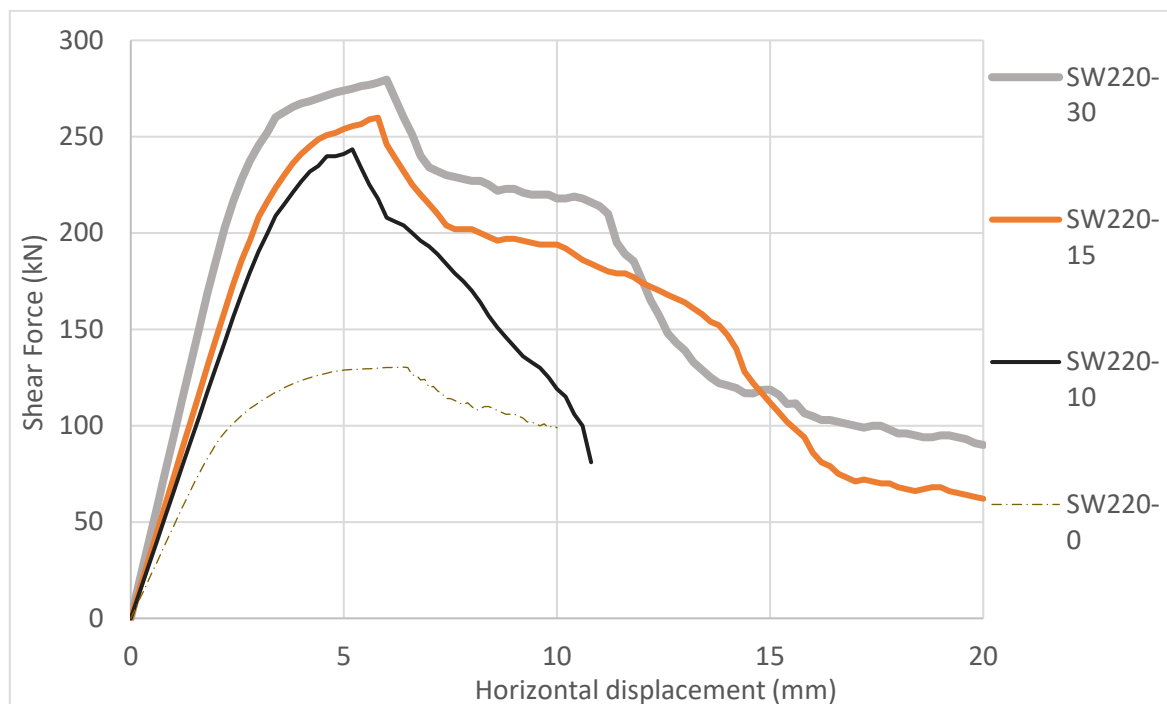


Figure 3.19: Shear force-displacement diagram of SW220-10, SW220-15 and SW220-30.

The principle strain (ϵ_1) diagrams of the 220 mm masonry wall retrofitted with 30 mm overlay are presented in Figure 3.20. Similar strain diagrams of the SW220-10 model are presented in Appendix A. Only the strains of the SHCC overlay are displayed. Figure 3.20 (a) presents the strains at 3.8 mm displacement, with the strains obtained at the ultimate shear force and associated 6.0 mm displacement presented in Figure 3.20 (b). Figure 3.20 (c), (d), (e) and (f) present the strains in the softening phase at

6.5, 8, 15.2 and 20 mm displacements respectively. At 20 mm displacement, the maximum strain is 1.13, implicating an excessively wide diagonal crack. Note that the same, automated deformation magnifying scale is used in these visualisations of the deformed SHCC overlay, leading to the distorted deformations in Figure 3.20 (e) and (f) when localisation of deformation occurs in the latter regions of the softening response.

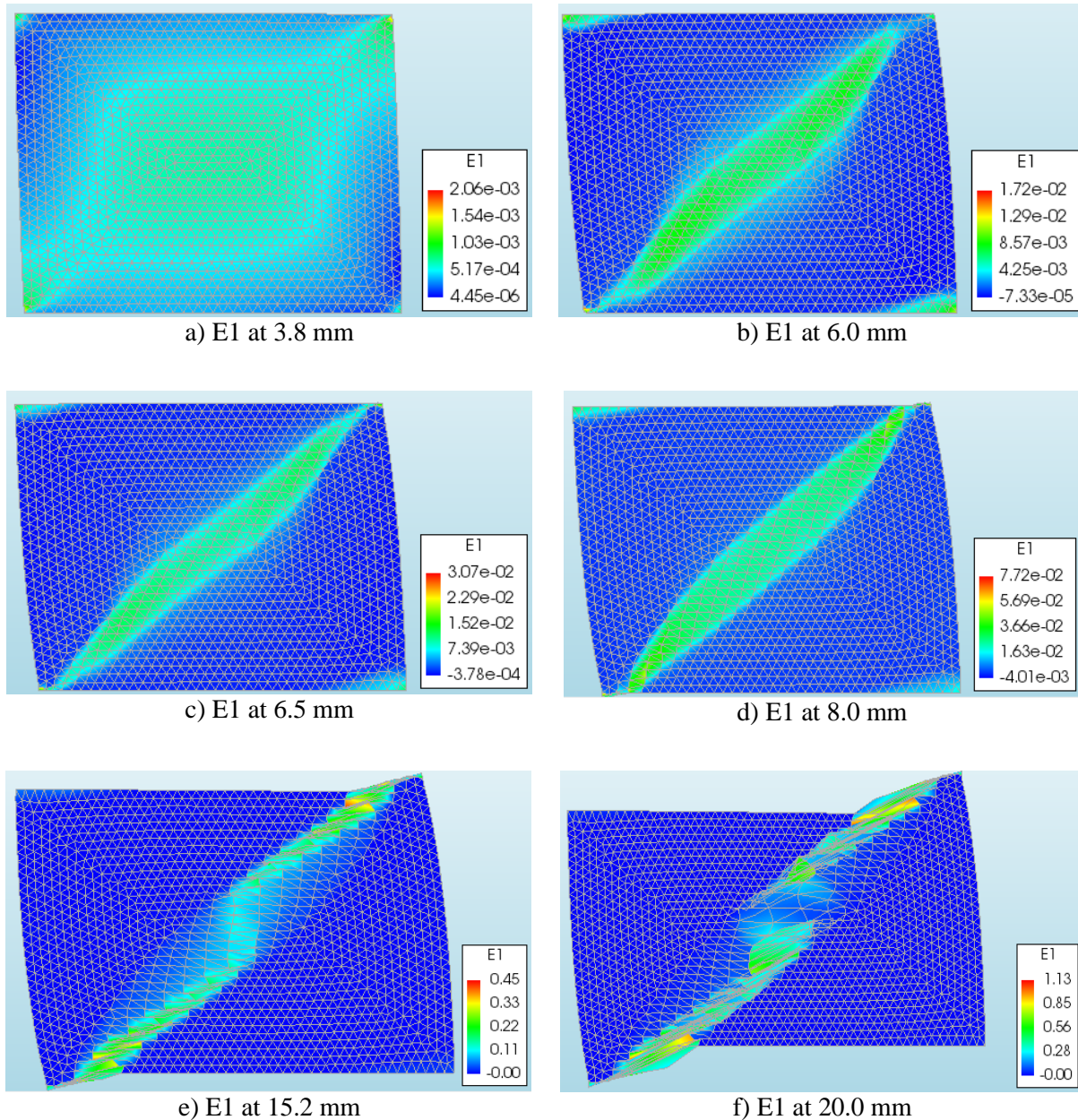


Figure 3.20: Principle strain diagrams of SW220-30 model.

The principle vertical stress (S_2) and compressive stress (S_{yy}) of the SW220-30 model are displayed on the left and right respectively of Figure 3.21. The top row, Figure 3.21 (a) and (b), is the presentation at 5.8 mm, while the shear wall is still in the hardening phase. The compressive resistance of 20 MPa is

not yet breached at this step. The middle row displays the stresses in the second descending branch of the softening phase at a displacement of 12.0 mm. Higher principle vertical stresses and compressive stresses are obtained in this region. The principle vertical stresses are higher than the 20 MPa compressive resistance, indicating the occurrence of limited toe crushing. The bottom row presents the compressive and vertical principle stress moving to the middle of the shear wall at a displacement of 19.5 mm. Similar diagrams of the SW220-10 model are presented in Appendix A.

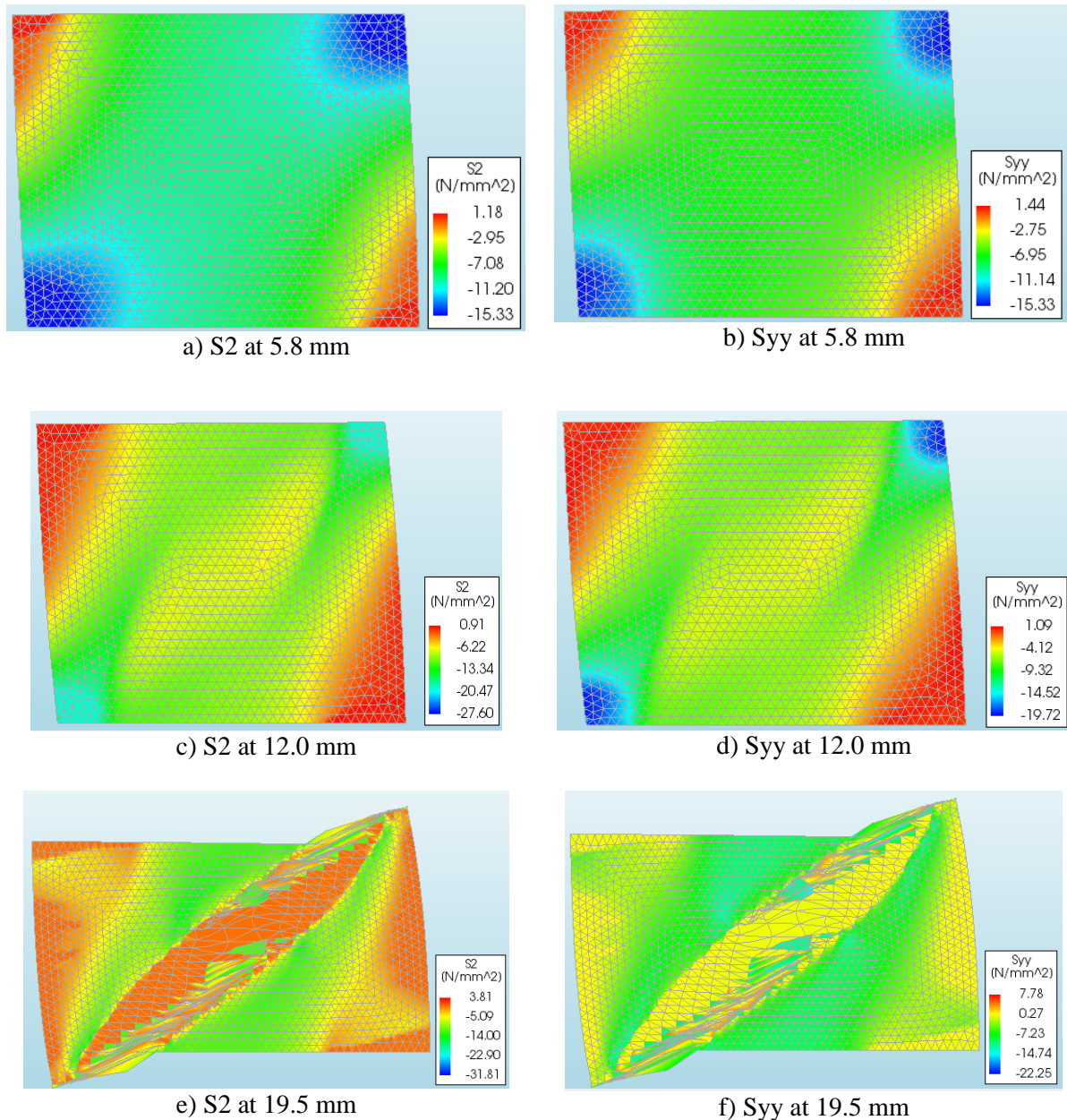


Figure 3.21: The principle vertical stress (S_2) and compressive stress (S_{yy}) of the SW220-30 model.

3.2.2.3 SW110-10, SW110-15 and SW110-30

This section presents the results of a 110 mm single leaf masonry wall retrofitted with different SHCC overlay thicknesses. SHCC overlays of 10, 15 and 30 mm thickness are analysed and compared. Note, De Beer (2016) did not perform experimental tests on the SW110-10 and SW110-15 walls, but did however on the SW110-30 wall.

Figure 3.22 presents the shear force-displacement behaviour of the 110 mm masonry wall retrofitted with varying SHCC thicknesses. The SW110-0 model without SHCC overlay is presented with a dashed line. As expected, an increase in shear force is obtained with an increase in overlay thickness. The SW110-10 model has a maximum shear resistance of 112.47 kN at a displacement of 2.8 mm, SW110-15 shows a maximum shear resistance of 148.65 kN at a displacement of 3.2 mm, with SW110-30 obtaining a maximum shear force of 199.56 kN at 3.6 mm. The ultimate shear strength and associated displacement is higher with 36.18 kN and 0.4 mm respectively from the SW110-10 to SW110-15 models. From the SW110-15 to SW110-30 models, higher ultimate shear resistance of 50.91 kN and 0.4 mm associated displacement are obtained. The maximum shear force and displacement of the SW110-0 model increase with 82.44 kN and 0.7 mm when retrofitted with a 15 mm overlay.

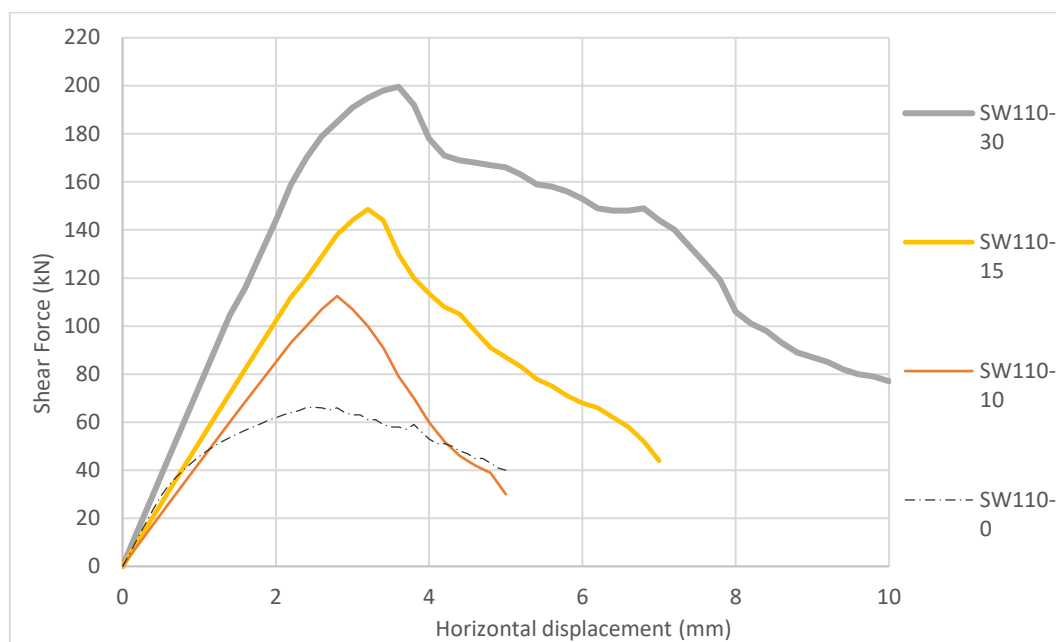


Figure 3.22: Shear force-displacement diagram of SW110-10, SW110-15 and SW110-30.

The principle strain diagrams of the SW110-30 model are presented in Figure 3.23 with similar diagrams of the SW110-10 and SW110-15 models displayed in Appendix A. Figure 3.23 (a) and (b) present the strains in the hardening phase at 1.8 mm and 3.4 mm displacements respectively. Figure 3.23 (c) and (d) present the strains in the softening phase at 4.8 mm and 9.6 mm.

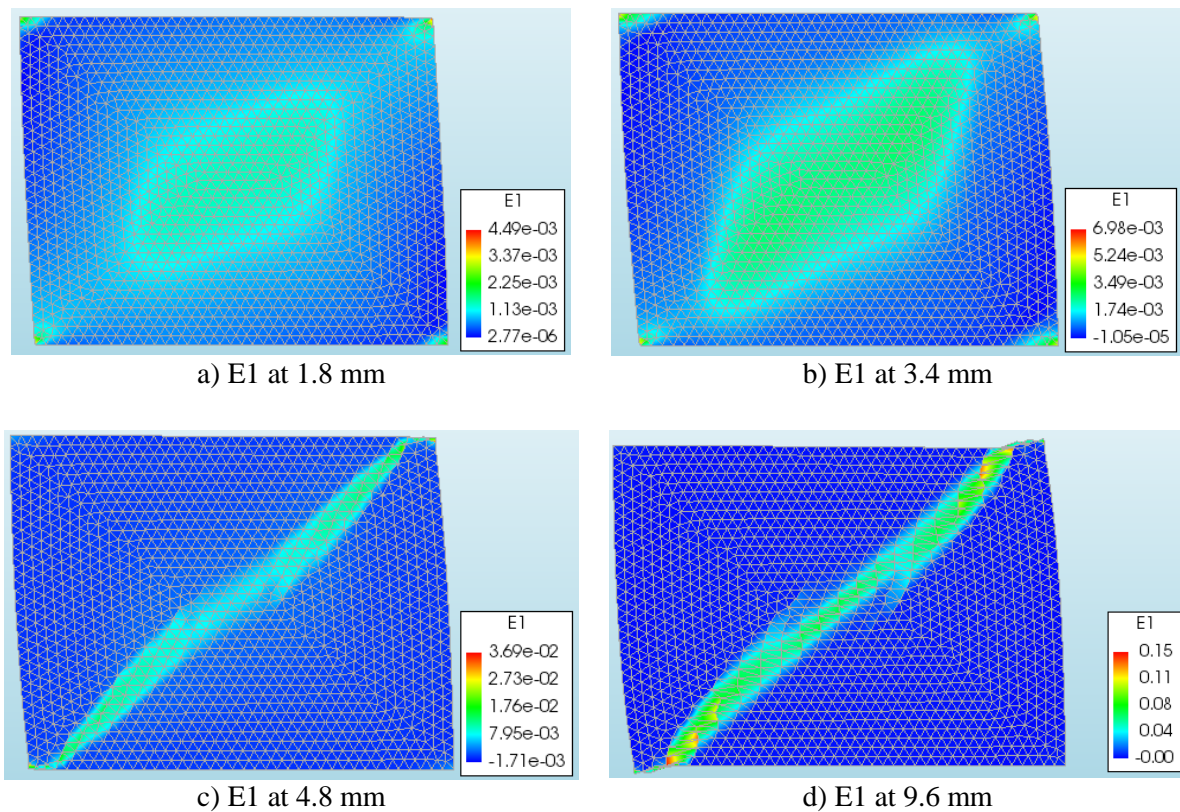
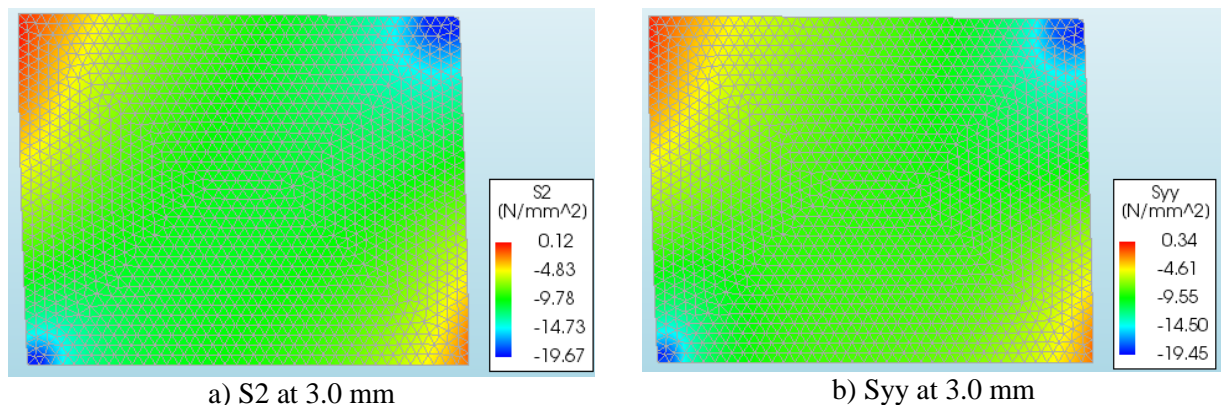


Figure 3.23: Principle strain diagrams of SW110-30 model.

The principle vertical stress (S_2) and compressive stress (S_{yy}) of the SW110-30 model are displayed on the left and right respectively in Figure 3.24. The top row, Figure 3.24 (a) and (b), is the presentation at 3 mm, while the shear wall is still in the hardening phase. The compressive resistance of 20 MPa is not yet breached at this step. The bottom row displays the stresses in the second descending branch of the softening phase at a displacement of 7.8 mm. Higher principle vertical stresses and compressive stresses are obtained in this region. The principle vertical stresses are higher than the 20 MPa compressive resistance, indicating the occurrence of toe crushing. Similar diagrams of the SW110-10 and SW110-15 models are present in Appendix A.



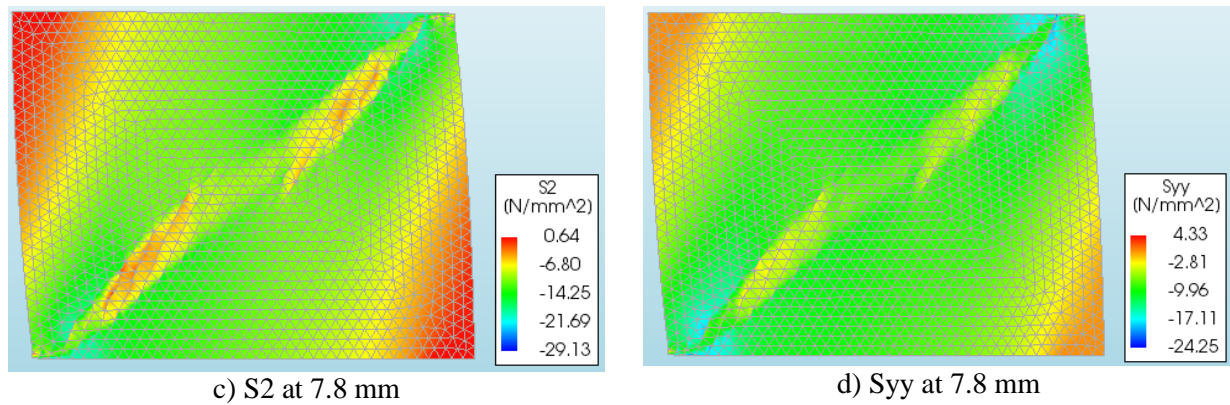


Figure 3.24: The principle vertical stress (S2) and compressive stress (Syy) of the SW110-30 model.

3.2.2.4 SW330-10, SW330-15 and SW330-30

This section presents the results of a 330 mm triple leaf masonry wall retrofitted with different SHCC overlay thicknesses. SHCC overlays of 10, 15 and 30 mm thicknesses are analysed and compared to the results of the SW330-0 model. Note, De Beer (2016) did not perform experimental tests on any of the models presented in this section. The scope of this section is to simulate the response of a 330 mm masonry wall when retrofitted with different SHCC overlay thicknesses.

Figure 3.25 displays the shear force-displacement behaviour of the 330 mm masonry wall retrofitted with varying SHCC thicknesses. The SW330-0 model is presented with a dashed line. As expected, an increase in shear force is obtained with an increase in overlay thickness. However, a lower increase in shear force from the 10 mm overlay to 30 mm is obtained from the triple leaf masonry wall than from the double leaf masonry wall. Note, the associated displacement at maximum shear force is decreased with increasing overlay thickness. The SW330-10 model has a maximum shear resistance of 286.94 kN at a displacement of 5 mm, SW330-15 shows a maximum shear resistance of 290.31 kN at a displacement of 4.8 mm, with SW330-30 showing a maximum shear force of 296.06 kN at 4.2 mm. The ultimate shear strength increases with 3.37 kN and the associated displacement decreases with 0.2 mm from the SW330-10 to SW330-15 models. From the SW330-15 to SW330-30 models, higher ultimate shear resistance of 5.75 kN and a decreased associated displacement of 0.6 mm are obtained. The maximum shear force of the SW330-0 model increases with 81.76 kN and the associated displacement decreases with 2.6 mm when retrofitted with a 15 mm overlay.

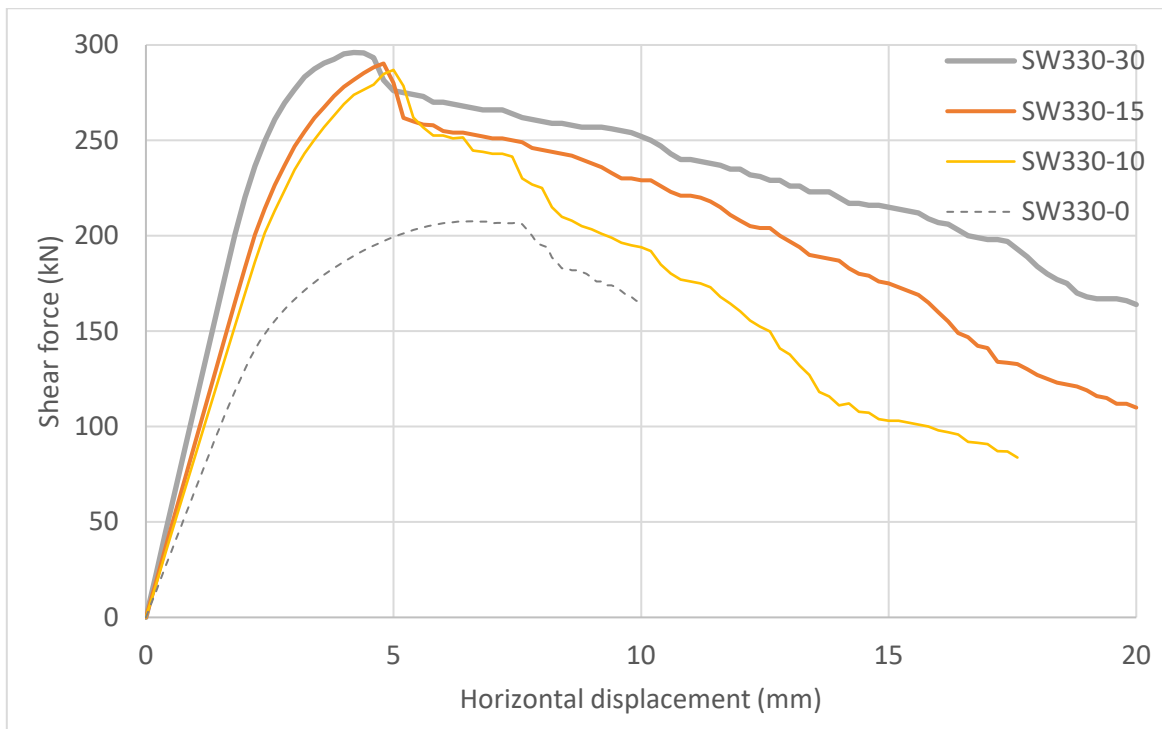


Figure 3.25: Shear force-displacement diagram of SW330-10, SW330-15 and SW330-30.

The principle strain diagrams of the SW330-15 model are presented in Figure 3.26, with similar diagrams of the SW330-10 and SW330-30 models displayed in Appendix A. Figure 3.26 (a) presents the strains in the hardening phase at a displacement of 4.5 mm. Figure 3.26 (b), (c) and (d) present the strains in the softening phase at 5.4 mm, 14 mm and 19.5 mm horizontal displacements respectively.

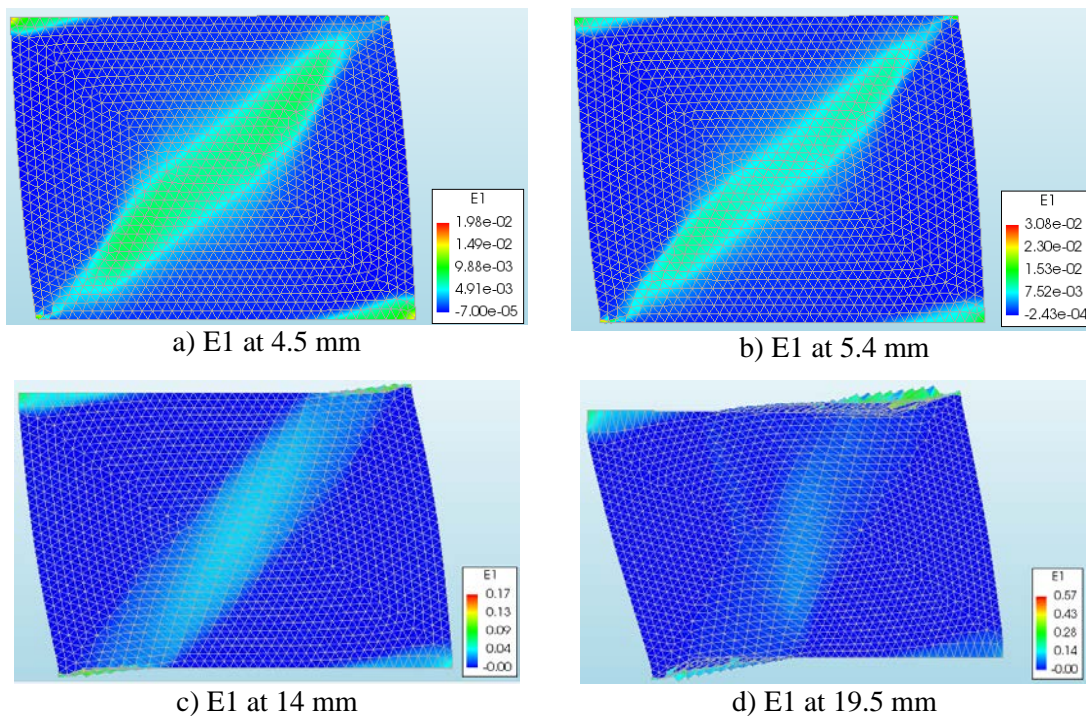


Figure 3.26: Principle strain diagrams of SW330-15 model

The principle vertical stress (S_2) and compressive stress (S_{yy}) of the SW330-15 model are displayed on the left and right respectively in Figure 3.27. The top row, Figure 3.27 (a) and (b), is the presentation at 4.0 mm displacement, while the shear wall is still in the hardening phase. The compressive stress of 20 MPa is not breached at this step. The bottom row displays the stresses in the second descending branch of the softening phase at a displacement of 20.0 mm. Higher principle vertical stresses and compressive stresses are obtained in this region. The principle vertical stresses has not breached the 20 MPa compressive resistance, indicating no occurrence of toe crushing. Similar diagrams of the SW330-10 and SW330-30 models are present in Appendix A.

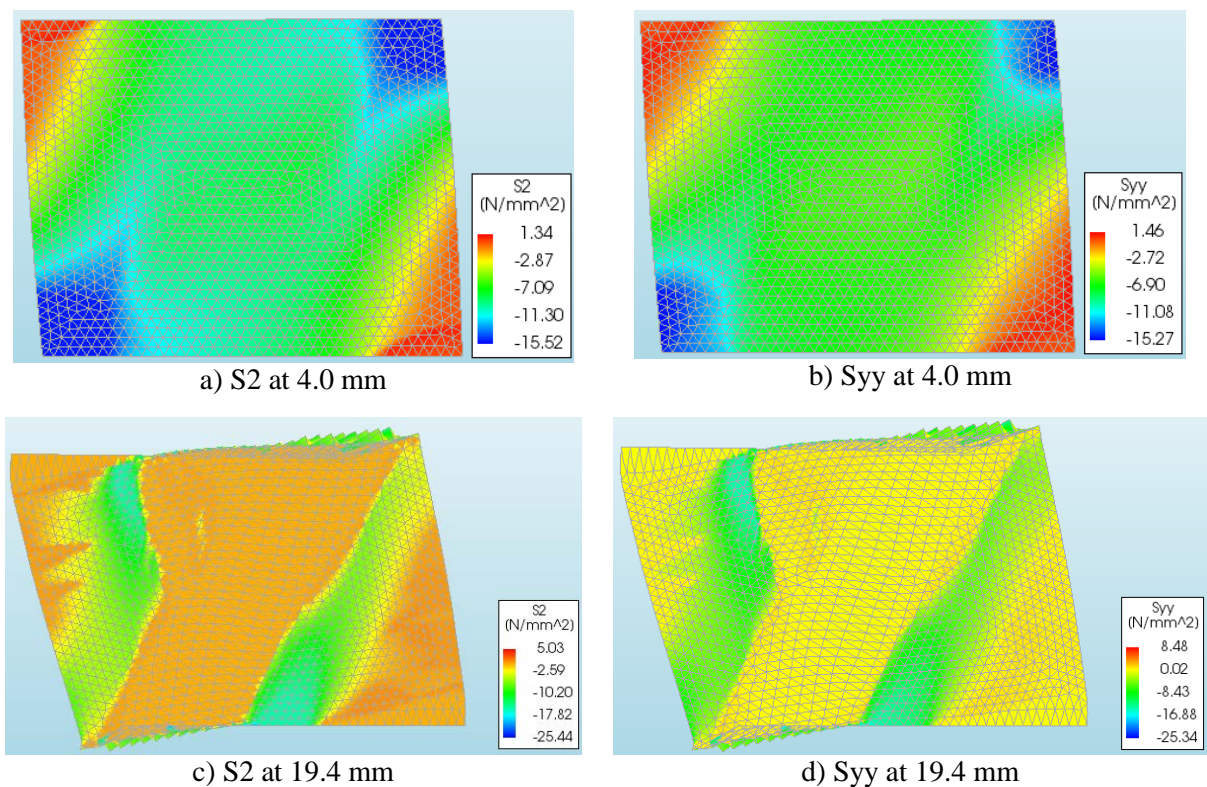


Figure 3.27: The principle vertical stress (S_2) and compressive stress (S_{yy}) of the SW330-15 model.

3.3 Conclusions and recommendations

Computational modelling has been presented of a retrofitting strategy of an SHCC overlay sprayed on masonry walls to improve in-plane shear resistance, and thereby their seismic resistance. The computed results have been compared to experimental results obtained by De Beer (2016) at SUN. Table 3.6 shows a summary of the results obtained by the computational models and the experimental tests.

Table 3.6: Summary of computed and experimental tests on shear walls with and without SHCC overlay.

| | Ultimate Shear Force (kN) | Ultimate Shear Stress (MPa) | Associated Displacement (mm) |
|------------------------------|---------------------------|-----------------------------|------------------------------|
| SW110-0 | 66.20 | 0.52 | 2.50 |
| SW110-0, De Beer, (2016) | 62.14 | 0.49 | 1.72 |
| SW110-10 | 112.47 | 0.89 | 2.80 |
| SW110-15 | 148.65 | 1.18 | 3.20 |
| SW110-30 | 199.56 | 1.58 | 3.60 |
| SW220-0 | 130.94 | 0.52 | 5.60 |
| SW220-0, De Beer, (2016) | 132.84 | 0.53 | 5.39 |
| SW220-10 | 243.45 | 0.96 | 5.20 |
| SW220-15 | 259.88 | 1.03 | 5.80 |
| SW220-15, De Beer, (2016) 01 | 235.28 | 0.93 | 8.24 |
| SW220-15, De Beer, (2016)02 | 283.62 | 1.12 | 5.38 |
| SW220-15, De Beer, (2016) 03 | 259.80 | 1.03 | 11.82 |
| SW220-30 | 279.64 | 1.11 | 6.00 |
| SW330-0 | 208.55 | 0.55 | 7.40 |
| SW330-10 | 286.94 | 0.76 | 5.00 |
| SW330-15 | 290.31 | 0.76 | 4.80 |
| SW330-30 | 296.06 | 0.78 | 4.20 |

The following conclusions are drawn from the results obtained from the nonlinear computational analyses performed on varying thickness masonry shear walls retrofitted with different SHCC overlay thicknesses:

- The behaviour of the bare, reference shear walls, i.e. without SHCC overlay has been simulated computationally with reasonable accuracy. As expected, the bare masonry shear walls showed an increase in ultimate shear resistance with an increase in wall thickness.

- A large variation in the stiffness reduction of the second rising branch is observed for the three identical retrofitted shear walls tested by De Beer (2016). The computed response of the SW220-15 analysis does not capture similar behaviour within this region. However, a reasonable representation of the mean ultimate shear strength with its associated displacement is obtained by the computed results.
- A significant increase of 98.5% in the ultimate shear strength from a bare shear wall compared with a wall retrofitted with a 15 mm SHCC overlay is obtained, proving the enhanced benefits of the composite material when subjected to a seismic loading regime.
- The 110, 220 and 330 mm masonry walls showed an increase in shear resistance with an increase in SHCC overlay thickness. However, a decreased rise in shear strength is observed with increasing wall thickness for the same overlay thicknesses varying between 10 and 30 mm.
- A reduced shear force is obtained as the masonry thickness increases when retrofitted with a 15 mm SHCC overlay.
- Due to reasonable agreement between the computed reference and retrofitted shear wall responses and those observed from the experimental shear walls tested by De Beer (2016), the computational models are considered to be suitably calibrated.

A significantly enhanced shearing ductility performance is not yet obtained with the application of an SHCC overlay, as the shear force currently reduces at a high rate in the softening phase. The next step is to increase the ductility by applying a balanced interface behaviour (as discussed in Section 2.9.3). This is done by applying debonded strips on the diagonal, where localised cracks form, for an enlarged cracking area within the SHCC overlay to be obtained. The strain-hardening behaviour exhibited by the SHCC material may be better exploited with this enlarged crack distribution. The following section discusses the detailed nonlinear analysis and preparation of the experimental tests performed in order to obtain higher ductility when retrofitting with SHCC overlay.

Chapter 4

Computational Prediction and Experimental Validation

Design of Strip Debonded Overlay

This chapter presents the strategy of the masonry shear walls retrofitted with SHCC overlay and debonded strip interfaces for obtaining enhanced ductility. Detailed nonlinear finite element analyses are performed, and the debonded strip setup and computed results of the shear force vs displacement and failure mechanisms discussed. Validating experimental specimens are designed with the same size as previously tested by de Beer (2016) at Stellenbosch University. An appropriate combination of strip width (W) and centre to centre spacing (S), shown in Figure 4.1, are investigated for maximum ductility to be obtained. The DIANA FEA software is used for the execution of the detailed nonlinear analyses, extrapolating the calibrated model from the previous chapter. This chapter is divided into three sections:

1. Setup and results of the masonry shear wall with debonded strip interfaces, retrofitted with SHCC overlay, DIANA FEA model.
2. Experimental SHCC overlay and debonded strips spray-ability and adherence testing.
3. Application of SHCC overlay and debonded strips on shear walls and the testing rig setup.

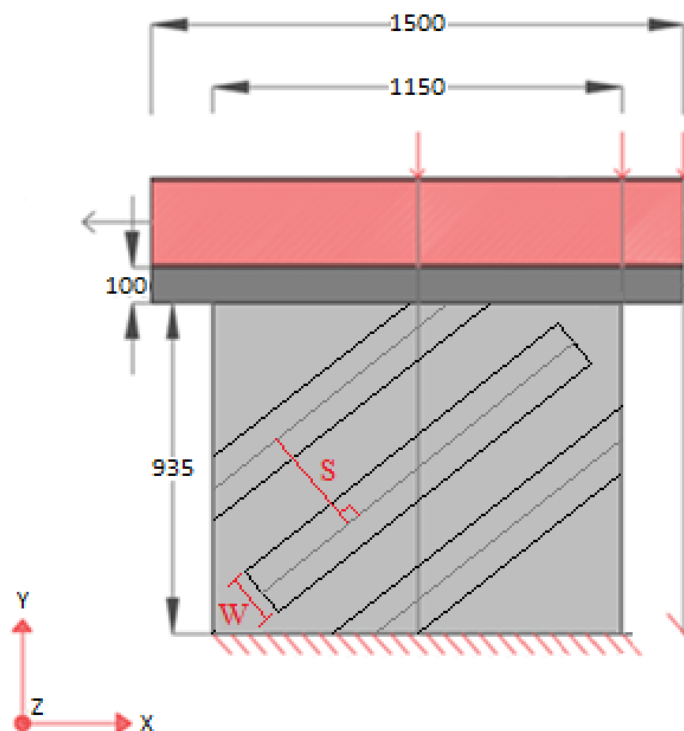


Figure 4.1: Debonded strip model layout.

4.1 Modelling of shear walls retrofitted with SHCC overlay and debonded strip interfaces

4.1.1 Setup

The geometry of the shear wall setup is similar to that discussed in Section 3.1.1, with the five structural elements i.e. masonry, SHCC, steel rods, concrete beam, and steel beam shown in Figure 3.2. However, the masonry wall model is divided into smaller parts shown in Figure 4.2. Similar to the analyses discussed in Section 3.1, the geometry of the elements, excluding the rods, are defined as sheets with an element class of 3D membranes assigned to them. The three steel rods are defined as 3D line elements. The geometry and materials assigned to all masonry parts are all exactly the same as those described in Section 3.1. A strip interface is assigned to the debonded strip regions to be modelled as unbonded, while a structural masonry-SHCC interface is assigned to the surrounding regions.

The debonded strip created along the diagonal stops 150 mm away from the corners. This is done to avoid delamination of the SHCC overlay as large compressive forces are present at these corners due to the pre-stressing forces of the steel rods and the overturning action during pull-over. For this analysis, all the strips have equal widths (W) of 75 mm. The perpendicular centre to centre spacing (S) of the strips is 150 mm, leaving a 75 mm strip with high bond strength (masonry-SHCC interface) in-between. Smaller spacing holds the risk of uncontrolled delamination of the SHCC overlay, which may lead to ultimate failure of the shear walls without the strain-hardening behaviour mobilised in the SHCC overlay. Different strip widths (75 and 100 mm) and spacing (150 and 200 mm) are experimentally tested and their results are discussed in Section 5.3. The model discussed here with $W = 75$ mm and $S = 150$ mm is analysed to investigate the improved ductility performance when implementing the debonded strip interfaces.

A strip interface material is created and assigned to the debonded strip interface. A 3D plane linear interface material is selected for the debonded strips with artificially low values for the normal stiffness (k_n) in the z-direction and shear stiffnesses (k_s) in the x- and y-directions of 0.001, 0.0001 and 0.0001 N/mm³ respectively. The low stiffness values are chosen to represent a very smooth interface with a low bonding strength compared to that of the masonry-SHCC interface material.

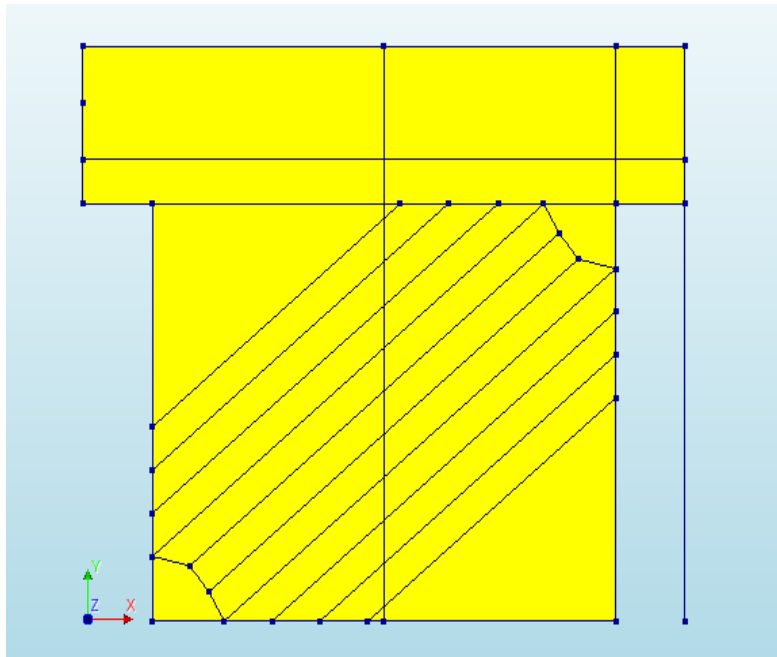


Figure 4.2: Debonded strip model geometry.

Similar boundary conditions and loads to those discussed in Section 3.1 are applied to the model. Therefore, the debonded strip interface is the only different addition in this model. Tetra/triangular elements with a meshing size of 30 mm are used for the computational model as they provide a better alignment of the diagonal strips and also the enhanced capturing of inelastic strains. Figure 3.4 displays the mesh of all the elements in the computational model, where it can be seen that uniform size and shape elements mesh the structural parts. Similar phased analysis procedures to those of Section 3.1 are followed for the execution of the nonlinear structural analysis.

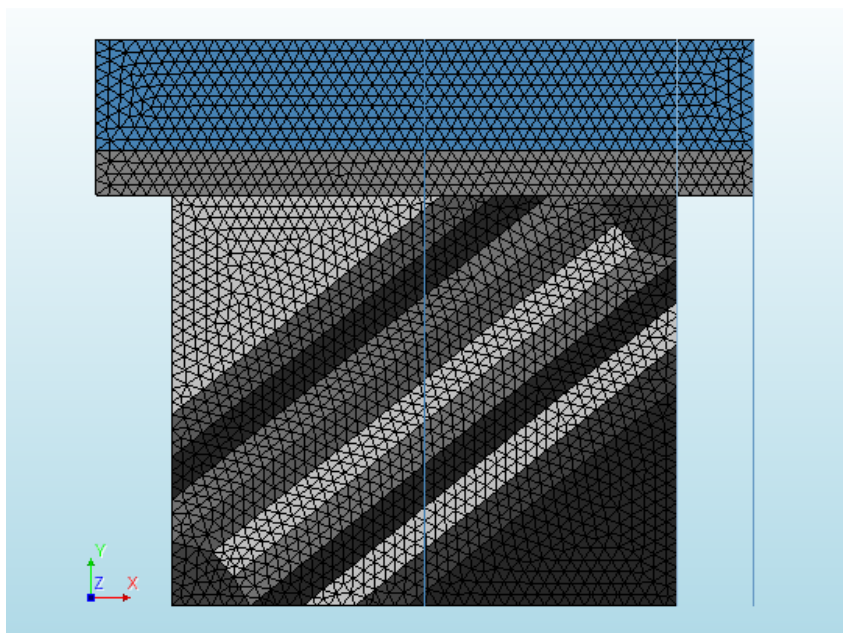


Figure 4.3: Debonded strip model mesh.

4.1.2 Results and discussions

This section presents the results of the analysis performed on the computational model setup discussed in Section 4.1.1. The behaviour of a double leaf masonry shear wall retrofitted with a 15 mm SHCC overlay with the use of the debonded strip interface strategy subjected to seismic loading regimes is tested. However, primary focus is on the increased ductility performance of the shear walls when debonded strip interfaces on the diagonal are used. A shear force vs displacement diagram, along with principle strain and compressive stress diagrams of the 220 mm shear wall retrofitted with 15 mm SHCC overlay and 75 mm debonded strip interfaces with 150 mm centre to centre spacing (SW-75-150-Strip Analysis) are presented in this section.

The computational results are compared with those of the SW220-15 computational model discussed in Section 3.2.2.1. The force-displacement diagrams of the two models are shown in Figure 4.4. The SW-75-150-Strip Analysis model has an ultimate shear strength of 259.96 kN at an associated displacement of 9.8 mm. A similar ultimate shear resistance is obtained when the 75 mm debonding strips are applied, while the associated displacement increases with a significant 68.97%. The post peak behaviour of the SW-75-150-Strip Analysis model shows a decreased descending gradient in comparison with that of the SW220-15 model. Thus, enhanced shear ductility is obtained when masonry walls are retrofitted with 15 mm SHCC overlay and 75 mm debonded strips.

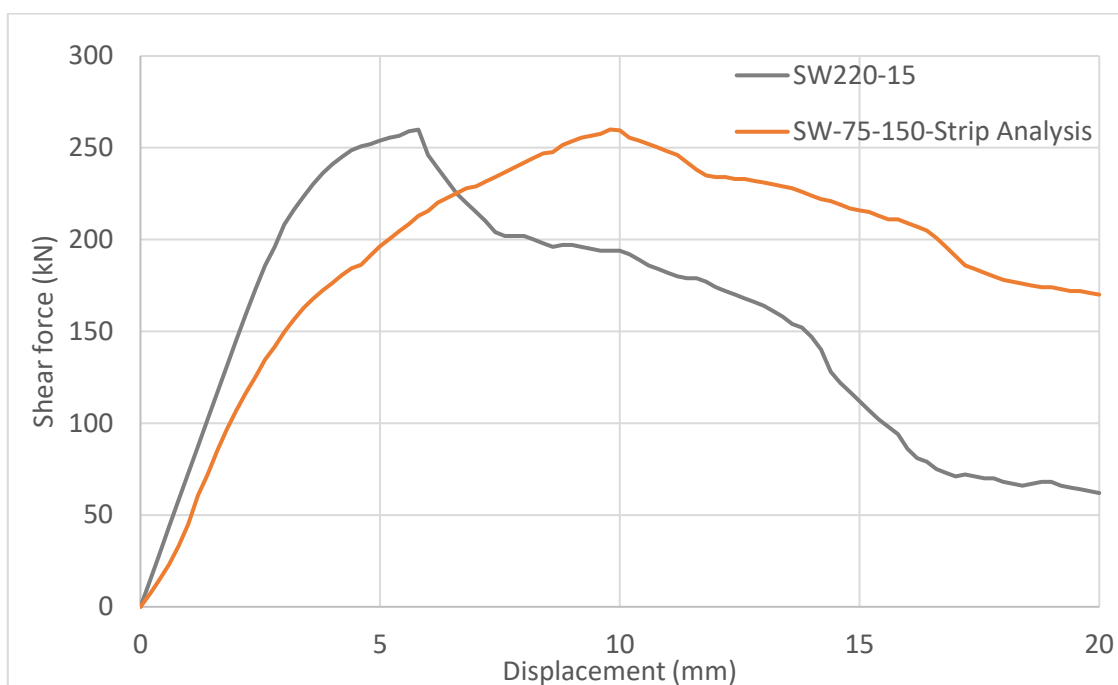


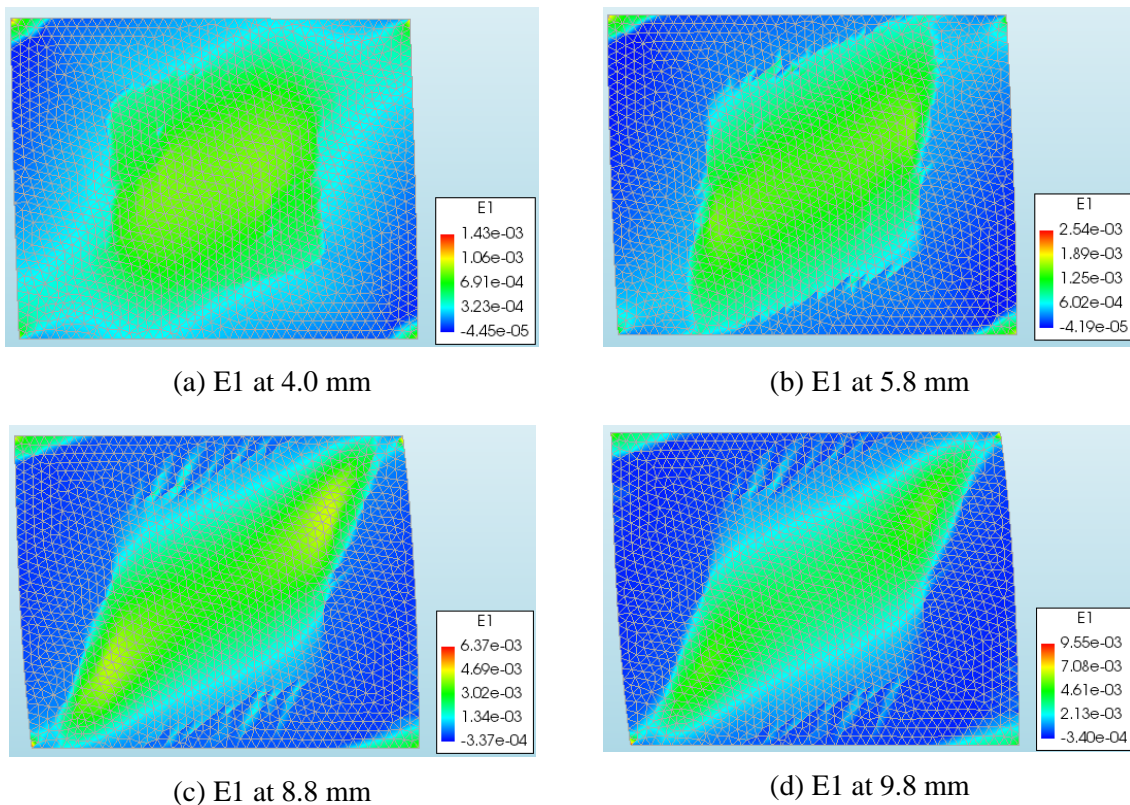
Figure 4.4: Shear force vs horizontal displacement diagram of shear walls retrofitted with 15 mm SHCC overlay with and without debonding strips.

Computational Prediction and Experimental Validation Design of Strip Debonded Overlay

The principle strain (E1) diagrams of the SW-75-150-Strip Analysis model are presented in Figure 4.5. Only the strains of the SHCC overlay are displayed. Figure 4.5 (a), (b) and (c) present the strains in the ascending hardening phase at 4.0 mm, 5.8 mm and 8.8 mm displacements respectively. The strains obtained at the maximum shear resistance of 278.46 kN with its associated 9.8 mm displacement are presented in Figure 4.5 (d). Figure 4.5 (e), (f), (g), (h) and (i) present the strains in the descending softening phase at 10.5 mm, 12.0 mm, 13.5 mm, 15.0 mm and 17.5 mm respectively. Figure 4.5 (j) presents the maximum principle strains at the ultimate displacement of 20 mm.

The principle strain contours of the SW-75-150-Strip Analysis model show an increased region of higher strain, indicating an enlarged crack distribution with the use of debonded strips. The maximum principle strains of this model are lower than those of the SW220-15 model. This indicates better distribution of strains over the larger region, and lower likelihood of localisation, or at least postponement of localisation to a larger displacement.

The principle vertical stress (S2) and vertical compressive stress (Syy) of the SW-75-150-Strip Analysis model are displayed on the left and right respectively, Figure 4.6. The stress diagrams presented from top to bottom are at horizontal displacements of 8.8 mm, 10.5 mm, 13.5 mm, 17.5 mm and 20 mm respectively. The compressive stress of 20 MPa is not breached at any of the steps, indicating no occurrence of toe crushing.



Computational Prediction and Experimental Validation Design of Strip Debonded Overlay

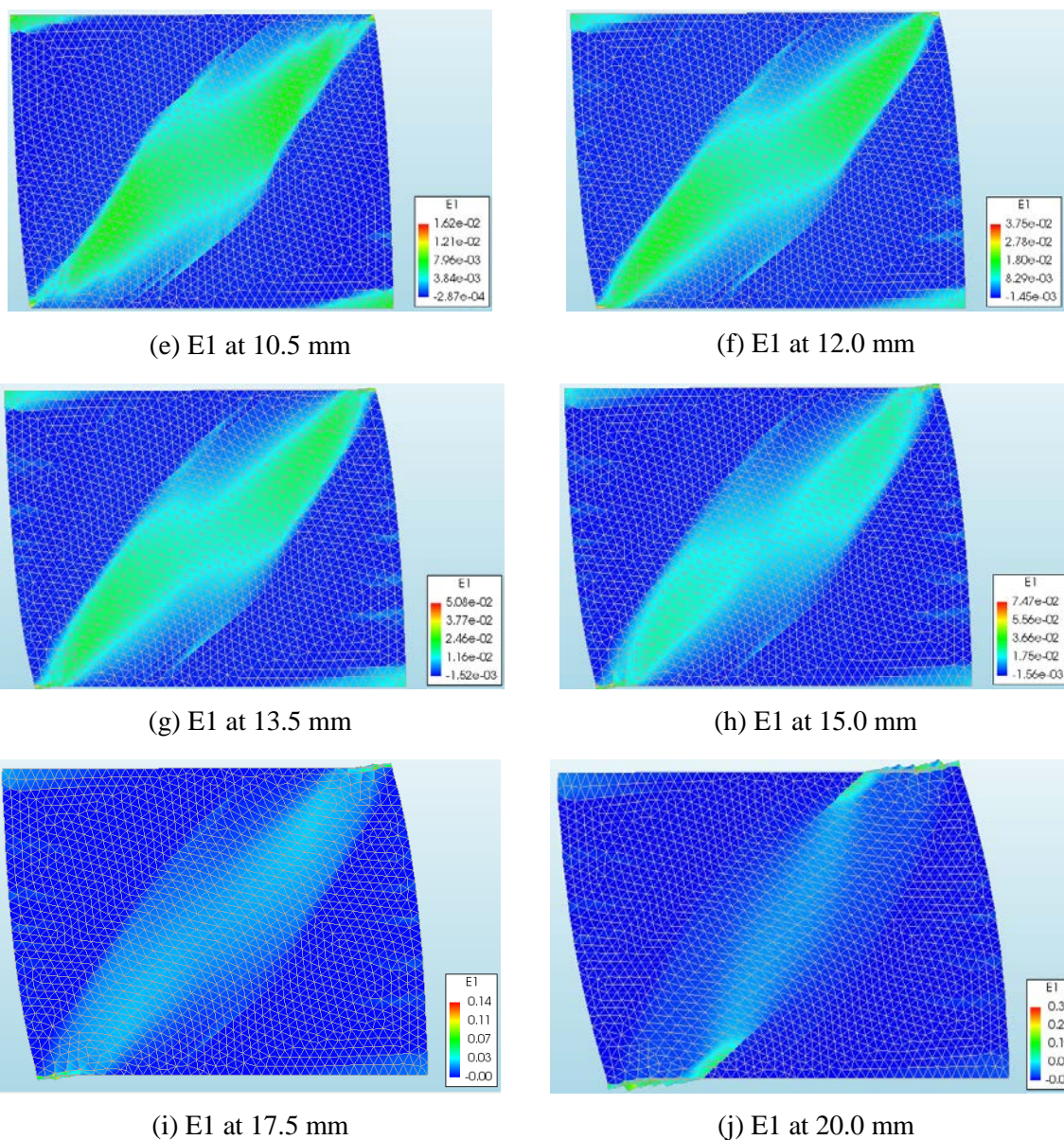
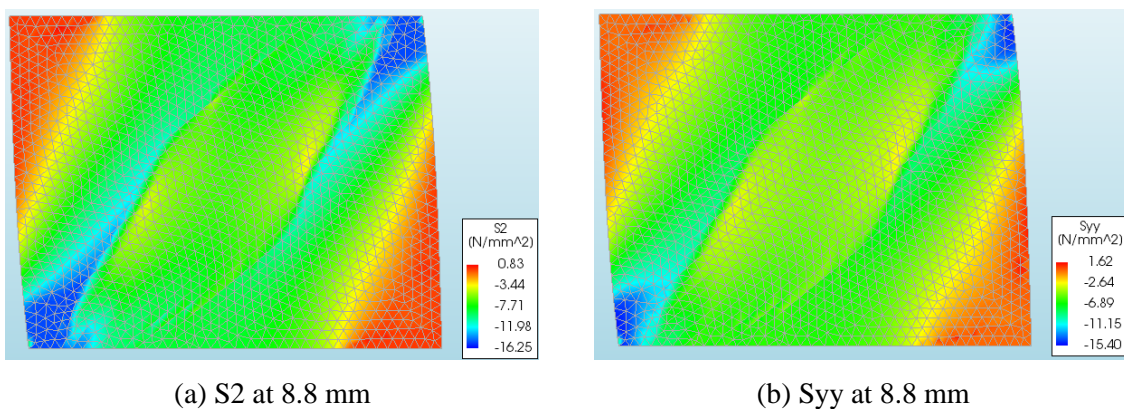
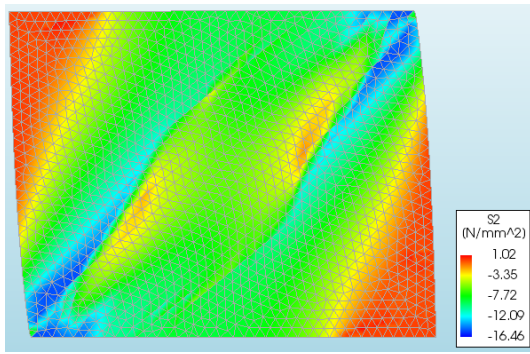


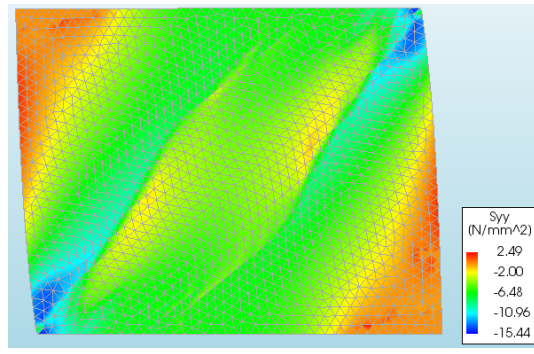
Figure 4.5: Principle strain diagrams of SW-75-150-Strip Analysis model at different horizontal displacements.



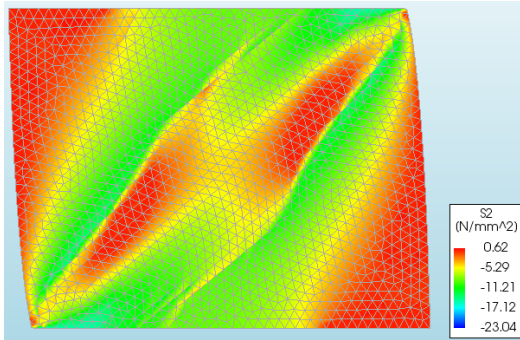
Computational Prediction and Experimental Validation Design of Strip Debonded Overlay



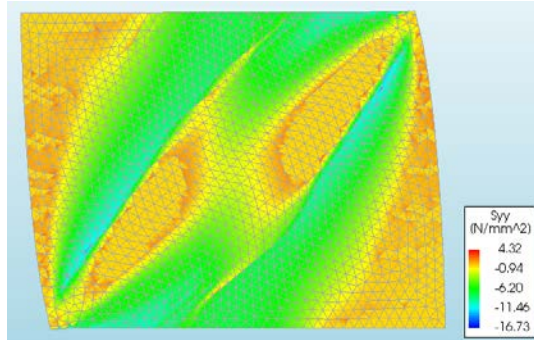
(c) S2 at 10.5 mm



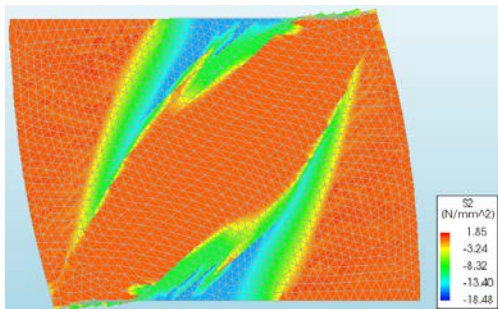
(d) Syy at 10.5 mm



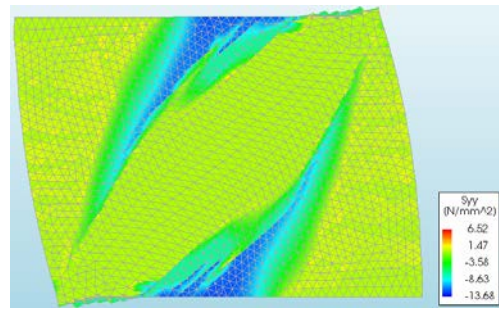
(e) S2 at 13.5 mm



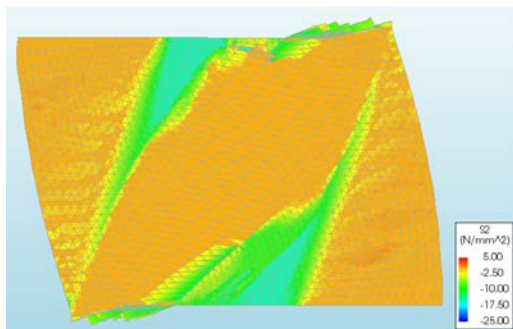
(f) Syy at 13.5 mm



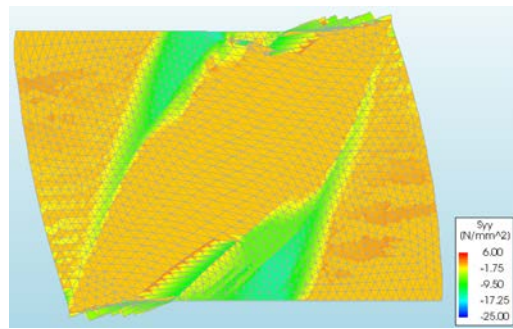
(g) S2 at 17.5 mm



(h) Syy at 17.5 mm



(i) S2 at 20.0 mm



(j) Syy at 20.0 mm

Figure 4.6: The principle vertical stress (S2) and compressive stress (Syy) of the SW-75-150-Strip Analysis model.

4.2 Experimental SHCC overlay and debonded strips spray-ability and adherence testing

The experimental test program aims to validate the computed shear strength and ductility performance of double leaf shear walls retrofitted with 15 mm SHCC overlay and debonded strips subjected to shear forces. The objective of this section is to successfully pursue the preparation and application of SHCC overlay and debonded strips on masonry shear walls for it to be easily and correctly implemented in practice.

The shotcrete equipment used for the application of the SHCC overlay is reported in this section. The mix design adopted from De Beer (2016) is applied to small-scale test walls and adjusted to obtain favourable pumpability and spray-ability, as well as low run-off. The small-scale walls are also used to obtain suitable methods of applying the debonded strips to the large-scale shear walls. Thereafter, the preparation of the large-scale shear walls is discussed.

4.2.1 Shotcrete equipment

SHCC is applied to the walls by spraying it with a shotcrete apparatus. For it to be sprayed effectively, it should have fluidity and consistency in its fresh state to limit segregation when transferred through the hose and nozzle. After the SHCC overlay is applied to the masonry walls, its viscosity should be high enough for it to stay adhered to the walls.

Figure 4.7 shows the shotcrete apparatus used for applying the SHCC overlay in this research. The machine is a Rockcrete-TSL machine manufactured in South Africa. It can achieve a maximum pumping rate of 10 l/min (used for this thesis), but the rate can be reduced by the control system. Pumping is driven by the rotor/stator, which operates to up to 50 Hz, and can pump the material up to a maximum pressure of 35 Bar. Aggregate sizes of up to 4 mm are accommodated by the machine.

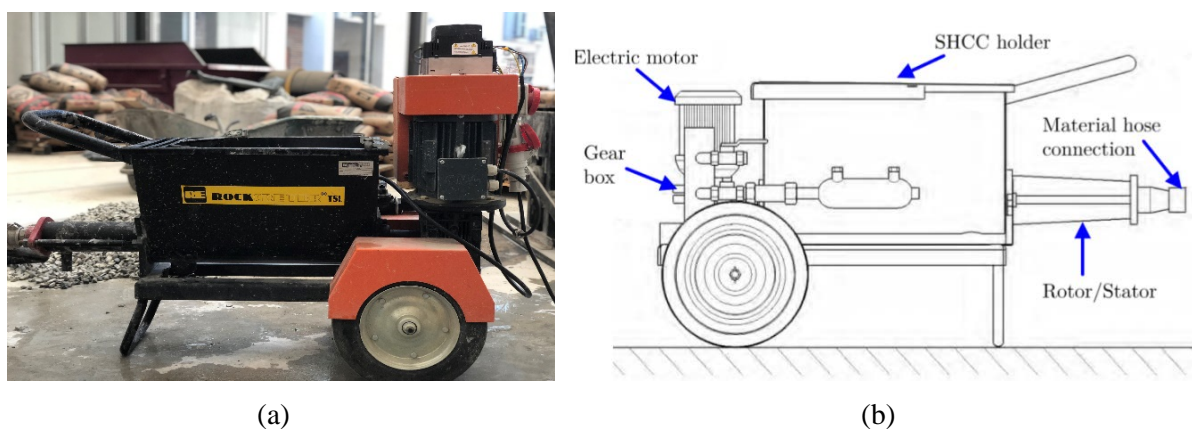


Figure 4.7: Rockcrete-TSL shotcrete equipment.

Computational Prediction and Experimental Validation Design of Strip Debonded Overlay

The nozzle displayed in Figure 4.8 is a circumferential air-pressure nozzle designed at Stellenbosch University, specifically for spraying SHCC overlays. The nozzle enables air to be supplied from behind the SHCC material, around the circumference. The flow moves through a long barrel leading to a small spraying angle, reducing wastage material. The nozzle is designed to ensure optimum air supply, and hereby obtain high spray velocity and improved compaction. This also allows the nozzle to be held further away from the wall during spraying, limiting the risk of the material being blasted off.

Applying shotcrete as a retrofitting strategy is no exact science. An experienced operator can control the nozzle with its air valve. Machines with different sizes operating at different rates will also be able to apply materials in the correct manner. The Rockcrete-TSL machine and circumferential nozzle are used for the application of the SHCC overlays further in this thesis.

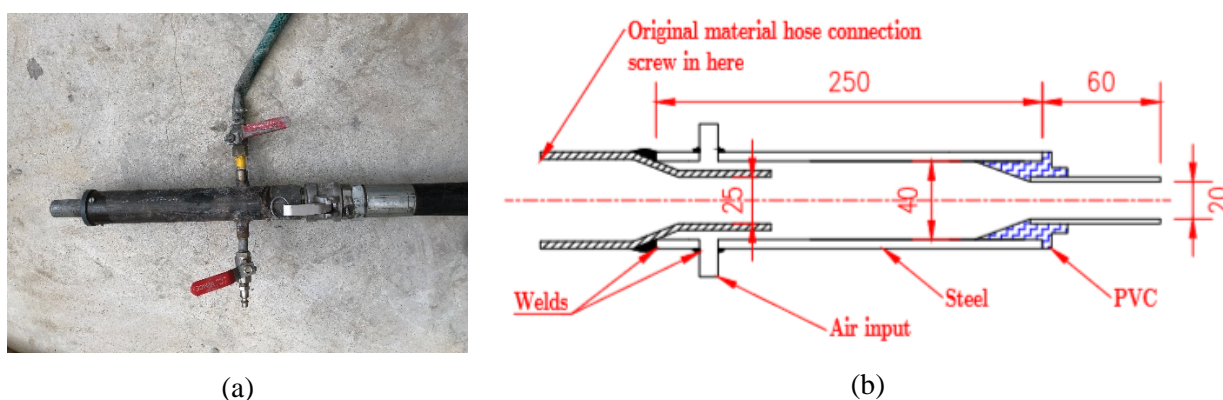


Figure 4.8: Circumferential nozzle.

4.2.2 SHCC mix design

De Beer (2016) performed deformability, spray-ability and adhesion tests on different SHCC mix proportions to obtain a favourable mix for shotcrete application. The SHCC mix design shown in Table 4.1 was developed by De Beer (2016) and used for all further tests in this thesis.

Water/binder, aggregate/binder, fly-ash (FA)/cement and calcium aluminate cement (CAC)/cement ratios of 0.34, 0.5, 1.4 and 0.05 respectively are used for the calculation of the mix proportions. CAC replace 5% of the cement to enhance the viscosity and cohesiveness of the SHCC while in its fresh state.

The cement is a CEM I 52.5N locally supplied by PPC. The type of CAC is a Segar 51®. PVA fibres with a diameter of 0.02 mm and a length of 8 mm is used. The super plasticizer used is a Dynamo SP 1 type.

Table 4.1: SHCC mix proportions adopted from De Beer (2016).

| Cement | FA | CAC | Sand | Water | Fibres* | SP | VA | Total | |
|--------|-----|-----|------|-------|---------|-----|-----|-------|----------------------|
| 420 | 620 | 21 | 540 | 365 | 2% | 2.2 | 0.8 | 1995 | (kg/m ³) |

* Fibre volume fraction

4.2.3 Deformability test

The CAC and VA are included to increase the cohesiveness and development of the viscosity over time while the mixture is still in its fresh condition. The CAC is mainly responsible for the viscosity development rate and De Beer (2016) performed deformability tests on different CAC/cement ratios. De Beer (2016) reported that by replacing 5% cement with CAC, a favourable viscosity will be obtained for mixing to spraying and finally finishing.

A deformability test is performed on the SHCC mix with proportions mentioned in Table 4.1. A small 100 mm base diameter (d_0) slump cone is used for the deformability measurement over time. No vibration is applied to the SHCC for the fresh mix to be consolidated. The SHCC collapses under gravity and spreads directly after the slump cone is lifted. The largest diameter (d_1) and the diameter perpendicular to that (d_2) are measured. Thereafter, the SHCC is subjected to vibration and the slump flow is tested according to ASTM C1437 (2007). The largest diameter of the collapsed spread (D_1) and the perpendicular diameter (D_2) are measured. Figure 4.9 (a) shows the slump flow of the mixture without vibration at $t = 0$ mins, while Figure 4.9 (b) shows the slump flow of the mixture without vibration at $t = 15$ mins.



Figure 4.9: Slump flow test (a) directly after mixing, and (b) 15 minutes after mixing.

Computational Prediction and Experimental Validation Design of Strip Debonded Overlay

The values of the deformability of the SHCC without vibration (γ) and those with vibration (Γ) are calculated as follows:

$$\gamma = \frac{(d_1 \times d_2) - d_0^2}{d_0^2} \quad (4.1)$$

$$\Gamma = \frac{(D_1 \times D_2) - D_0^2}{D_0^2} \quad (4.2)$$

Standard mixing procedures are followed. Directly after the mix is completed, the first slump measurement is taken at time equal to zero minutes. Thereafter, the slump is measured in time intervals of 15 minutes. Figure 4.10 shows the deformability results graphically. From several trials, it is observed that the workability is high enough for pumping, with Γ being larger than 1.2. However, when the value of Γ is lower than 1.2, the viscosity is too high, and the shotcrete machine is not able to pump the SHCC material.

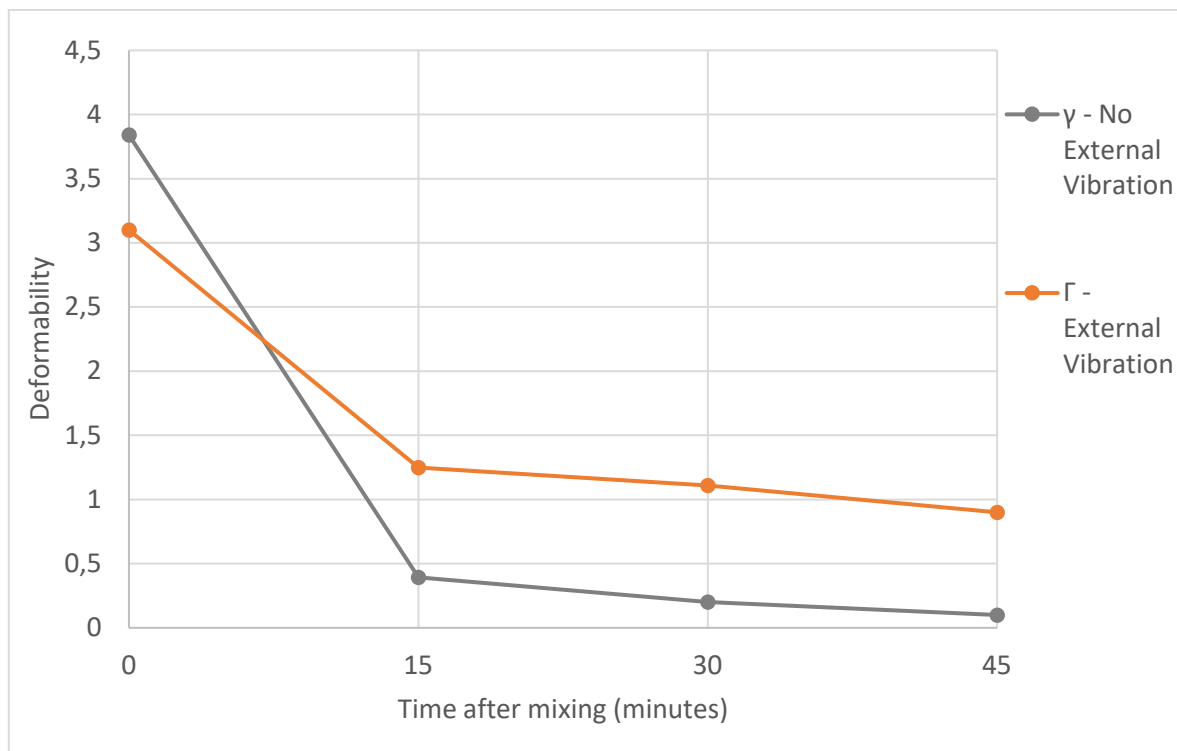


Figure 4.10: Deformability γ and Γ after time of mixing with the adopted SHCC mix.

4.2.4 Spray-ability and adhesion to small-scale masonry test walls

The experimental spray-ability and adhesion tests consist of small masonry test walls of plane dimensions 630 mm x 450 mm, shown in Figure 4.11 (a). A wooden box with a 15 mm overhanging edge is used to obtain the set overlay thickness. The walls are used to test the adhesion of the mix after it is sprayed on the masonry. Figure 4.11 (b) shows the spraying process of the SHCC overlay, where the distance from which the spraying nozzle is held from the masonry is displayed. Completion of the spraying process is seen in Figure 4.11 (c), where the overlay thickness varies roughly between 10 and 25 mm over the area before trowelling, Figure 4.12 (a). The near end of the trowelling process is displayed in Figure 4.11 (d), and trowelling is finished to an overlay thickness of 15 mm, Figure 4.12 (b).



(a) Bare specimen



(b) Spraying process



(c) Before trowelling



(d) Near completion of trowelling

Figure 4.11: Spray-ability and adhesion testing on small-scale test wall specimens.



(a) Before trowelling

(b) After trowelling

Figure 4.12: SHCC thickness before and after trowelling.

Further testing on the small-scale test walls follows for obtaining favourable bonding to masonry and surface smoothness to practically represent the debonded strips. Figure 4.13 (a) shows a buff tape that has a good bonding with the masonry bricks, but an absorbing surface on which the SHCC is most likely to bond. Figure 4.13 (b) shows a duct tape with a smooth surface suitable for the formation of the debonded strips, but with poor bonding with the masonry. The buff tape is applied to the masonry to provide a surface for the duct tape to be applied to without debonding from the masonry. Figure 4.13 shows a test wall specimen in which 130 mm buff tape with 75 mm duct tape is applied to the masonry to test if an appropriately low run-off will be obtained when the tapes are applied to the diagonal. Figure 4.13 (d) shows the buff tape with the duct tape applied to the right-hand corner with only the buff tape applied to the left-hand corner. This is done to evaluate the bonding of the SHCC overlay with the two different surfaces.

Figure 4.14 shows the results obtained on the run-off and SHCC overlay-strip bonding tests. SHCC is applied directly after mixing and shows that run-off occurs when the wall has a diagonal strip, Figure 4.14 (a). Figure 4.14 (b) shows the SHCC overlay-strips test in which no run-off occurs if the SHCC is applied seven minutes after mixing. Smooth trowelling of the diagonal strip specimen is still obtained despite the run-off. Figure 4.14 (d) and (e) show a clear weak bond between the SHCC overlay and the debonding duct tape. However, a weak bond is also obtained between the buff tape and the overlay, Figure 4.14 (f). The results obtained from the test wall specimens indicate that the buff tape should not overlap the duct tape.

Computational Prediction and Experimental Validation Design of Strip Debonded Overlay

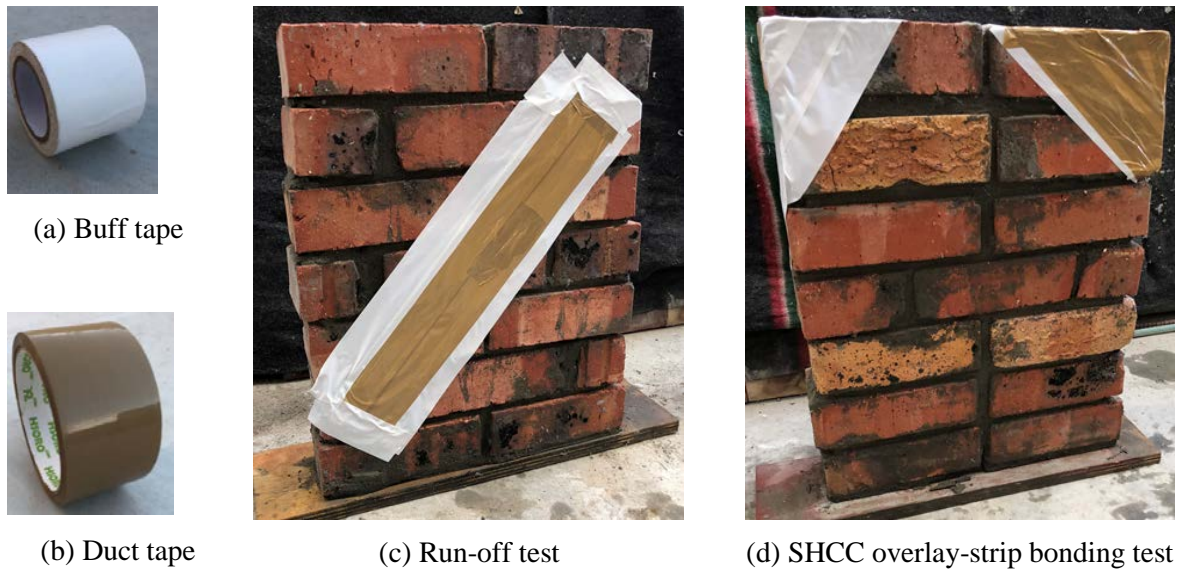


Figure 4.13: Tape bonding to masonry and surface roughness tests.

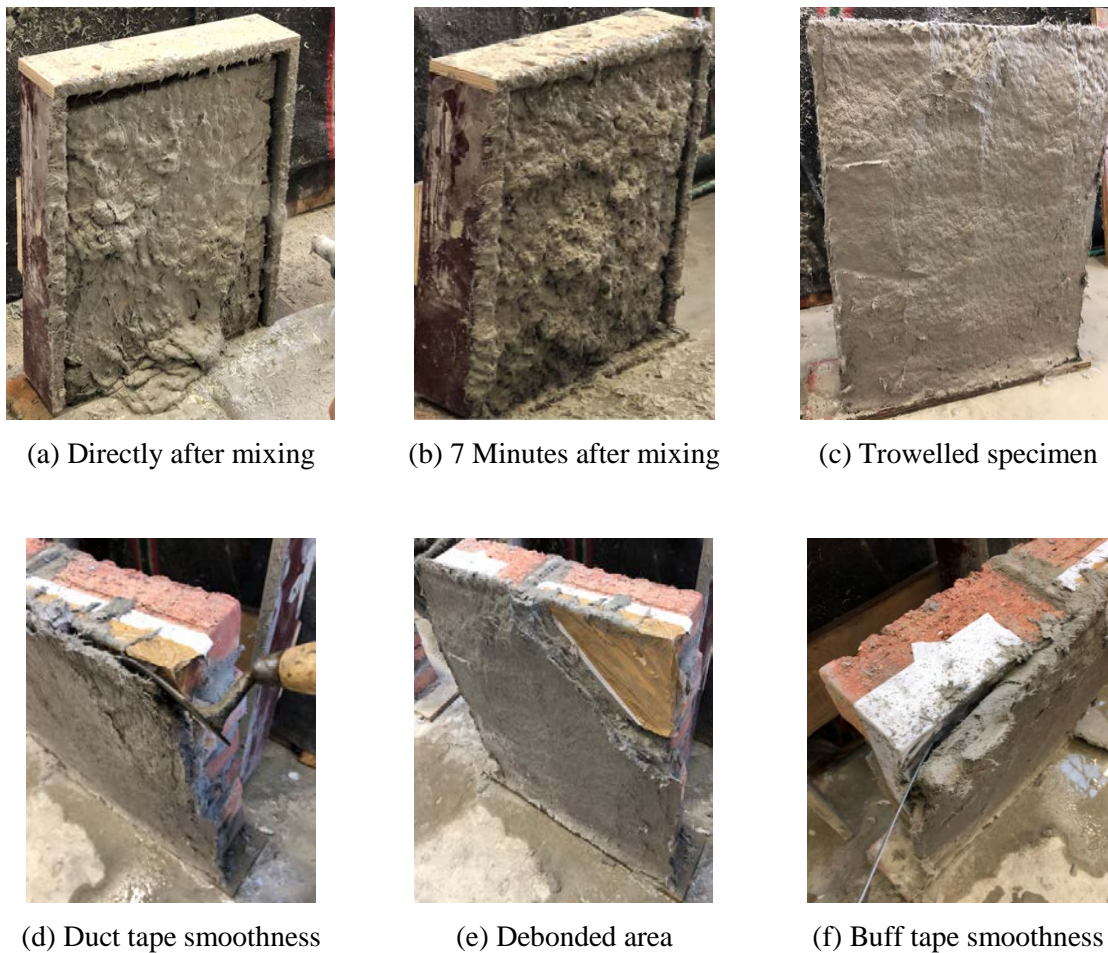


Figure 4.14: Run-off and surface roughness tests.

4.3 Masonry shear wall test setup

4.3.1 Introduction

This section discusses the procedures of the URM shear walls containing debonded strips setup. The primary aim is to investigate the shear behaviour of masonry shear walls when retrofitted with SHCC overlay and debonded strips. Note, there is no standardised test method for the confinement of the pressure or for the application of the debonded layers to the shear walls. However, it is opted to obtain a similar shear wall setup to that used by De Beer (2016).

The shear wall test consists of simulating a typically full-scale structural masonry wall element, loaded in its horizontal and vertical in-plane directions to obtain diagonal shear failure. An advantage of the shear wall test is to simulate the vertical self-weight pressure while the shear force is applied to the top surface of the wall, similar to a shear wall element in URM structures. The disadvantages of the experimental testing are that the wall specimens are heavy, and the manufacturing thereof is time consuming.

For shear wall testing of this research, the SHCC overlay thickness is kept constant while the variables are the debonded strip width and centre to centre spacing.

4.3.2 Mortar and masonry brick compressive tests

A mortar mix with class I specification from SANS 10164-1 (1989) is used for the wall specimens. The mortar mix is adopted from De Beer (2016) and is provided in Table 4.2. The mix contains a water/cement ratio of 0.75 and the same sand and cement as the SHCC mixture discussed in Section 4.2.2.

The same mortar mix displayed in Table 4.2 is used for constructing all the experimental test specimens in this thesis. The compressive strength of the mortar is determined by standard compressive testing (ASTM C109, 2010), with at least two specimens prepared from every mix. A 250 kN Zwick MTM is used to perform the compressive tests. Cubes with 50 mm dimensions are crushed at a rate of 60 kN/min.

Table 4.2: Mortar mix proportions.

| Water | Cement | Sand |
|-------|--------|------|
| 1 | 1.32 | 6 |

Burned clay bricks are used throughout the research for all specimens. The dimensions of the clay bricks are $222\pm 3 \times 105\pm 3 \times 70\pm 3$ mm. The bricks have a smooth face and a grooved face, Figure 4.15. The grooves are 5 mm deep and 12 mm wide. The smooth face is the facing side on which the SHCC overlay is applied with the grooved face being the non-facing side. This type of clay brick is typically used in multi-story URM building in the Western Cape region. SANS 10249 (2012) specifies that water should be applied to the bricks 24 hours before the specimens are constructed, to ensure that the absorption rate is initially lower than $1.8 \text{ kg/m}^2\cdot\text{min}$. Eight bricks are used for the determination of the compressive strength. The BS EN 772-1 (2011) specifications are followed for determining the compressive strength of the bricks. A 2 MN Instron MTM is used to crush the bricks at a loading rate of 300 kN/min.



Figure 4.15: Burned clay bricks.

4.3.3 Experimental shear wall specimen

The URM shear walls are built with the masonry bricks and mortar as discussed in the section above. The walls are built onto a RC beam base, with a similar RC beam attached to the top, 15 days thereafter. Figure 4.16 shows the specimen dimensions of $1150\pm 4 \times 935\pm 4 \times 220\pm 4$ mm, with 11 bricks in height and 5 bricks in length. The dimensions are similar to the double leaf masonry specimens tested by De Beer (2016) and are selected to represent typical wall sections between window openings of URM walls. An aspect ratio (l/h) of 1.2 is selected to obtain the favourable shear failure rather than the overturning force.

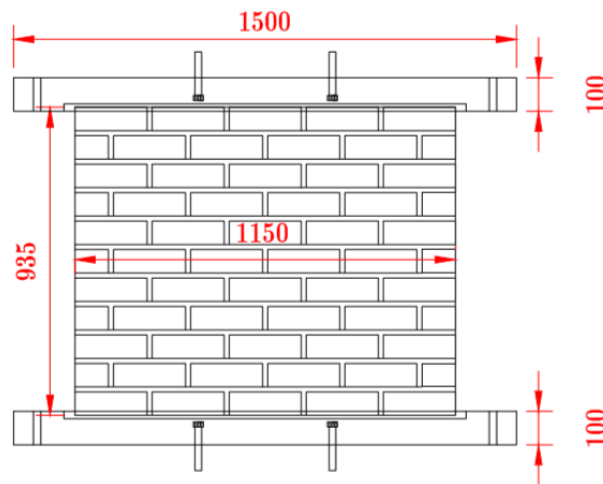


Figure 4.16: Shear wall specimen dimensions.

The dimensions of the RC beams with its reinforcement (shown in green) are displayed in Figure 4.17. All the reinforcement rods have a 12 mm diameter and a characteristic tensile yield capacity of $f_y = 450$ MPa (Y12 rods). Class 8.8 bolts with high characteristic yield strength of $f_y = 800$ MPa and 70×70 mm steel plates with a 5 mm thickness (blue) are in the beams to connect them to the top and bottom steel beams. High strength self-compacting concrete (SCC) is used to produce the beams.

The beams are cast in wooden moulds made of shutterply wood and the surface painted for it to be reused, Figure 4.18 (b). Screws with 8×40 mm dimensions at 120 mm spacing are used to assemble the moulds. A central groove with dimensions of $22 \times 240 \times 1200$ mm is created in the mould in which the shear wall is constructed. Desirable compaction is obtained by the SCC, and little surface finishing is necessary. Note that the RC beams manufactured and used by De Beer (2016) are re-used in this thesis.

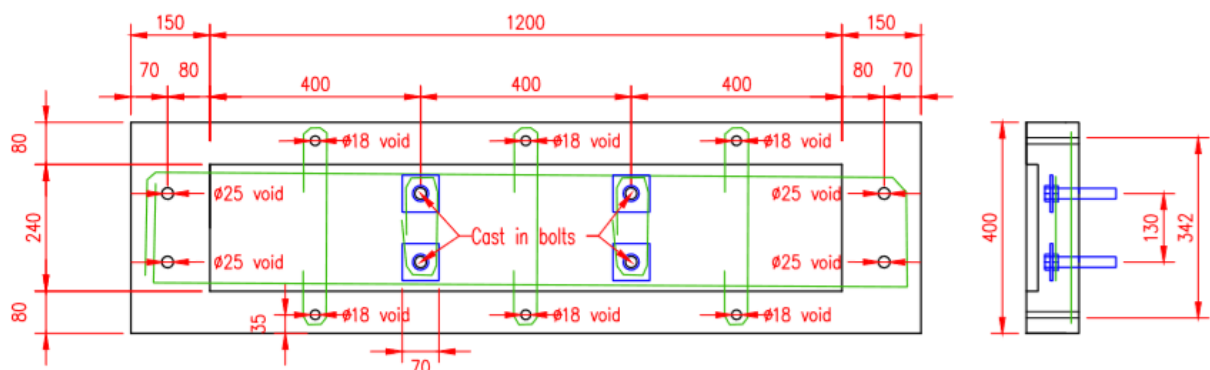
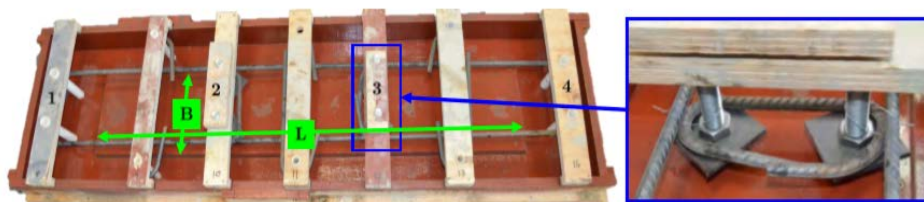


Figure 4.17: Concrete beam dimensions (De Beer, 2016).



(a) Wooden mould



(b) Beam casted with SCC

Figure 4.18: RC beams casting mould and procedure (De Beer, 2016).

A skilled bricklayer built 5 masonry walls within one day, each onto a separate RC foundation beam. The top RC beams are placed on the walls 15 days after the walls are built, Figure 4.19 (a) and kept in laboratory conditions (see Appendix B, Figure B.1 for storage of the shear walls). A mortar with a lower water/cement ratio (0.4) than that used to build the masonry walls is used to attach the concrete beams to the walls to ensure full contact between the RC beams and the masonry, for appropriate load transfer between the beams and masonry, and preferred failure through the masonry joints rather than shear-slip along the beam-masonry interfaces.

After the top RC beams are attached to the walls, the debonded strips are applied. Figure 4.19 (b) shows the insulation tape applied to the walls as markers for the debonded tape to be applied to obtain the favourable dimensions. Here, the 75 mm wide strips with 150 mm centre to centre spacing are displayed. Thereafter, the buff tape and duct tape, discussed in Section 4.2.3, are applied to the walls, Figure 4.19 (c) and (d).

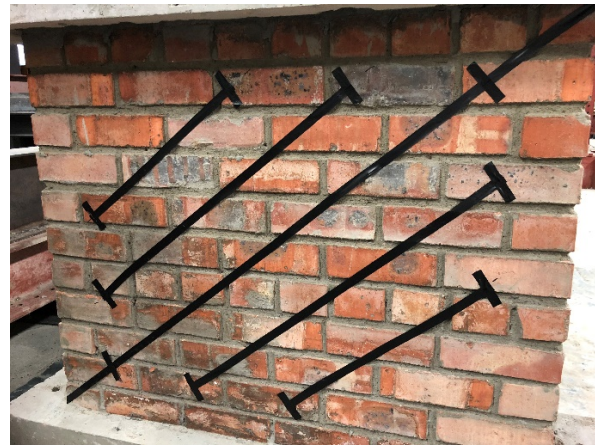
A wooden frame is applied to obtain the desired 15 mm SHCC overlay thickness on the shear walls. Figure 4.20 (a) shows a shear wall specimen during the SHCC overlay application process. Thereafter the overlay is trowelled smooth with the wooden frame to obtain the 15 mm thickness, Figure 4.20 (b).

After the overlay is applied to all the specimens, the SHCC overlay is wetted and cured for 7 days with a sprinkler after which it is left to harden. The shear wall specimens are kept indoors in laboratory conditions during the process.

Computational Prediction and Experimental Validation Design of Strip Debonded Overlay



(a) Bare SW



(b) Insolation tape



(c) Buff tape



(d) Duct tape

Figure 4.19: Masonry walls with debonding strips.



(a) During SHCC application



(b) After trowelling

Figure 4.20: Retrofitting shear walls with SHCC overlay.

4.3.4 Testing machine

An Instron MTM with an actuator of 500 kN ultimate load capacity is used to apply a shear force to the shear wall specimens. An adjustable meccano structural steel element set is used to construct the loading frame for the Instron actuator. Careful planning of the loading rig is important to obtain a similar test setup to that of De Beer (2016) and to make use of steel parts available in the laboratory. The laboratory has a 500 mm thick concrete floor with bolt holes on a 920 mm grid spacing. The setup is adjusted for the spreader beams to be fixed by bolts in these holes to fix the shear wall structure at its base. The testing actuator and loading rig setup with a wall specimen are shown in Figure 4.21. In the figure various details are indicated to clearly show careful details of the vertical support (blue rectangle, (i)) and the lateral supports (blue rectangles, (d) and (h)) supporting the load spreader beam. Bearing details are shown separately in Figure 4.22 (a) and (b), and Figure 4.23.

The setup is designed to ensure that no structural parts will undergo significant deformation, and not fail when the Instron actuator applies its ultimate 500 kN load capacity. The frame setup dimensions are shown in Figure 4.24.

Lateral supports are included in the frame setup to limit the shear wall setup out-of-plane movement and the occurrence of failure. Lateral movement at the Instron actuator connection will damage the actuator, necessitating careful design of a hinged connection that ensures axial load on the actuator only. This includes in-plane lateral displacement at the actuator connection, as well as out-of-plane displacement. The Instron head and loading beam are restrained vertically by a roller support, and the wall lateral (out-of-plane) support is designed to prevent out-of-plane translation or action on the actuator, and of course any possibility of catastrophic out-of-plane collapse. A 5 mm clear gap is left between the vertical restraint and the loading beam, to allow limited free translation vertically, but providing lateral support under accidental failure.

When placing the shear wall specimen with an overhead crane in the test setup, the bolt holes of the RC base beam are aligned with those in the frame lower steel beam on the laboratory floor slab. Thereafter, the load spreader beam with the coil springs attached to it, is aligned with the top RC beam and lowered by the crane, and bolted to the beam. Four bolts are used to attach the loading beam to the top RC beam to ensure that the shear force is distributed evenly along the RC beam. The loading beam is connected to the Instron actuator with four bolts (Figure 4.25, (a)). The steel beam on the base of the concrete floor is bolt connected to the floor with the two bottom spreader beams, running perpendicular with the wall in-plane direction.

Two beams, each bolted to the laboratory floor, are placed parallel to the founding beam to allow connection of the 6 wall tie rods. The rods are stressed to produce a pre-tension force to the structure, representing the self-weight of the upper stories. The rod pair of row 1 pass through load cells at the bottom, while load cells are connected to the top of the rods in rows 2 and 3, providing for continuous

Computational Prediction and Experimental Validation Design of Strip Debonded Overlay

monitoring of the rod forces. Each rod is fixed by a nut and washer at each end. A 200 kN load cell is used to measure the vertical pre-tension pressure applied by each rod. A channel section steel beam supported by the beams parallel to the ground beam on each side is used as support for the load cells.

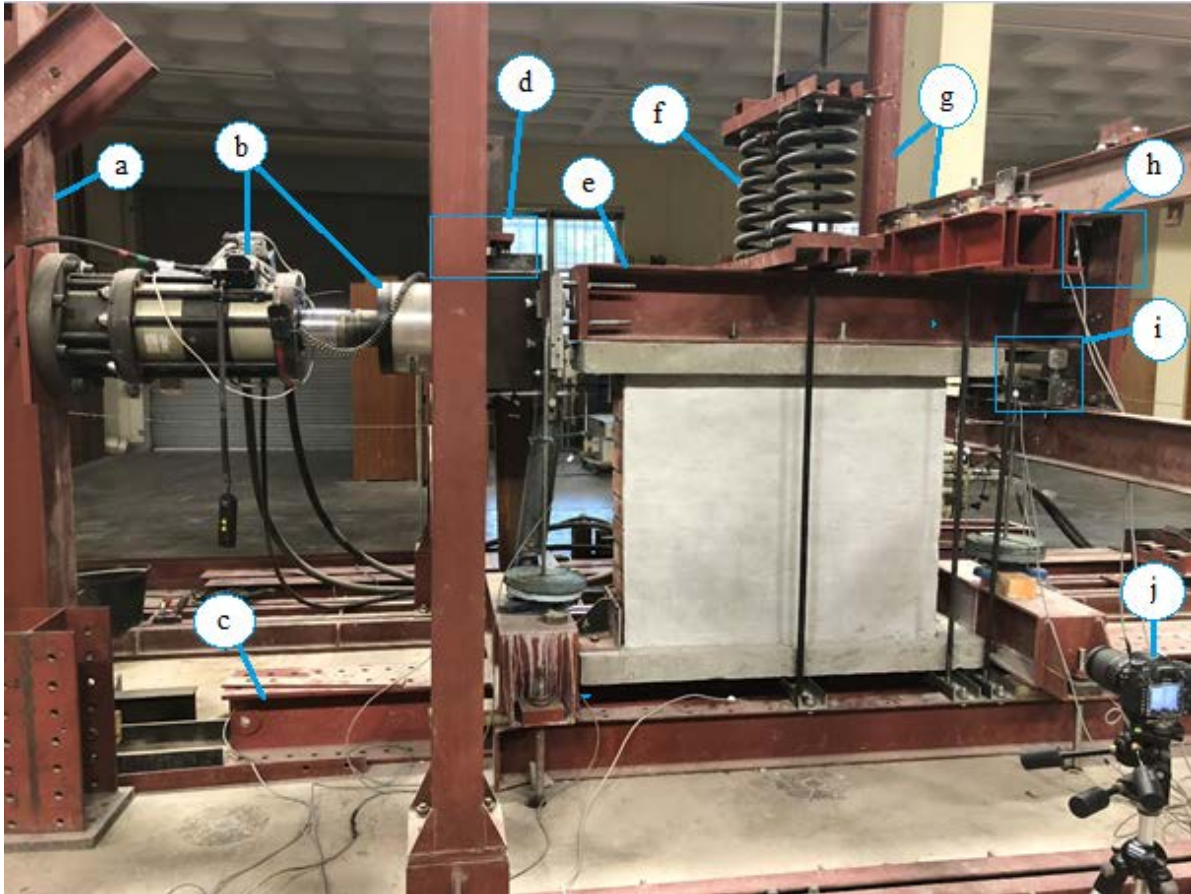


Figure 4.21: Testing machine setup with a SW specimen in place; (a) Instron supporting frame; (b) Instron actuator; (c) Base steel beam; (d) Instron head lateral roller support; (e) Load spreader beam; (f) Coil springs; (g) Lateral roller supporting frame structure; (h) Spreader beam connected to a lateral support; (i) Vertical roller support; (j) Camera.

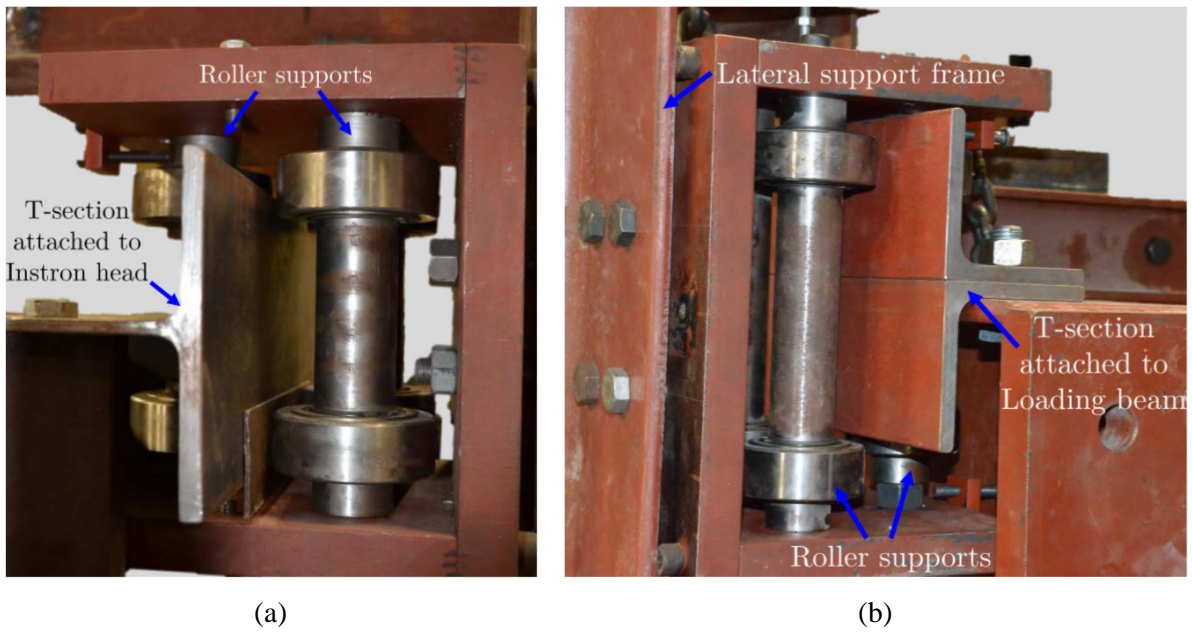


Figure 4.22: Lateral roller supports at (a) Instron head and (b) spreader beam.



Figure 4.23: Vertical roller support

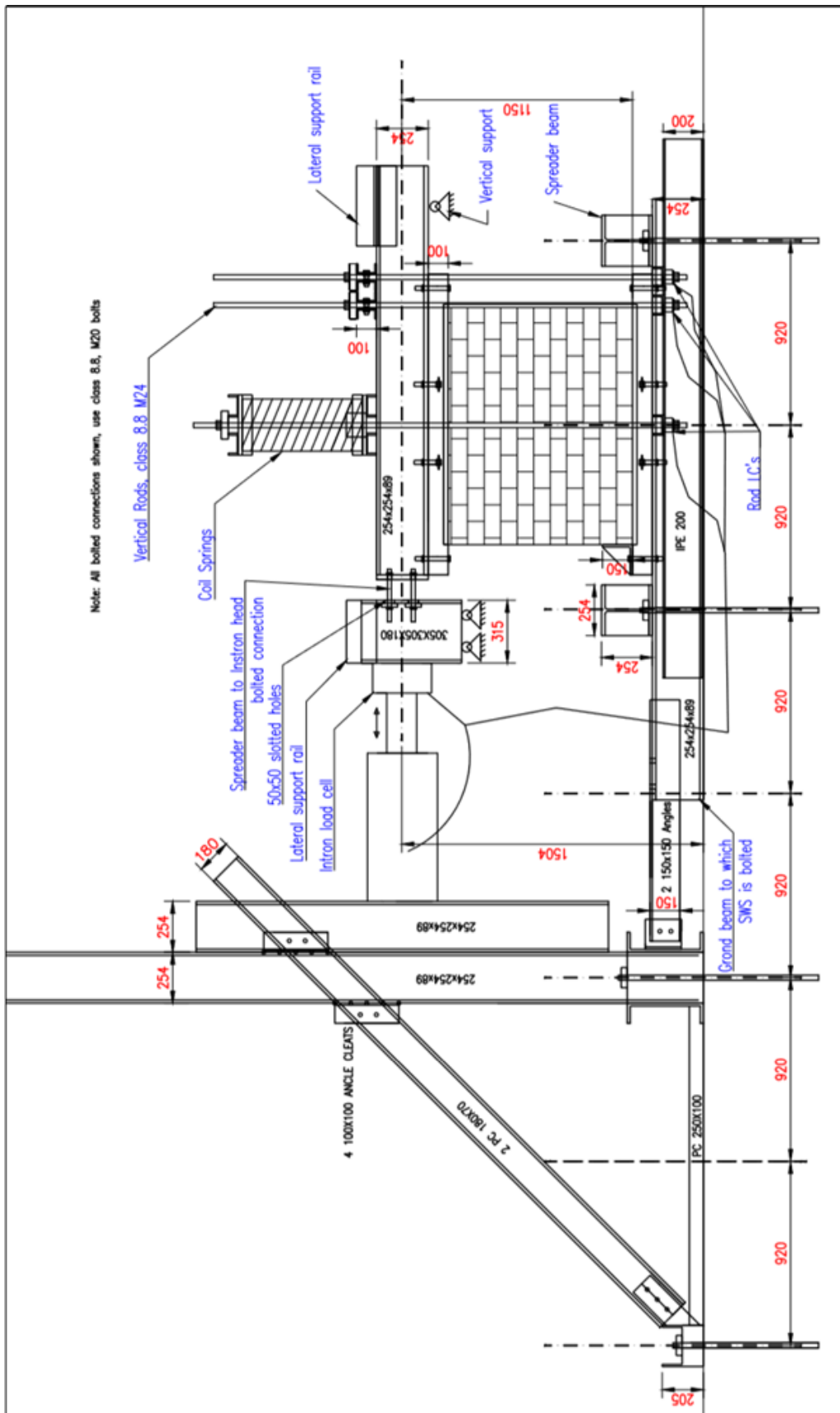


Figure 4.24: Testing setup layout.

Computational Prediction and Experimental Validation Design of Strip Debonded Overlay

Careful consideration is given to displacement measurement at various positions on the wall, to capture relevant displacements and deformation of the wall. The blue rectangles drawn in Figure 4.25 show the positioning of the LVDT's used on the shear walls. Clamps and frames are used to keep the LVDTs in position to allow displacement measurements to be taken relative to fixed positions on the laboratory floor.

An HBM WA/100 mm LVDT (100 mm measurement length) is positioned to measure the top horizontal displacement on a Perspex plate attached to the centre of the top row of bricks on the left-hand side. On the right-hand side, an HBM WA/50 mm LVDT (50 mm measurement length) is placed on a Perspex plate attached to the top row of bricks, also to measure the horizontal displacement. An average measurement between the two is used as the top horizontal displacement.

HBM WA/50 mm LVDTs are placed vertically on each side of the shear wall, and provision made for their moving ends to remain vertical by placing them on a Perspex surface, 75 mm from the edge of the bottom of the top RC beam, Figure 4.26 (a). The Perspex surface is smooth, enabling wall movement perpendicular to the LVDT, while only vertical displacement of the top corners is measured.

An HBM WA/10 mm LVDT (10 mm measurement length) is positioned horizontally at the edge of the bottom RC beam, Figure 4.25. It is used to measure the slippage between the RC beam and the floor beam, to obtain the horizontal displacement of the top beam relative to that of the bottom beam. No LVDT is placed on the bottom row of bricks as no sliding shear between the bricks and the bottom beam is expected, assuming that the RC beam and corner bricks undergo equal displacement.

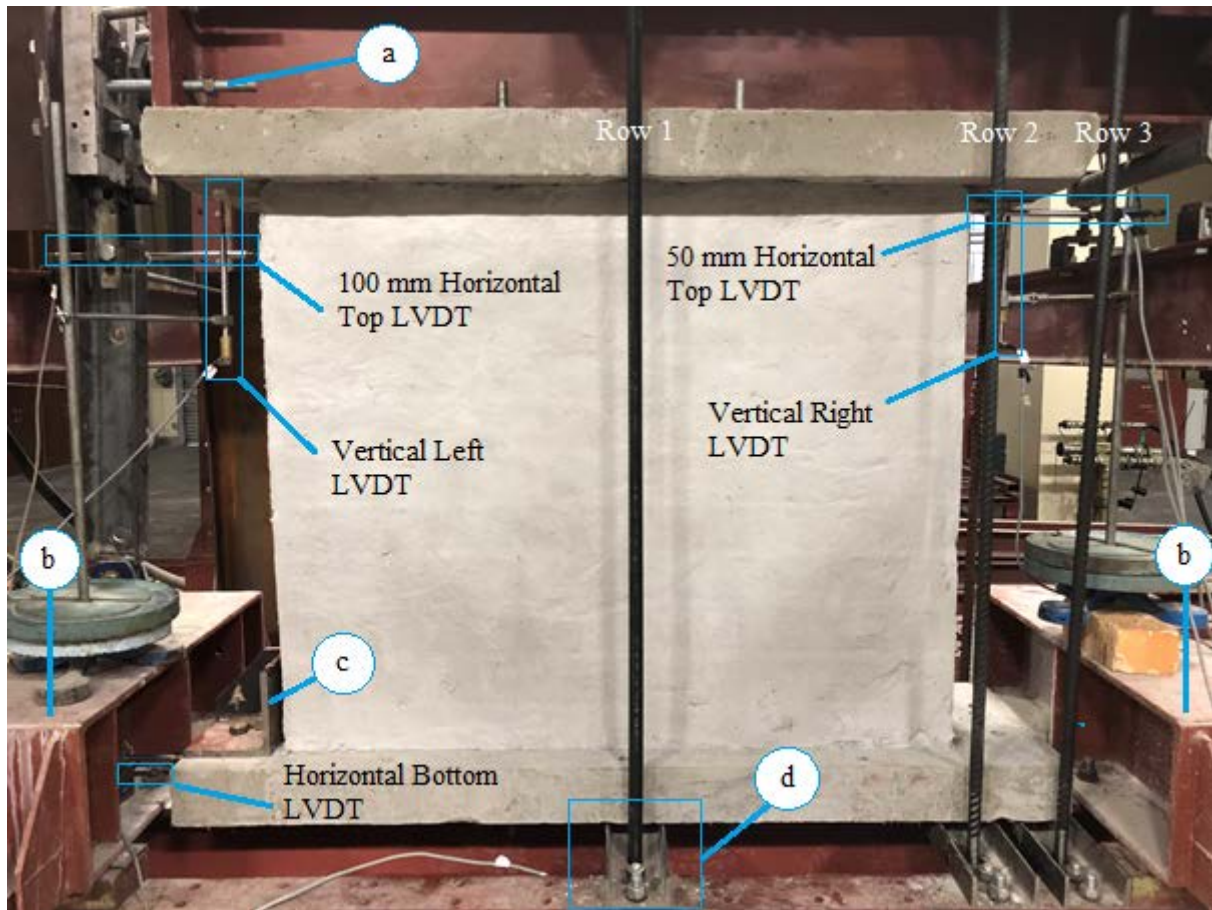
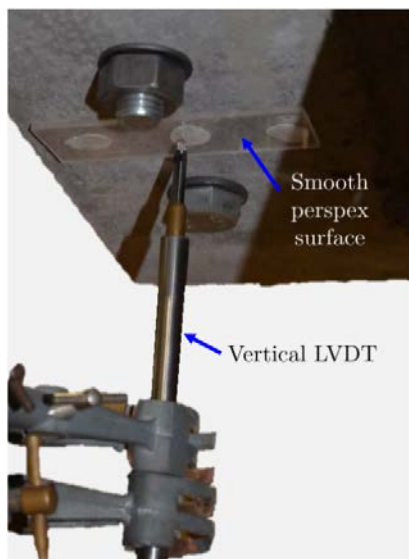
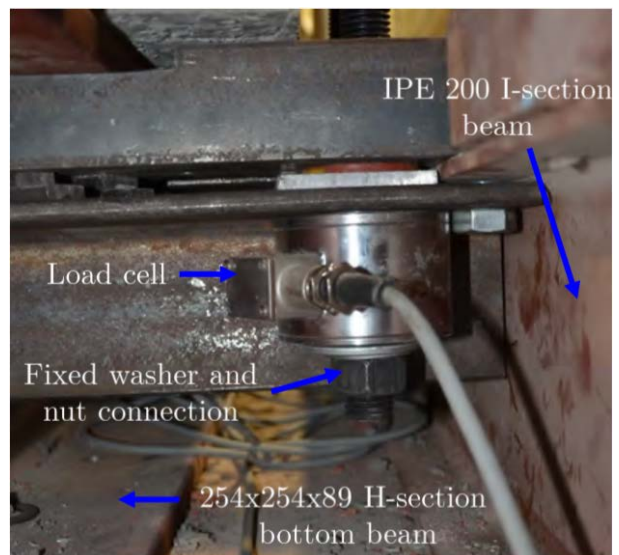


Figure 4.25: SWS in the testing rig in place and the LVDT's indicated with blue boxes; (a) Instron head/spreader beam bolt connection; (b) Bottom spreader beam connecting the base beam to the concrete floor with colts; (c) Foot stop angle section; (d) Connection of vertical rods to parallel base beams.



(a)



(b)

Figure 4.26: Close up of (a) 50 mm Vertical LVDT sliding on a smooth Perspex surface; (b) Load cell taking prestress measurement at bottom of vertical rods.

4.3.5 Constraints and loading regimes

The shear wall specimen in the testing rig is subjected to complex boundary conditions and loading states, in an attempt to simulate a wall part in an URM building subjected to vertical compressive and horizontal shear forces. A tension, pull-over force is applied to the top spreader beam by the Instron actuator to simulate in-plane shear force. The spreader beam is connected to the top concrete beam by four bolts, which are connected to the masonry wall with a strong mortar, to allow the shear force to distribute evenly in the specimen.

Post-tensioning rods are connected to the top spreader beam and to the parallel beam at the base to apply a superimposed gravity load simulation to the specimen. Coil springs are connected to the central post-tensioning rods to limit additional tension force from arising in the rods due to tip-over/rotational movement of the wall, or flexural crack opening. Two rows of additional post-tensioning rod pairs are used in a fixed configuration, in which tip-over moment forces will increase the normal forces in the rods, to limit rocking. This is done to ensure diagonal shear failure, but to an extent simulate restraint by stiff upper structural parts on the shear wall in actual buildings. Rocking, or flexural failure will occur, leading to horizontal cracks at the bottom and/or top concrete beam, if these additional pre-tensioning rods are not included. The rods are positioned in such a manner that their resultant force and lever arm equal that of the shear force applied at the height of 1150 mm.

No standardised shear wall tests yet exist, thus no standard specifications are set out for the control of the pre-tensioning forces to ensure favourable, or representative shear failure. A vertical pressure of 0.35 MPa, simulating upper stories of an URM structure, is selected for the tests in this research. The Instron actuator applies the shear force via its head at a displacement-controlled rate of 2 mm/min.

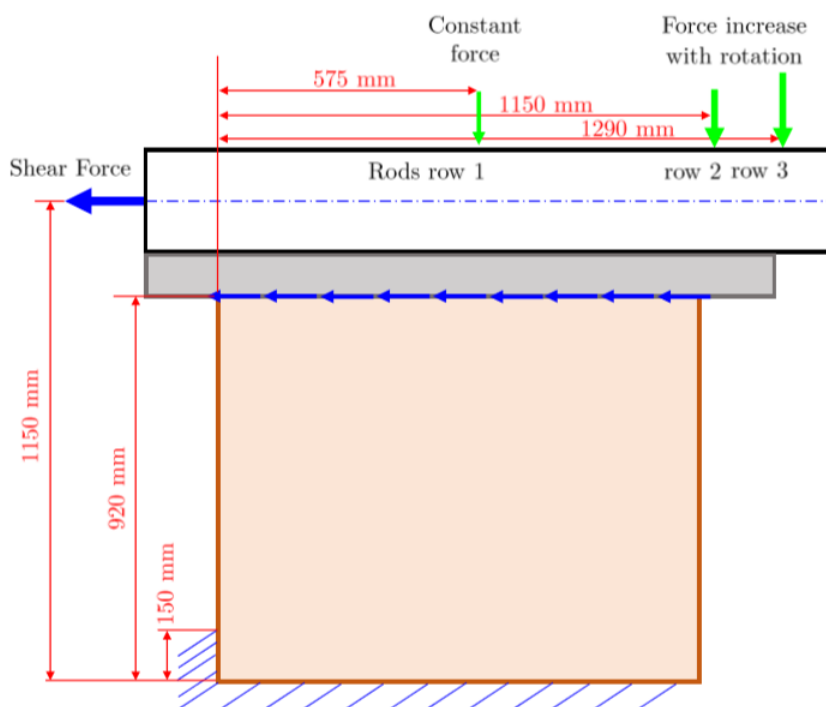


Figure 4.27: Shear wall specimen free body diagram.

4.3.6 Collecting data

A Spider 8 data collector and computer system are used to collect the data from the load cells and LVDTs connected to the SW test specimens. The displacement and force of the Instron actuator is linked to the system for synchronized measurement. The system collects measurements from the LVDT's and LC's at a rate of 5 Hz. Cracks are captured at 20 photographs/min with a 16 mega pixel high resolution camera.

4.4 Conclusions and recommendations

Detailed nonlinear computational modelling has been presented of a new method containing debonded strip interfaces, extrapolating the calibrated model from the previous chapter. The computed results of the model containing double leaf masonry, 15 mm SHCC overlay and 75 mm debonded strip widths have been compared to that of the model without the strip interfaces (SW220-15) and the following conclusions are drawn:

- The debonded diagonal strip interfaces are successfully modelled with the use of an interface material model with low normal and tangential stiffness to simulate a smooth surface.

Computational Prediction and Experimental Validation Design of Strip Debonded Overlay

- The model, containing five 75 mm width strips with 150 mm centre to centre spacing, computes a similar ultimate shear strength compared to the fully bonded SW220-15 model.
- The computed post-peak response of the strip debonded overlay model has a less steep descending branch compared to that of the SW220-15 model, indicating increased ductility and higher energy dissipation.
- A larger diagonal region of high algebraic maximum principle strain (E_1) is observed in the strip debonded overlay model, indicating that more cracks are likely to form over this enlarged region than in the case of the fully bonded overlay.

Five masonry walls have been built in the structures laboratory and debonded strips and SHCC overlay are prepared and applied to these walls. The wall and masonry thickness are kept constant, with a variation in the debonded strip widths and spacings. A testing rig setup is constructed in which the shear behaviour of these shear wall specimens is tested. The shear behaviour of the SWS is presented in the following chapter, with validation of the computed increase in ductility being the primary aim.

Chapter 5

Results and Discussion

5.1 Introduction

The results of the experimental shear wall test setup described in Chapter 4 are presented here. This chapter includes the compressive strength of the mortar used to build the shear walls and to attach the RC beams to the top of the SW, followed by the strength and ductility enhancement results obtained by applying SHCC overlays and debonded strips to these walls. The experimental results are compared to the computed computational results discussed in Chapter 3 and 4, and also to the results obtained by De Beer (2016). Note, no drying shrinkage cracks are observed on the SHCC overlays at the time of testing, thus no further discussions thereof will follow in this section.

5.2 Compressive strength

The compressive strength of the masonry mortar and the mortar used to attach the RC beams to the masonry walls is tested on 50 mm cubes as described in Section 4.3.2. Table 5.1 summarises the mean results (f_{cm}) of the compressive tests with the associated coefficient of variation (CoV). The RC beams (RCB) and shear walls (SW) are tested at an age of 28 days. Compressive tests are performed to compare strengths and inconsistency between the different batches.

From Table 5.1 it can be seen that the mortar used for the two different purposes can be classified as class I, as the mean strengths are higher than 14.5 MPa (SANS 10164-1, 1989). The CoV of all the specimens are between 7-11%, indicating that sufficient consistency is obtained. The lower mean compressive strength obtained for the SW is possibly due to the different mixing procedure used by the brick layer. Additional water was added to obtain a favourable workability. The lower compressive strength will not have a significant influence on the shear strength results of the SW, thus it is sufficient.

Table 5.1: Compressive strength of mortar specimens.

| Specimen | no of samples | f_{cm} (MPa) | CoV (%) |
|----------|---------------|----------------|---------|
| RCB | 10 | 28.40 | 7.2 |
| SW | 14 | 16.33 | 10.3 |

Compressive strength tests are performed on the bricks (f_{bu}) used in all tests in this research according to Section 4.3.2. Five bricks are selected randomly for testing, resulting in a mean f_{bu} of 41.4 MPa with a CoV of 9.3%. The bricks are sufficient for being used in URM structures according to SANS 10164-1 (1989) specifications.

5.3 Shear wall results

The specifications and conditions described in Section 4.3 are used to analyse the behaviour of URM shear walls when retrofitted with SHCC overlay. The loading and boundary conditions ensure a realistic representation of a typical URM structure. The objective of this section is to test the in-plane strength and ductility behaviour of shear walls retrofitted with SHCC overlay and debonded strips, and to compare the results with the computed computational results and the experimental results obtained by De Beer (2016).

Note, all SWS discussed in this section are double leaf masonry walls (220 mm thick) retrofitted with 15 mm SHCC overlay. A control specimen without any strips (SW-220-15-No Strips) is tested as a reference case to the results obtained by De Beer (2016) and discussed. Thereafter, four specimens containing debonded strips are tested according to Section 4.3. Two of the four specimens contain strips with a width of 75 mm and a centre to centre spacing of 150 mm (SW-75-150-01 and SW-75-150-02) and two with 100 mm width strips and 200 mm centre to enter spacing (SW-100-200-01 and SW-100-200-02). The shear force vs horizontal displacement results are presented, followed by the crack formation of each specimen.

5.3.1 Boundary conditions results and interpretation

The specifications discussed in Section 4.3 are used to perform in-plane pull-over tests on shear walls. In this section, the vertical boundary conditions are investigated, and the tie rod force evolution presented.

Before the start of the test, the centre row (Row 1) of rods is connected to coil springs and pre-tensioned to the force discussed in Section 4.3 (14 kN each side), while the two rows of rods on the right flank (Rows 2 & 3) of the specimen are pre-tensioned by tightening the rods to a force of 9 kN each. Positioning of the rods can be seen in Figure 4.27. The coil springs and central positioning of the rods in Row 1 cause the force in the rods to remain constant during the test, while the force in the rods on the right flank increase during the test, as seen in Figure 5.1 (a). The row of rods on the far right (Row 3) shows the highest force increase, with the middle row (Row 1) showing a constant force during the test. The measurements of the vertical LVDT's on the right and left-hand side are shown in Figure 5.1 (b). Note, movement towards the LVDT records a positive reading as seen from the vertical left LVDT (downwards) while movement away from the LVDT records a negative reading as seen from the vertical

right LVDT (upwards). A cracked wall specimen is rotated 180° and tested from the opposite side to obtain these data. The reason for the large horizontal displacements is due to the initial crack closing at the starting phase of the test. Figure B.2 (Appendix B) shows the cracked specimen after testing by which the initial and final diagonal cracks are visible.

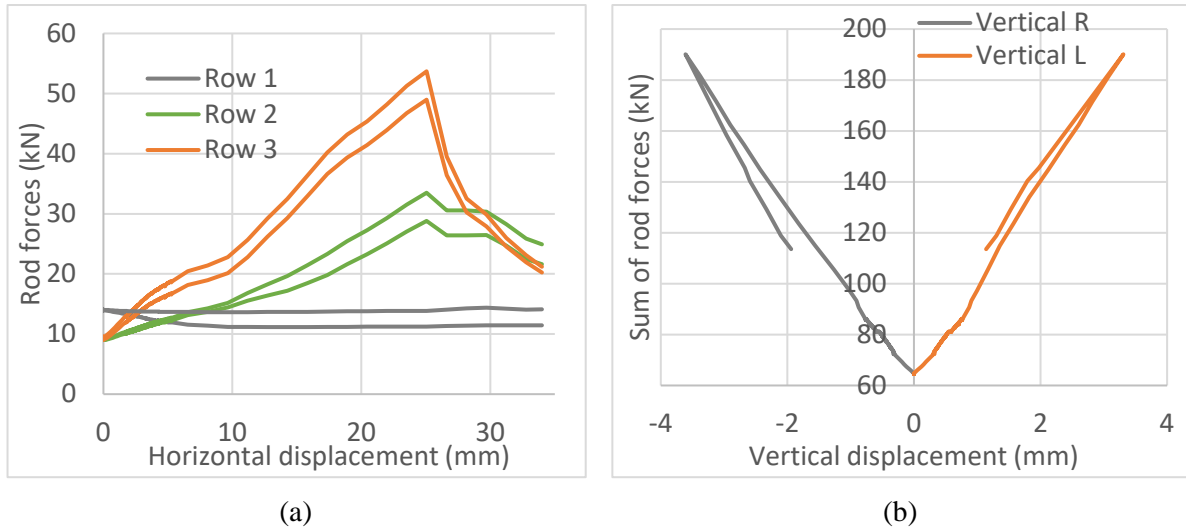


Figure 5.1: (a) Rod forces vs horizontal displacement; (b) Sum of rod forces vs vertical displacement.

The sum of all the vertical forces and the shear force vs horizontal displacement are shown in Figure 5.2 (a). Note that the total vertical force is the sum of the forces exerted by the six rods and the weight of the top concrete beam. The shear force shows a higher initial increase than the vertical force until localised crack formation, after which the shear and vertical force increase at a similar rate. Figure 5.2 (b) presents the shear force/vertical force relation at which a one to one ratio is obtained after localised crack formation.

The similar rate of increase of the shear and vertical force in the post peak phase is ascribed to friction along to the mortar brick interfaces along the crack path. The drop in the vertical force is due to the reverse rotation of the wall on the right-hand side of the crack after it forms.

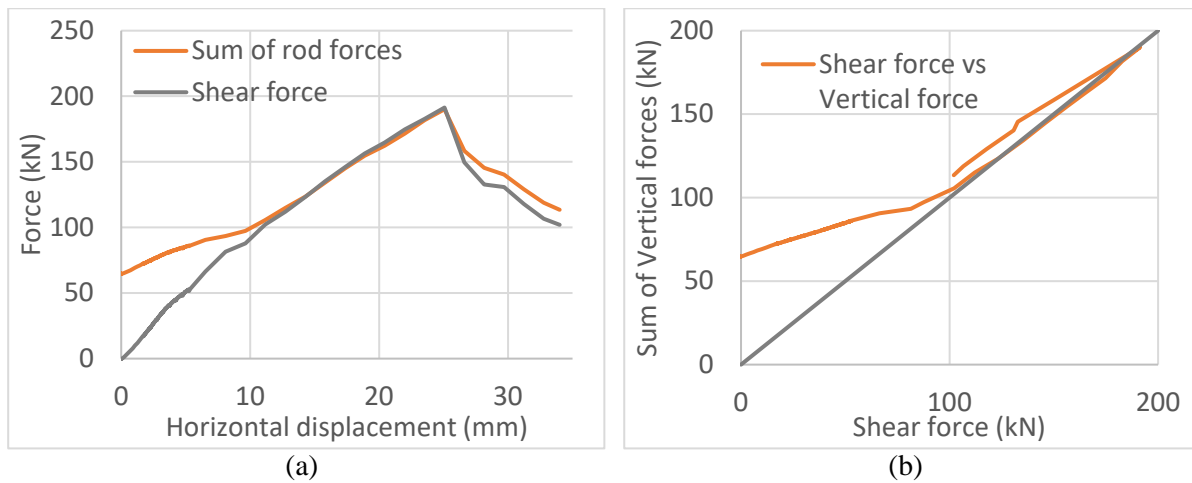


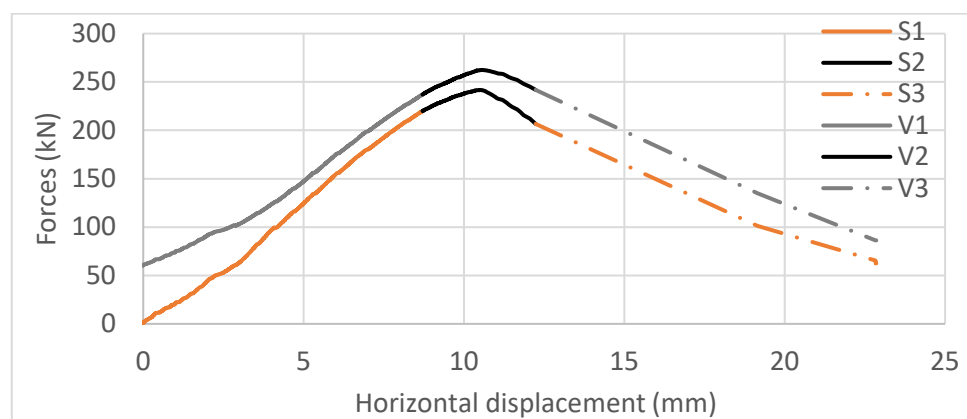
Figure 5.2: (a) Sum of rod forces and shear force vs horizontal displacement; (b) Vertical vs shear force.

The following sections present the results for each shear wall specimen, the total vertical and shear force are plotted against the top horizontal displacement. The curves presented in the shear and vertical force vs horizontal displacement graphs for all specimens contain three parts each. The first part of the shear and vertical force is indicated by S1 and V1 respectively. This part indicates the force and displacement until initial cracks in the SHCC overlay are visible. The parts indicated by S2 and V2 are the shear and vertical force during multiple cracking in the SHCC overlay. These parts end when a localised crack forms in the SHCC, or in some cases where delamination occurs. S3 and V3 indicate the shear and vertical force after localised cracking or delamination of the overlay until the test stops.

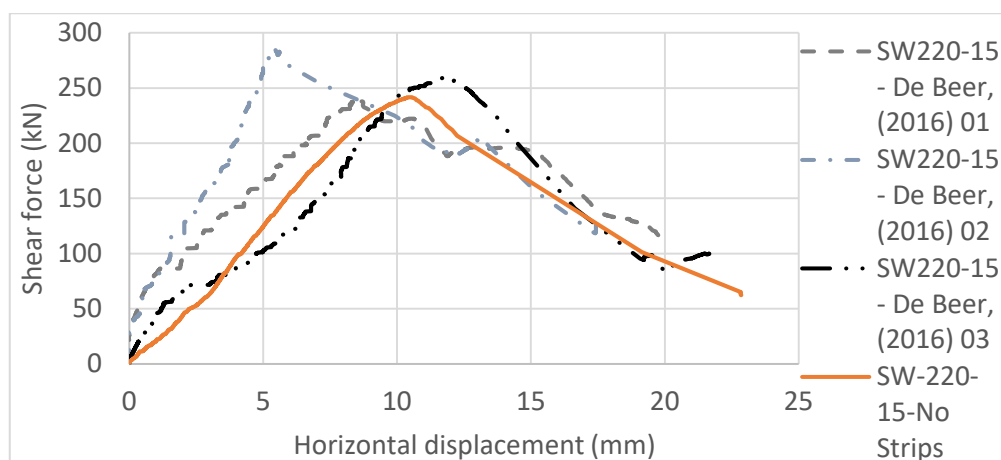
SW-220-15-No Strips

The SW-220-15-No Strips specimen is a reference case for comparison with the results obtained by De Beer (2016). It is tested to validate that the correct procedures are followed in the preparation and setup of the materials used, SWS, and testing rig. The shear and vertical forces are plotted against the top horizontal displacement, Figure 5.3 (a). Multiple fine diagonal cracks start to form in the SHCC at a shear force of 229.84 kN and a displacement of 9.34 mm. An ultimate shear force of 241.74 kN is reached at a displacement of 10.51 mm. Thereafter, a localised crack starts to form at the centre of the diagonal and moved towards the corners. Full development of the crack is reached at 12.23 mm displacement and can be seen in Figure 5.5, with the crack pattern in the masonry shown in Figure 5.4.

Figure 5.3 (b) shows the shear force results vs horizontal displacement results of the SW-220-15-No Strips specimen compared to the three experimental results (dashed lines) obtained by De Beer (2016). The primary ascending branch shows a lower slope, after which the second ascending branch shows a reasonably similar stiffness. The reference specimen reaches reasonable agreement of the ultimate shear resistance and post-peak responses. Given the reasonable agreement, the test walls and procedures are considered to be representative of those of De Beer (2016).



(a)



(b)

Figure 5.3: (a) Shear and vertical force vs horizontal displacement of SW-220-15-No Strips specimen and (b) compared to the results obtained by De Beer, (2016).

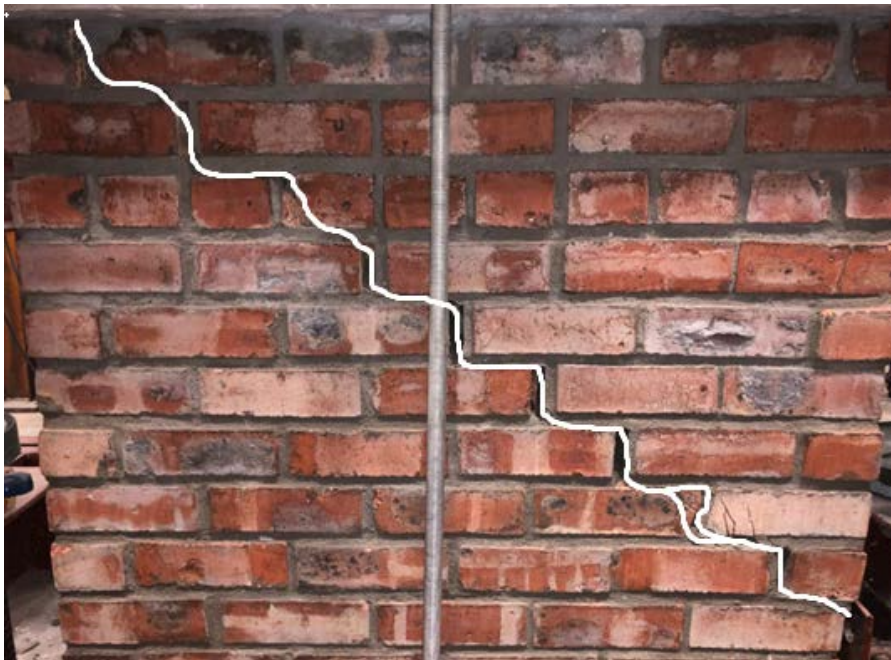


Figure 5.4: SW-220-15-No Strips crack pattern in the masonry.

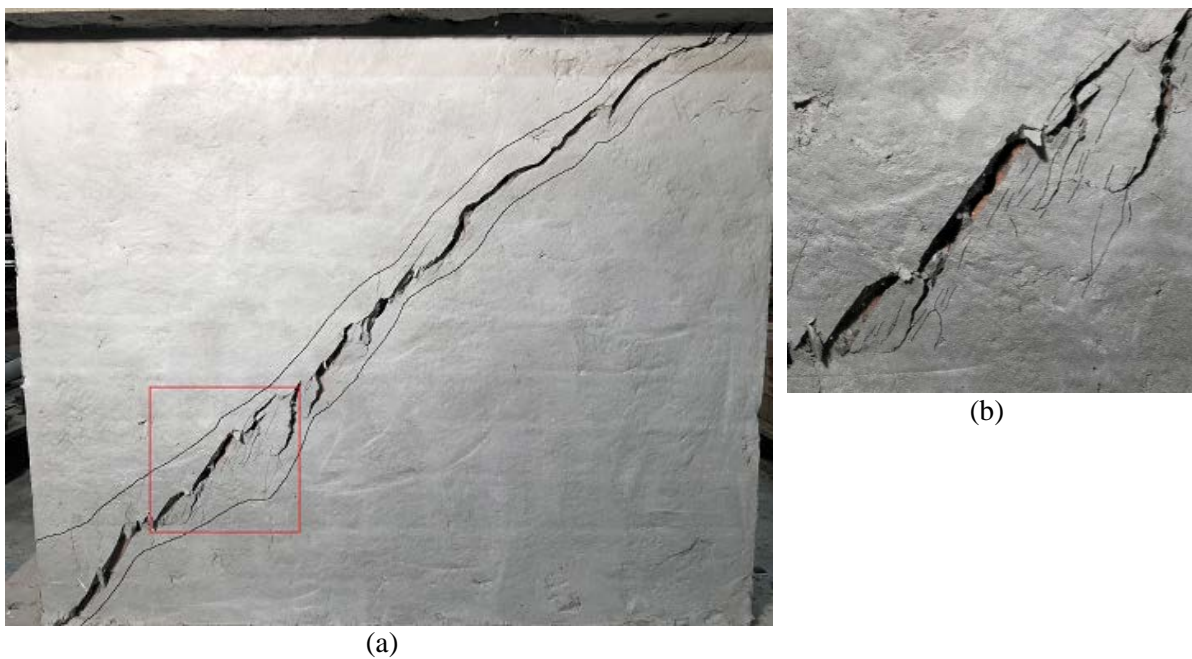


Figure 5.5; SW-220-15-No Strips (a) localised crack with crack pattern/width outlined; (b) enlarged photograph.

SW-75-150-01

The shear and vertical forces vs the top horizontal displacement of the SW-75-150-01 specimen are shown in Figure 5.6. Multiple fine diagonal cracks start to form on the diagonal at a shear force of 204 kN and a displacement of 10.08 mm. An ultimate shear force of 218.92 kN is reached at a displacement of 13.31 mm. A fully developed localised crack forms at a shear force of 177 kN and an associated displacement of 16.79 mm.

Initial multiple crack formation starts and distributes on the central diagonal strip. Hereafter, cracks in the SHCC overlay move into the first strip below the central strip and an enlarged area of fine multiple cracks start to form in the debonded strip region. Figure 5.8 shows the crack formation in the SHCC from which the enlarged crack distribution area can be seen. The nonlinear analysis showed for the SW-75-150-Strip Analysis model that large strains initiate on the diagonal, after which large strains arise in the first strips above and below the central strip as the pull-over displacement increases, Figure 4.5. Thus, a crack pattern with reasonable agreement between the analysis and SW-70-150-01 specimen is obtained.

The primary ascending branch shows a higher stiffness to that of the SW-220-15-No Strips specimen, but reasonably similar to the results obtained by De Beer (2016), with a less steep slope in the second ascending branch. Lower ultimate shear resistance is obtained, but the maximum resistance is at a higher horizontal displacement. The descending branch shows a less steep response compared to the results obtained by De Beer (2016) and the SW-220-15-No strips specimen. The favourable less steep descending branch suggests that the increased number of cracks forming in the debonded surfaces increase the ductility of the specimen's response.

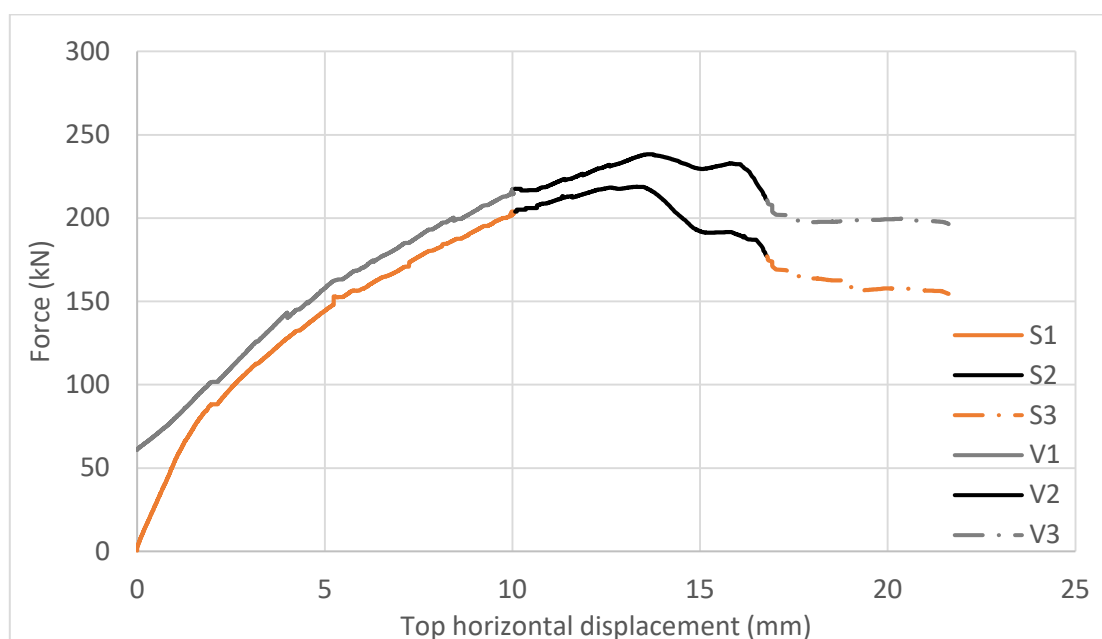


Figure 5.6: Shear and vertical force vs horizontal displacement of SW-75-150-01 specimen.

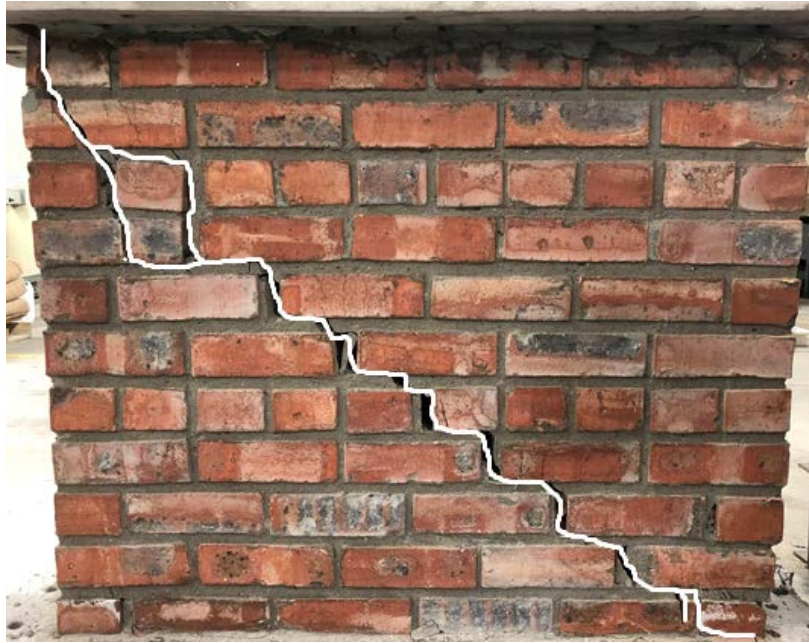
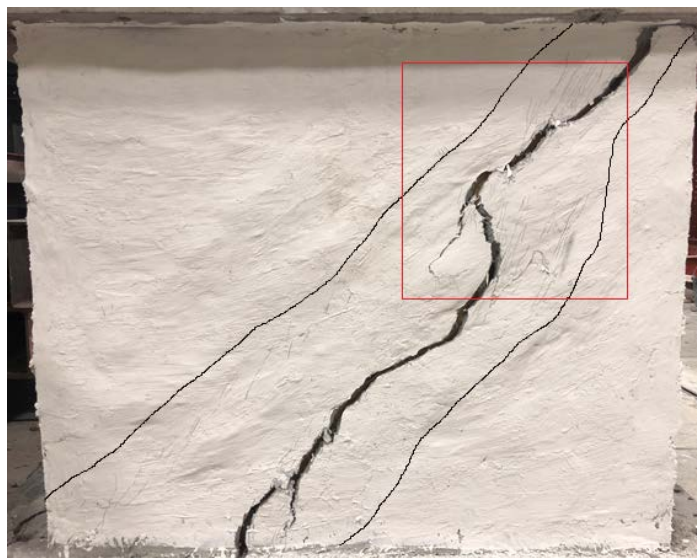
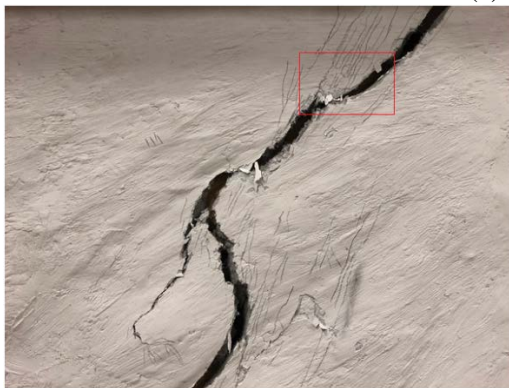


Figure 5.7: SW-75-150-01 crack pattern in the masonry.



(a)



(b)



(c)

Figure 5.8: SW-75-150-01 (a) localised crack with crack pattern outlined; (b) enlarged photograph; (c) enlarged photograph focussing on crack distribution.

SW-75-150-02

The shear and vertical forces vs the top horizontal displacement of the SW-75-150-02 specimen are shown in Figure 5.9. Multiple fine diagonal cracks start to form on the first and second strip above the central strip at a shear force of 218.2 kN and a displacement of 10.29 mm. An ultimate shear force of 243.76 kN is reached at a displacement of 11.94 mm.

The white line in Figure 5.10 shows the path of the initial crack in the masonry wall. The SHCC forms multiple cracks in the two top strips, enabling it to reach the high ultimate shear force. The overlay maintains high forces for 5 mm of pull-over displacement as the crack (shown in white) starts to open. Before a fully localised crack develops, a new crack path forms within the masonry wall (blue line in Figure 5.10) at a displacement of 16.93 mm. Hereafter, the SHCC forms a fine crack on the central diagonal strip after which it delaminates from the masonry at the bottom right-hand corner. The steep descending slope observed in Figure 5.9 after 17.52 mm is due to delamination. Crack patterns can be seen in Figure 5.11. Note, the black lines indicate the region in which the SHCC cracked during the initial crack in the masonry, while the blue lines show the region in which it cracked on the central strip during the second crack in the masonry.

The primary ascending branch shows a steeper stiffness to that of the SW-220-15-No Strips specimen, but with a reasonably similar second ascending branch. A slightly higher ultimate shear resistance is obtained at a higher horizontal deformation. The descending branch is less steep compared to the results obtained by De Beer (2016) and the SW-220-15-No Strips specimen. The favourable less steep downwards branch indicates that the higher number of cracks forming on the debonded surface increase the specimen's ductility.

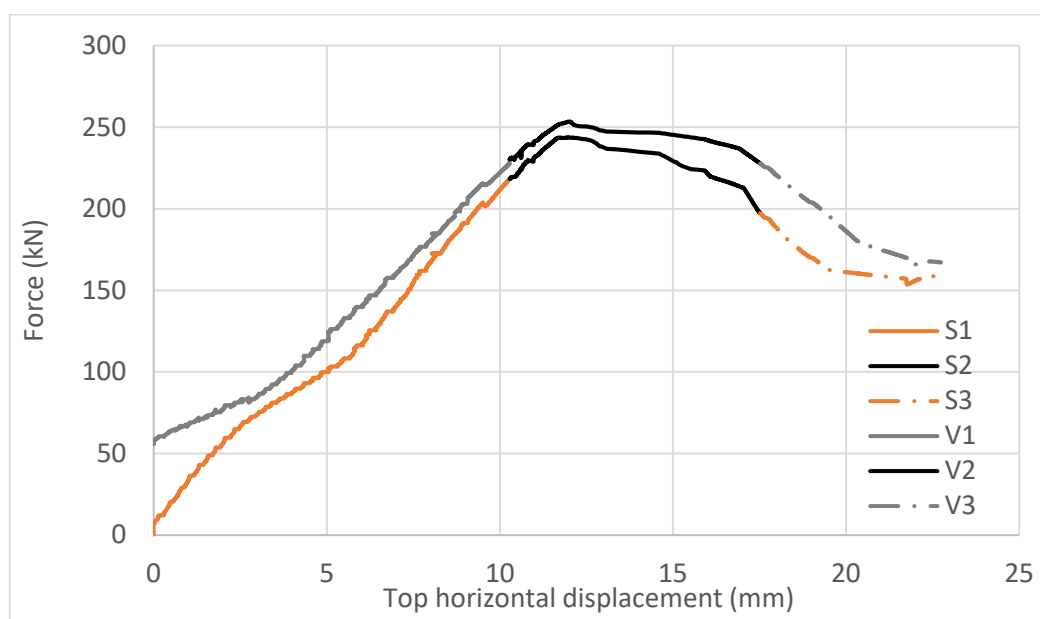


Figure 5.9: Shear and vertical force vs horizontal displacement of SW-75-150-02 specimen.

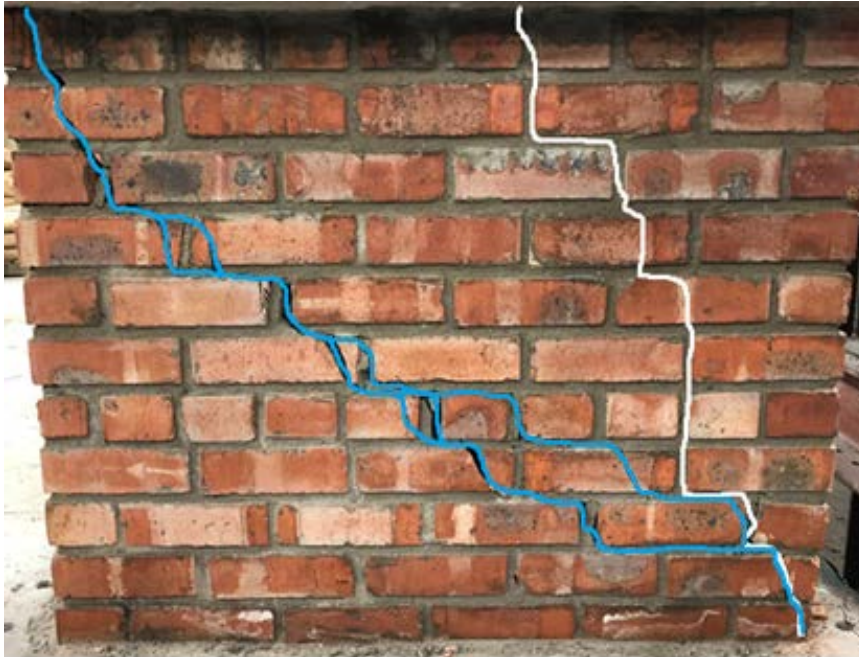
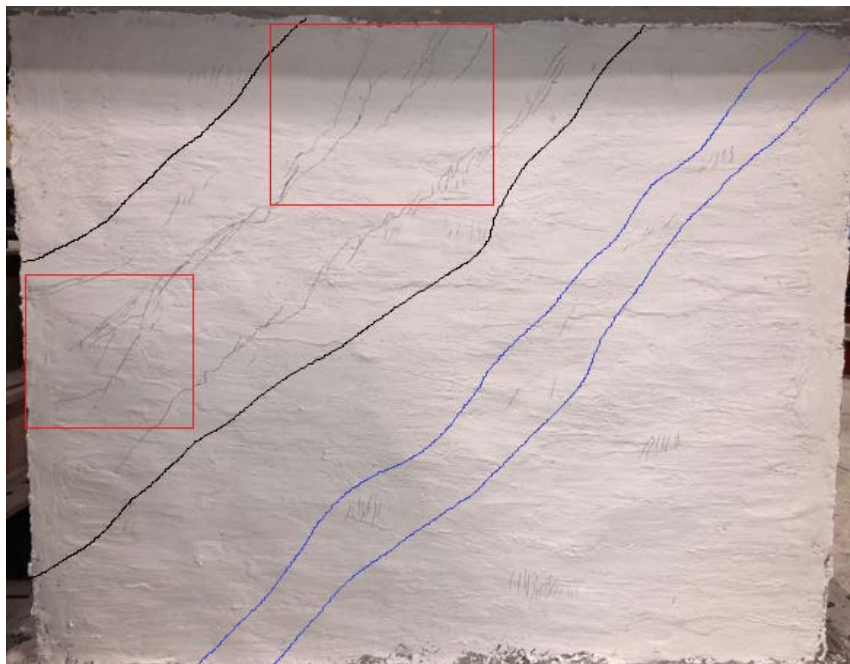


Figure 5.10: SW-75-150-02 crack pattern in the masonry.



(a)



(b)



(c)



(d)

Figure 5.11: SW-75-150-02 (a) Crack patterns during different cracking patterns outlined; (b) bottom enlarged photograph; (c) top enlarged photograph; (d) delamination.

SW-100-200-01

The shear and vertical forces vs the top horizontal displacement of the SW-100-200-01 specimen are shown in Figure 5.12. Multiple fine diagonal cracks start to form on the central diagonal strip at a shear force of 146.62 kN and a displacement of 5.6 mm. Hereafter, delamination starts from the bottom right-hand corner. Fine cracks are observed on the first strip above and below the central strip. The SHCC carries the load for approximately 7.2 mm, until the overlay completely delaminates from the masonry at a displacement of 13.13 mm. During the period of multiple crack formation, a maximum shear force of 168.78 kN is reached at an associated displacement of 10.73 mm. The crack path of the masonry is displayed in Figure 5.13, while the crack pattern in the SHCC overlay can be seen in Figure 5.14.

The ascending branch shows a higher stiffness to that of the SW-220-15-No Strips specimen. A lower maximum shear resistance is obtained due to delamination. The descending branch shows a steep response similar to the post-peak responses obtained by De Beer (2016) and the SW-220-15-No strips specimen.

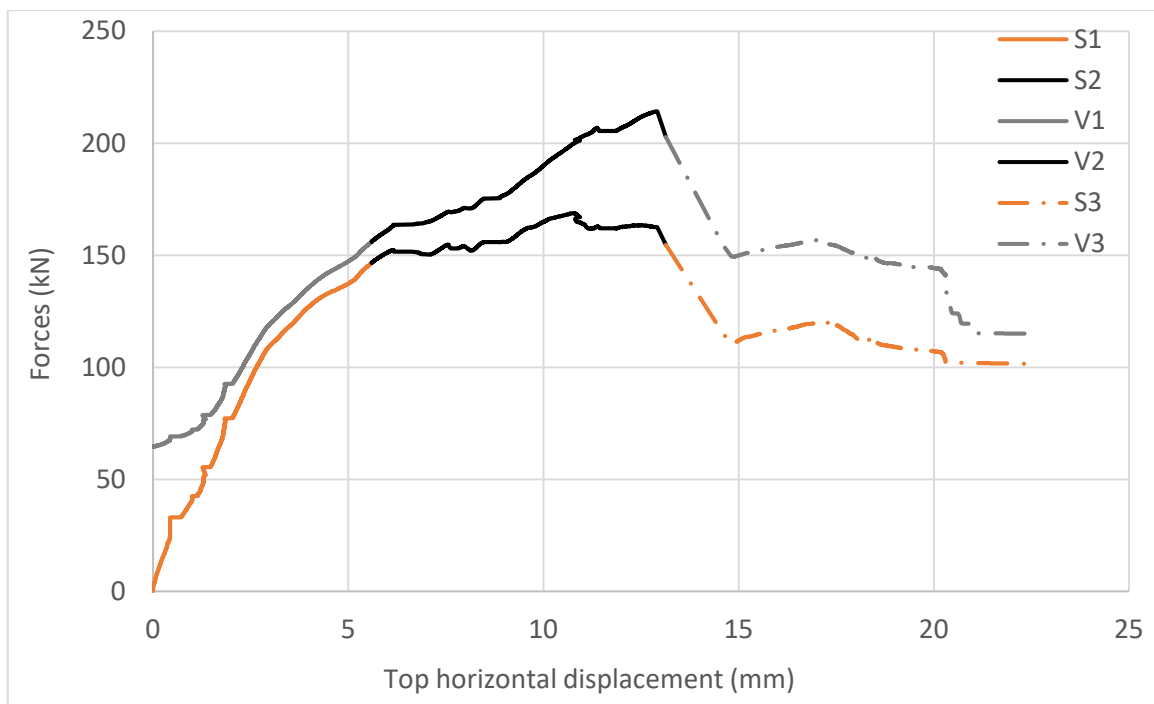


Figure 5.12: Shear and vertical force vs horizontal displacement of SW-100-200-01 specimen.

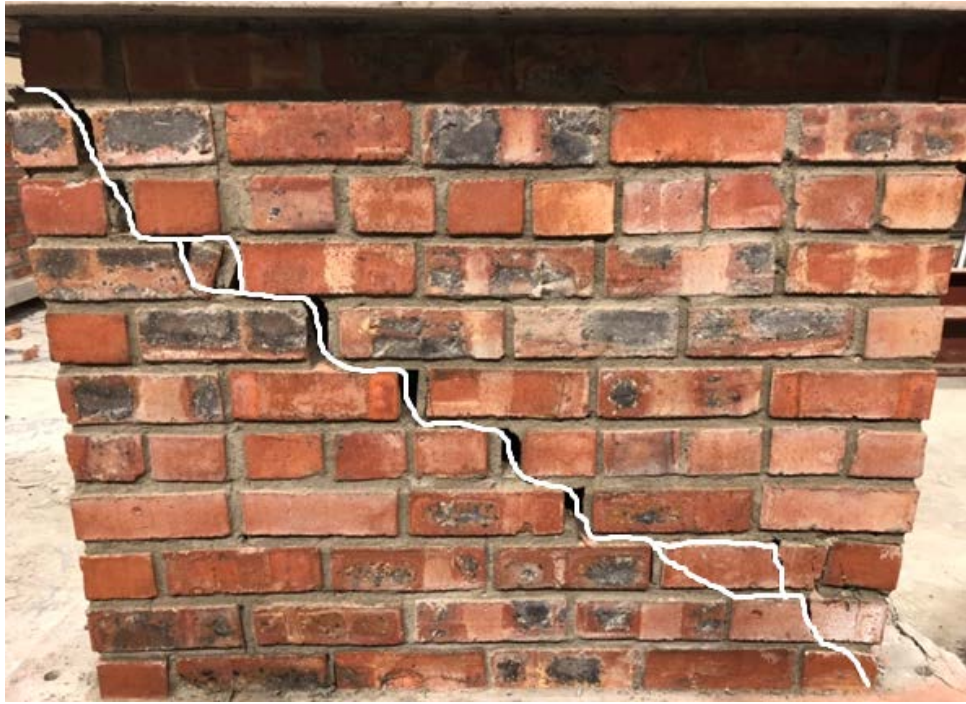


Figure 5.13: SW-100-200-01 crack pattern in the masonry.

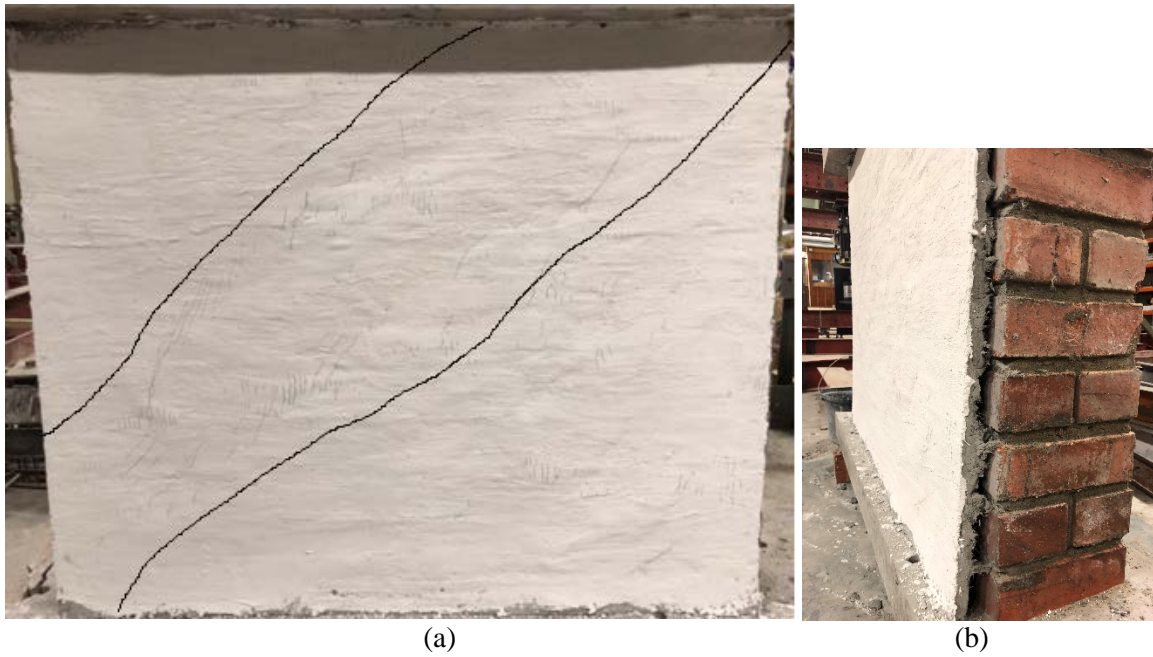


Figure 5.14: SW-100-200-01 (a) Crack patterns outlined; (b) delamination in bottom right corner.

SW-100-200-02

As the shotcrete process of spraying the SHCC to the masonry walls is performed in a similar manner to that of De Beer (2016), the overlays are sprayed to the top and bottom concrete beams, leaving no space between the overlay and RC beams. Consequently, the SHCC has a fixed restraint at its top and bottom. During testing, the axial tension forces increase within the vertical rods of row 2 and 3, applying higher forces on the top and bottom concrete beams. These forces cause downward deflection of the top beam, and upward deflection of the bottom beam, on the right-hand side. Due to the SHCC being fixed to the beams, an increased compression force is applied to the overlay. This compressive force causes the overlay to buckle and delaminate from the masonry as seen from the SW-75-150-02 and SW-100-200-01 specimens. The SHCC of the SW-100-200-01 specimen delaminated at a lower shear force due to its larger debonded interface area.

For the SW-100-200-02 specimen, 20 mm wide horizontal grooves are created at the top and bottom by grinding the SHCC from the masonry, Figure 5.15. The grooves enable free vertical movement of the top and bottom RC beams without applying compressive forces to the SHCC overlay, and hereby reducing the likelihood of delamination.



Figure 5.15: SW-100-200-02 2 cm horizontal grooves at (a) top and (b) bottom.

The shear and vertical forces vs the top horizontal displacement of the SW-100-200-02 specimen are shown in Figure 5.16. Fine diagonal cracks start to form on the diagonal at a shear force of 216.22 kN and a displacement of 9.08 mm. An ultimate shear force of 256.98 kN is reached at a displacement of 20.51 mm. A fully developed localised crack forms at a shear force of 250.3 kN and an associated displacement of 21.14 mm.

An initial crack forms in the masonry at the bottom right-hand corner, Figure 5.17. The crack grows horizontally towards the middle and the SHCC overlay manages to bridge the crack, preventing localised

failure in this bottom row of bricks. Hereafter, a new failure path initiates in the masonry on the diagonal. Multiple cracking starts and distributes on the central diagonal strip at a displacement of 9.08 mm. Cracks in the SHCC overlay move into the second strip below the central strip and an enlarged area of fine multiple cracks starts to form in the debonded interface region. Figure 5.18 shows the crack formation in the SHCC from which the enlarged crack distribution can be seen. The SW-100-200-02 specimen manages to withstand a shear force of more than 210 kN for 13.88 mm, showing the significant increase in ductility obtained by applying 100 mm debonded diagonal strips.

The primary and secondary ascending branch show reasonably similar stiffness to that of the SW-220-15-No Strips specimen. The primary ascending branch has reasonable agreement with the SW100-200-01 specimen, but a lower secondary branch is obtained. The ultimate shear resistance is in reasonable agreement with the SW-75-150-Strip Analysis model, but the maximum resistance is at a significantly higher horizontal displacement. The primary post-peak branch shows a descending slope for 0.72 mm, after which an ascending slope is obtained towards the secondary (ultimate) peak. The ascending branch after primary post-peak mobilises significant strain-hardening behaviour in the SHCC material in the regions of debonded interfaces.

Note, no delamination is observed during the test of the SW-100-200-02 specimen. Thus, it is clear that delamination of the SW-75-150-02 and SW-100-200-02 specimens occurred due to the buckling of the SHCC overlay, caused by the high compressive forces carried over from the pre-tension rods to the top and bottom RC beams and finally to the SHCC overlay.

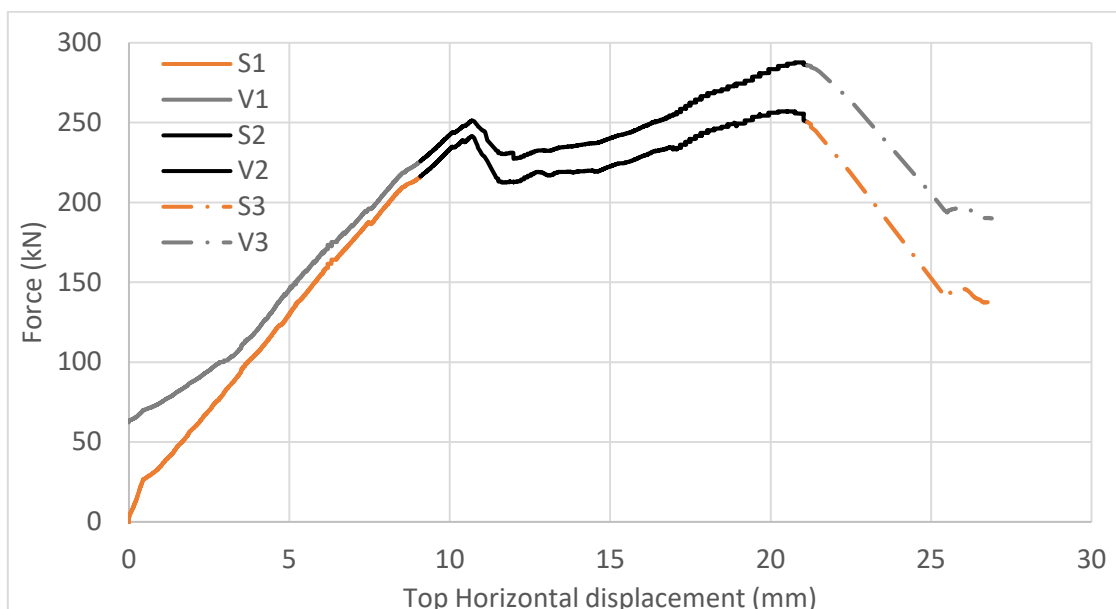


Figure 5.16: Shear and vertical force vs horizontal displacement of SW-100-200-02 specimen.



Figure 5.17: SW-100-200-02 crack pattern in the masonry.



Figure 5.18: SW-100-200-02 crack patterns outlined.

The width of all the cracks in the above-mentioned experimental specimens are 0.1 ± 0.05 mm, before crack localisation and widening in the post-peak softening branch. Full crack saturation over the SHCC overlay diagonal is not achieved, but in regions of apparent saturation, the crack spacing is approximately 10 mm as seen in Figure 5.19.

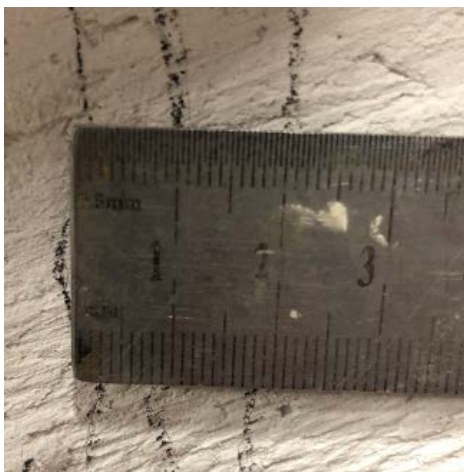


Figure 5.19: Crack spacing

5.4 Shear wall results comparison

The results discussed in Section 5.3 on the masonry walls retrofitted with SHCC overlay with and without debonded strip interfaces are compared in this section. A safety margin indicating the energy (ductility) contribution is determined and discussed.

5.4.1 Shear walls test results summary

Figure 5.20 displays the shear force vs top horizontal displacement of the computational and experimental tests performed on the double leaf (220 mm thick) masonry wall retrofitted with 15 mm SHCC overlay, with and without debonded strip interfaces. The ultimate shear and vertical forces and stresses with their associated displacements of the experimental tests are summarised in Table 5.2.

The SW-75-150-Strip Analysis, SW-75-150-01 and SW-75-150-02 tests show a variation in the ascending branch and the ultimate shear resistance, but a reasonable agreement in the post-peak trend, Figure 5.20. All three of these tests show a less steep descending branch compared to that of the test excluding debonded strips. No analysis is performed using a 100 mm strip width and 200 mm centre to centre spacing. However, for the SW-100-200-02 test, an initial descending branch is obtained after the primary peak resistance, after which an ascending branch follows leading to the high ultimate shear

resistance. This behaviour shows the significant ductility increase due to the effectiveness of the strain-hardening behaviour being exhibited by the SHCC overlay and debonded strip interface combination.

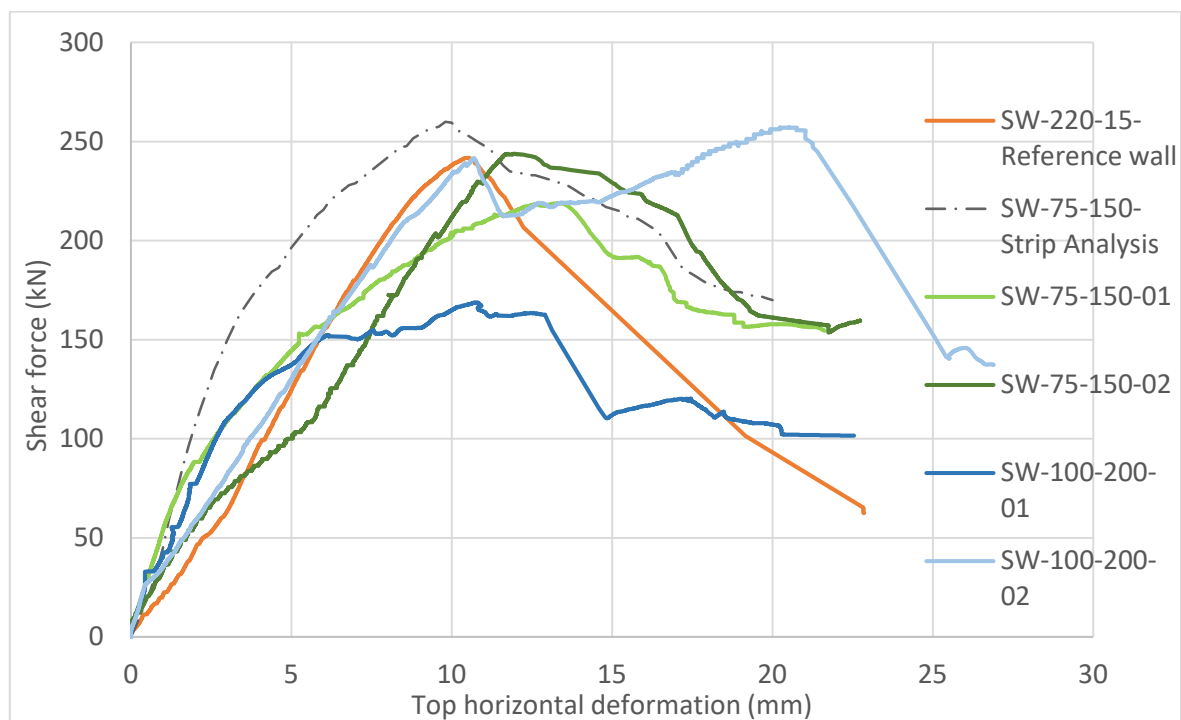


Figure 5.20: Summary of shear walls shear force vs displacement results.

Table 5.2: Experimental tests maximum shear and vertical forces and stresses with its associated displacements.

| Specimen | Shear | | | Vertical | | |
|----------------------|----------------|-------------------------------|------------------------------|----------------|-------------------------------|------------------------------|
| | Max force (kN) | ¹ Max Stress (MPa) | Horizontal Displacement (mm) | Max force (kN) | ² Max Stress (MPa) | Horizontal Displacement (mm) |
| SW-220-150-Reference | 241.74 | 0.96 | 10.51 | 262.41 | 1.04 | 10.58 |
| SW-75-150-01 | 218.92 | 0.87 | 13.31 | 238.26 | 0.94 | 13.70 |
| SW-75-150-02 | 243.76 | 0.96 | 11.94 | 253.36 | 1.00 | 12.02 |
| SW-100-200-01 | 168.78 | 0.67 | 10.73 | 214.18 | 0.85 | 12.90 |
| SW-100-200-02 | 256.98 | 1.02 | 20.51 | 287.60 | 1.14 | 20.75 |

¹Average shear stress obtained by dividing maximum shear force by the wall horizontal cross-section

²Average normal stress obtained by dividing the maximum total vertical force by the wall horizontal cross-section

5.4.2 Debonded strip interface energy contribution

The ductility factor discussed in Section 2.10 is 3.1 for the SW-100-200-01 specimen and 2.7 for the SW100-200-02 specimen. Thus, showing that it is inappropriate for the walls tested in this study as it does not account for the shear strength. Here, the energy dissipation contribution due to the application of the debonded strip interfaces is discussed. Energy is determined by force times distance in the force direction. Higher energy dissipation indicates that a more effective strain-hardening response is obtained from the SHCC overlay. Increased ductility is obtained when a constant force is maintained over a longer displacement. The primary aim of this research is to obtain a higher in-plane shear ductility response from the retrofitted shear walls.

Figure 5.21 shows the shear force vs horizontal displacement of the SW-220-15-No Strip (Reference) and SW-75-150-02 specimens. The dotted area is the energy dissipation at a force of 200 kN of the reference wall, while the hatched area shows the energy dissipation of a specimen containing 75 mm debonded strips at the same shear force level. The Energy Contribution Factor (ECF) is determined at different forces, to compare the energy dissipation contributed by the debonded strip interfaces to that of a specimen without these strips (Reference wall). Thus, the energy dissipated at a force level resisted by a wall without strips times the associated ECF will result in the approximate energy dissipated at that force, for the associated strip method. Equations 5.1 and 5.2 express the determination of the ECF.

$$\Delta = \partial 2 - \partial 1 \quad (5.1)$$

$$ECF = \Delta_{strip} - \Delta_{ref} \quad (5.2)$$

Where

- Δ Total displacement withstanding the constant force or a force exceeding it; measured for reference (Δ_{ref}) and strip (Δ_{strip}) specimens
- $\partial 1$ First displacement at which force is reached in the ascending branch
- $\partial 2$ Final displacement at which force is maintained in the descending branch

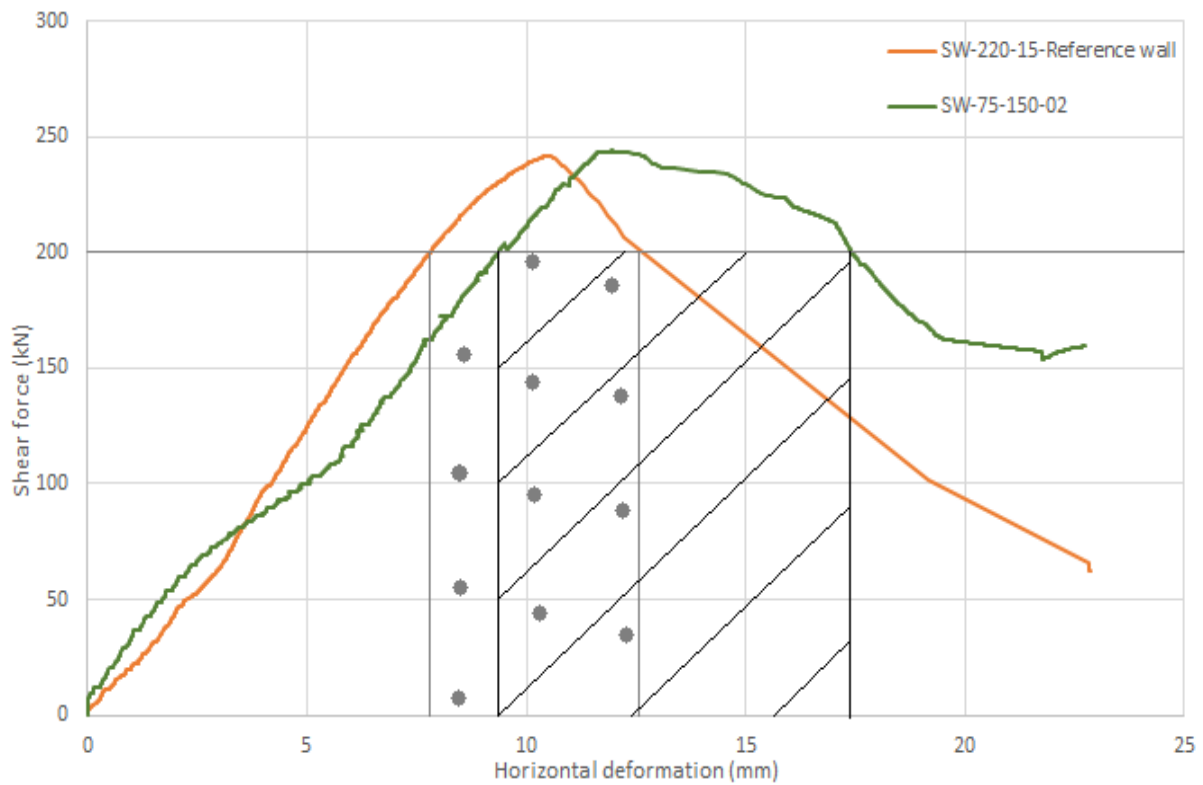


Figure 5.21: Shear force vs displacement with indicated energy at a 200 kN force.

SW-75-150

Here, the energy contribution of the SW-75-150-01 and SW-75-150-02 specimens is discussed. The horizontal lines in Figure 5.22 show at which shear forces the energy contribution of the SW-75-150-01 specimen is determined. The ECF is determined at 150, 175 and 200 kN forces and summarised in Table 5.3. The ECF at a shear force of 200 kN is smaller than 1, indicating that the strip specimen contributes less energy, but it can be seen as negligible due to the factor being smaller by only 0.02. The ECF increases as the forces decrease and a high factor of 2.1 is obtained at a force of 150 kN.

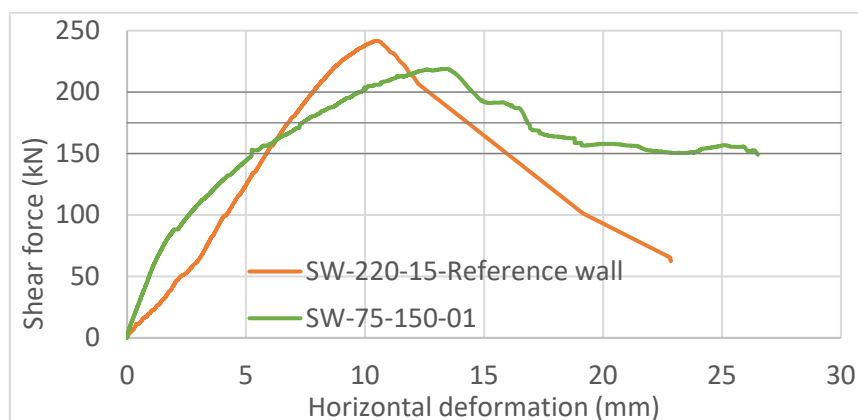


Figure 5.22: Horizontal forces for determining ECF of SW-75-150-01.

Table 5.3: ECF factor of SW-75-150-01.

| Force (kN) | Reference | | | SW-75-150-01 | | | ECF |
|------------|--------------|--------------|----------|--------------|--------------|----------|------|
| | $\partial 1$ | $\partial 2$ | Δ | $\partial 1$ | $\partial 2$ | Δ | |
| 150 | 5.86 | 15.96 | 10.10 | 5.24 | 26.48 | 21.24 | 2.10 |
| 175 | 6.78 | 14.32 | 7.54 | 7.36 | 16.80 | 9.44 | 1.25 |
| 200 | 7.81 | 12.67 | 4.87 | 9.75 | 14.52 | 4.77 | 0.98 |

The horizontal lines in Figure 5.23 show at which shear forces the energy contribution of the SW-75-150-02 specimen is determined. The ECF is determined at 150, 175, 200 and 225 kN forces and can be seen in Table 5.4. Note, the shear force does not decrease to below 150 kN in the descending branch during the test. However, the associated displacement of the lowest shear force (153.64 kN) is used as the value of $\partial 2$, which is more conservative. This specimen shows a significant increase in energy dissipation.

Table 5.5 displays the average ECF of the two specimens containing 75 mm width strips. A significant energy increase is obtained by retrofitting a masonry wall with 15 mm SHCC overlay and 75 mm diagonal debonded strip interfaces. Note, the delamination of the SHCC overlay led to lower energy dissipation. Higher ductility would most likely have been obtained by eliminating the top and bottom restraint as done with the SW-100-200-02 specimen.

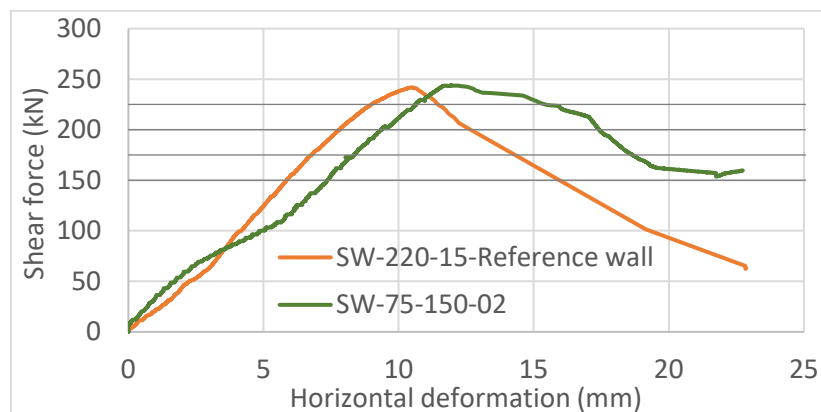


Figure 5.23: Horizontal forces for determining ECF of SW-75-150-02.

Table 5.4: ECF factor of SW-75-150-02.

| Force (kN) | Reference | | | SW-75-150-02 | | | ECF |
|------------|--------------|--------------|----------|--------------|--------------|----------|------|
| | $\partial 1$ | $\partial 2$ | Δ | $\partial 1$ | $\partial 2$ | Δ | |
| 150 | 5.86 | 15.96 | 10.10 | 7.35 | 21.75 | 14.40 | 1.43 |
| 175 | 6.78 | 14.32 | 7.54 | 8.35 | 18.66 | 10.31 | 1.37 |
| 200 | 7.81 | 12.67 | 4.87 | 9.35 | 17.42 | 8.07 | 1.66 |
| 225 | 8.99 | 11.47 | 2.47 | 10.63 | 15.41 | 4.79 | 1.93 |

Table 5.5: Average ECF of specimens with 75 mm strips.

| Force (kN) | SW-75-150 ECF |
|------------|---------------|
| 150 | 1.76 |
| 175 | 1.31 |
| 200 | 1.32 |
| 225 | 1.93 |

SW-100-200

Here, the energy contribution of the SW-100-200-02 specimen is discussed. The energy contribution of the SW-100-200-01 specimen is not determined due to early delamination. The horizontal lines in Figure 5.24 show at which shear forces the ECF of the SW-75-150-02 specimen is determined.

The ECF is determined at 150, 175 and 200 kN and 225 kN forces and can be seen in Table 5.6. Note that the constant horizontal 225 kN shear force line intersects with two ascending and two descending branches. Therefore, $\partial 1$ and $\partial 2$ are the displacements at the first descending and ascending branches respectively, while $\partial 3$ and $\partial 4$ are the displacements at the second ascending and descending branches. The value for $\Delta_{\text{SW-100-200-02}}$ is determined as follows:

$$\Delta = (\partial 2 - \partial 1) + (\partial 4 - \partial 3) \quad (5.3)$$

A significant energy dissipation increase is obtained by this specimen containing 100 mm strips. This shows the high ductility increase obtained by applying 15 mm SHCC overlay and 100 mm diagonal debonded strip interfaces.

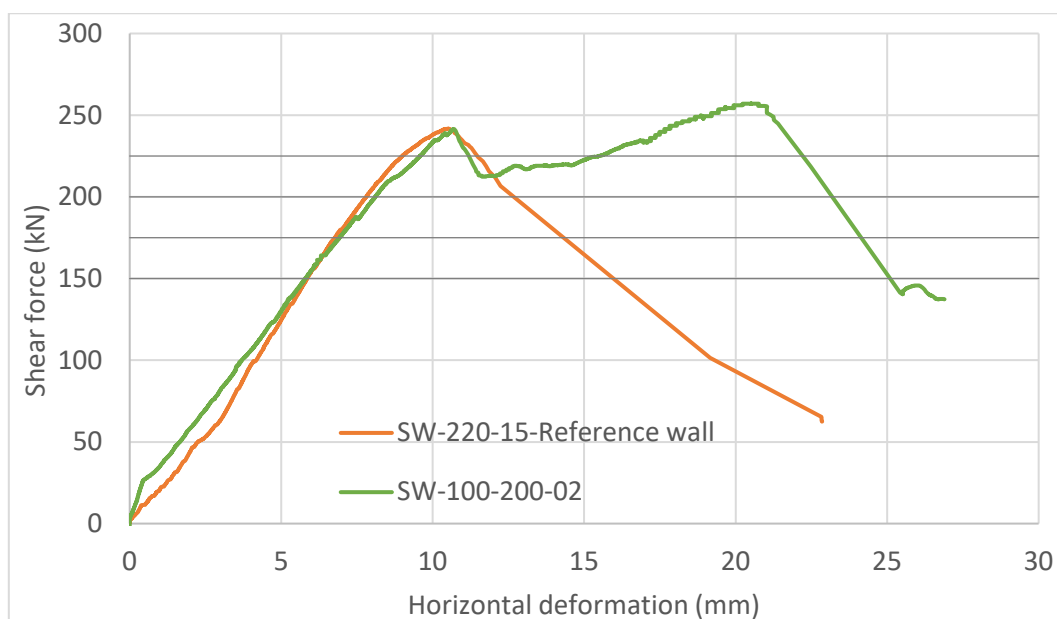


Figure 5.24: Horizontal forces for determining ECF of SW-100-200-02.

Table 5.6: ECF factor of SW-100-200-02.

| Force (kN) | Reference | | | SW-100-200-02 | | | | | ECF |
|------------|--------------|--------------|----------|---------------|--------------|--------------|--------------|----------|------|
| | $\partial 1$ | $\partial 2$ | Δ | $\partial 1$ | $\partial 2$ | $\partial 3$ | $\partial 4$ | Δ | |
| 150 | 5.86 | 15.96 | 10.10 | 5.79 | 25.10 | - | - | 19.31 | 1.91 |
| 175 | 6.78 | 14.32 | 7.54 | 6.93 | 24.14 | - | - | 17.21 | 2.28 |
| 200 | 7.81 | 12.67 | 4.87 | 8.10 | 23.19 | - | - | 15.09 | 3.10 |
| 225 | 8.99 | 11.47 | 2.47 | 9.59 | 11.17 | 15.48 | 22.21 | 8.32 | 3.36 |

5.5 Concluding Summary

Results and discussions are given in Section 4.1.2 on the nonlinear computational modelling of a double leaf shear wall retrofitted with 15 mm overlay and 75 mm debonded strip interfaces. A more ductile behaviour is predicted by this model when debonded strips are applied. This is made possible by the strain-hardening response being distributed over a larger area.

From the results discussed on the five SWS in Section 5.3 and the results comparison in Section 5.4, the following conclusions can be drawn:

- Testing shear walls with an increase in vertical (rods) forces led to the successful shear failure of the walls on the diagonal.

- The reference specimen showed a reasonably similar ascending and descending slope, and also ultimate shear resistance compared to the three experimental results performed by De Beer (2016). Multiple crack formation occurred in a more localised region and a steep post-peak descending slope is obtained by this specimen.
- Specimens containing 75 mm diagonal debonded strips showed an increased ductility compared to the reference specimen. Localised and multiple cracks distributed over two of the debonded strips in the SW-75-150-01 specimen, leading to increased strain-hardening behaviour. Reasonable agreement in the post-peak behaviour of this specimen and the SW-75-150-Strip Analysis is obtained. High ultimate resistance and crack distribution area are obtained from the SW-75-150-02 specimen. High forces are maintained until buckling of the SHCC led to delamination.
- Buckling and delamination of the SW-100-200-01 specimen occurred at an early stage during testing at the same position as in the SW-75-150-02 specimen. Thereafter, grooves created in the SHCC at the top and bottom of the SW-100-200-02 specimen eliminated this failure mechanism.
- Initial cracking in the masonry led to the first peak response of the specimen, after which a second diagonal crack is maintained at high forces until the ultimate shear resistance is reached. A significant ductility enhancement and a large cracking region are obtained.
- Higher forces and ductility behaviour are expected from the 75 mm strip specimens with grooves at the top and bottom.
- The determination of the Energy Contribution Factor (ECF) shows that higher energy dissipation is obtained by adding of the two different debonded strip patterns. Higher energy is contributed in the specimen containing 100 mm strips than those with 75 mm strips. However, it is difficult to compare the two strip patterns as the 75 mm strip specimens are subjected to compressive forces from the top and bottom concrete beams, bearing onto the SHCC overlay.
- An energy dissipation factor (ECF) has been defined to express the increased energy in walls containing strip debonded SHCC overlay compared with walls without these debonded strips. For the wall with 100 mm debonded strips, and where the bearing between foundation and floor beams onto the overlay is prevented, and thereby premature delamination, ECF factors ranging between 1.91 and 3.36 are realised. This indicates significantly enhanced ductility in shearing response of the retrofitted walls by the debonded strips.

Chapter 6

Conclusions and Recommendations

6.1 Conclusions

This research is motivated by the large number of ULM structures constructed prior to the standardisation of design for seismic activity in the South African Standard in 1989. A significant stock of multi-story unreinforced load bearing masonry (ULM) structures are found in the Cape Town area. This region is categorized as a light to moderate seismic region. Retrofitting techniques of these buildings have been proposed at Stellenbosch University by a group of researchers, as poor behaviour of the buildings is expected during seismic activity due to their brittle response to lateral excitation. A Strain Hardening Cement-based Composite (SHCC), which can be easily applied by spraying, without losing its characteristic mechanical properties, was developed as a retrofitting material to improve shear behaviour during seismic events.

Nonlinear FEA have been performed to simulate the responses of shear walls retrofitted with SHCC overlays and previously tested at SUN. Having calibrated the computational model to obtain reasonable agreement with the behaviour measured on experimental walls, analyses have been extrapolated to investigate different wall and overlay thicknesses. A new retrofitting technique, by which an SHCC overlay with debonded strip interfaces are applied to the masonry has been developed with the primary aim of improving the ductility performance. Encouraged by the computed ductility of this retrofitting strategy, validating laboratory experimental tests have been performed on five shear walls. To express the ductility added by the debonded strips, the concept of the energy contribution factor (ECF) has been developed.

This research contributes towards the process of redressing design literature for increasing the performance of ULM buildings retrofitted with an SHCC overlay. From the work done in this research the following conclusions are drawn.

6.1.1 Nonlinear FEA and calibration

- By computational modelling with the use of the DIANA software, the results of the bare ULM shear walls without SHCC overlays tested by De Beer (2016) are simulated with reasonable agreement. The Rankine-Hill plasticity plane stress model used for the masonry as a continuum is thus sufficient, the boundary conditions of the experimental setup appropriately simulated, and the material model parameters are sufficiently calibrated.

- As expected, the bare masonry shear walls have an increase in ultimate shear resistance with an increase in the wall thickness.
- A significant variation in the second ascending branch gradient of the shear load-deformation response is observed for the three identical shear walls with 15 mm SHCC overlays tested by De Beer (2016). The computed response of the SW220-15 model does not capture the behaviour in this region accurately. However, a good representation of the mean ultimate shear strength with its associated displacement is computed. A reasonably similar post-peak behaviour to that tested by De Beer (2016) is obtained. Thus, the smeared rotational cracking model used to model the SHCC overlay as a retrofitting material can be considered as reasonable.
- By retrofitting the bare 220 mm thick ULM wall with a 15 mm SHCC overlay, a 98.5 increase in the ultimate shear strength is obtained, demonstrating the enhanced benefits of the composite material when subjected to a seismic loading regime.
- Large principle strains developed on the diagonal, and in the compressive strut toe and heel indicating that shear and rotational forces are present. However, the strains are dominant on the diagonal as the load increases, showing that shear failure occurs under the test boundary constraints.
- The 110, 220 and 330 mm thick masonry walls showed an increase in shear resistance with an increase in SHCC overlay thickness. Note that an increase in SHCC overlay thickness in the range 10 to 30 mm leads to a lower increase in the ultimate shear strength with an increase in masonry thickness.
- The algebraic minimum principle stresses (S_2) in the SW220-15 computational model indicate toe crushing at its bottom left-hand corner. However, this occurs after localisation on the diagonal. Toe crushing also occurs in the SW110-30 model, but not in the 330 mm thick masonry wall model.
- Although a significant increase in resistance is obtained by applying the SHCC overlay, a retrofitting technique is required to avoid or reduce the unfavourable sudden drop in resistance beyond the peak.

6.1.2 Debonded strip interface computational modelling

- The debonded diagonal strip interfaces are successfully modelled with the use of an interface material model with low normal and tangential stiffness to simulate a smooth surface.
- The model, containing five 75 mm width strips with 150 mm centre to centre spacing, computes a similar ultimate shear strength compared to the fully bonded SW220-15 model.

- The computed post-peak response of the strip debonded overlay model has a less steep descending branch compared to that of the SW220-15 model, indicating increased ductility and higher energy dissipation.
- A larger diagonal region of high algebraic maximum principle strain (E1) is observed in the strip debonded overlay model, indicating that more cracks are likely to form over this enlarged region than in the case of the fully bonded overlay.

6.1.3 Shear wall experimental validation

Successful validating large scale experimental shear tests have been performed on five double leaf (220 mm thick) masonry shear walls retrofitted with 15 mm SHCC overlays, from which the following conclusions can be drawn:

- Shear failure occurred in all five walls on the diagonal. The forces in the off-centre, vertical tie rods increased with a 1:1 ratio to the horizontal shear force as cracking started.
- The reference specimen, with a fully bonded SHCC overlay, showed a reasonably similar ultimate shear resistance and descending load-deformational slope compared to the three experimental shear walls tested by De Beer (2016). The second ascending branch fell within the envelope defined by those of the three walls tested by De Beer (2016). Multiple cracks formed in a relatively narrow diagonal band of this specimen. Therefore, the materials of the masonry wall, test setup and control used for the SHCC and shear wall testing setup is validated to be reasonably similar to that implemented by De Beer (2016).
- Two walls containing 75 mm diagonal debonded strips exhibited an increased ductile behaviour compared to the reference specimen.
- Localised and multiple cracks formed in the SHCC overlay in two of the debonded strip regions in the SW-75-150-01 specimen, suggesting increased strain-hardening behaviour in these regions. The crack pattern resembles the region of high principle strains (E1) diagram computed for the SW-75-150-Strip Analysis model.
- Reasonably similar post-peak behaviour of this specimen and the SW-75-150-Strip Analysis is obtained. For the SW-75-150-02 specimen, a large distributed crack region is obtained. High forces are maintained until buckling of the SHCC led to delamination.
- Buckling and delamination of the SW-100-200-01 specimen occurred at an early stage during testing at the same position as in the SW-75-150-02 specimen. As the vertical rod forces increased during testing, the top and bottom concrete beams had downward and upward movement respectively, causing the overlay to buckle and delaminate as it is restrained at its top and bottom. Thereafter, grooves are created in the SHCC at the top and bottom of the SW-100-200-02 specimen and this failure mechanism is eliminated.

- Initial cracking in the masonry led to the first peak response of the SW-100-200-02 specimen, after which a second diagonal crack is maintained at high forces until the ultimate shear resistance is reached. A significant ductility enhancement and a large cracking region are obtained.
- Higher shear resistance and ductility are expected from the 75 mm strip specimens with grooves at the top and bottom, i.e. avoiding contact between the overlay and upper and lower floors, or the foundation.
- The Energy Contribution Factor (ECF) expresses the higher energy dissipation obtained with the debonded strips. Higher energy is contributed in the specimen containing 100 mm strips than those with 75 mm strips. However, delamination most likely reduced the energy contribution in the 75 mm strip specimens due to the compression exerted by the top and bottom concrete beams.

6.2 Recommendations

From the insights gained during this research, the following issues are recommended for further investigation:

- Development of spray-able SHCC materials to obtain maximum strength and strain by optimizing the mixture design, and also taking ageing effects that include loss of ductility of the SHCC into account.
- Conduct more shear walls tests on specimens containing similar overlay thickness and debonded strip widths and spacing as in this research, but all having grooves at top and bottom as validation of the improved performance if contact with upper and lower floors or the foundation is avoided.
- Conduct more tests on shear walls containing different debonded strip interface patterns than those used in this research.
- Perform nonlinear computational analysis on full-scale walls containing window openings, replicating a multi-story ULM shear wall. Model these walls bare and retrofitted with SHCC overlay and with debonded strip interfaces.
- For the subsequent step towards full three-dimensional modelling of a multi-story building, the use of layered shell elements instead of membrane elements is recommended.
- Perform nonlinear computational analysis on full scale ULM buildings. Develop such models with the different retrofitting techniques discussed in this research.

- Assess the durability benefits held in SHCC when used to retrofit masonry in terms of water ingress.
- The application of cross-diagonal debonded strips to capture multiple cracks under cyclic load should be verified for sufficient prevention of fresh SHCC run-off during the spraying process, and delamination in the hardened state due to further reduced bonded surface.
- A design model for SHCC overlay retrofit should be developed with pertinent expression of designed ductility increase. For the simplified equivalent push-over approach in earthquake design, an increased value of the behaviour factor of ULM walls retrofitted with a ductile overlay is recommended.
- Determination of the regional earthquake displacement demand, considering the particular founding soil type, will enable confirmation whether the added masonry shear wall deformation capacity is sufficient to exceed the demand.

References

- Alexander, Mark and Beushausen, H. D. (2009) 'Fulton's Concrete Technology'. Cement and Concrete Institute, Midrand, South Africa, 9, pp. 111–146.
- ASTM C109 (2010) 'Standard Test Method for Compressive Strength of Hydraulic Cement Mortars (Using 2-in. or [50-mm] Cube Specimens) 1', in *Annual Book of ASTM Standards i.C.*, pp. 1–9. doi: 10.1520/C0109.
- ASTM E518-10 (2010) 'Standard test method for flexural bond strength of masonry. American Society for Testing and Materials, West Conshohocken'.
- De Beer, L. R. (2016) 'Developing and testing a sprayable overlay of Strain Hardening Cement-based Composite for retrofitting of unreinforced load bearing by', (October).
- Boshoff, W. P. and Van Zijl, G. P. A. G. (2007) 'A computational model for strain-hardening fibre-reinforced cementbased composites', *Journal of the South African Institution of Civil Engineering*, 49(2), pp. 24–31.
- Bruneau, M. (1994) 'STATE-OF-THE-ART REPORT ON SEISMIC PERFORMANCE OF UNREINFORCED MASONRY BUILDINGS', *Journal of Structural Engineering*, 120(1), pp. 230–251.
- BS EN 772-1 (2011) 'Methods of test for masonry units-Part1: Determination of compressive strength.', in *British Standards Institution. London, United Kingdom.*
- Chandra Paul, S. and P. A. G. van Zijl, G. (2014) 'Crack Formation and Chloride Induced Corrosion in Reinforced Strain Hardening Cement-Based Composite (R/SHCC)', *Journal of Advanced Concrete Technology*, 12(9), pp. 340–351. doi: 10.3151/jact.12.340.
- Curosu, I., Mechtcherine, V. and Millon, O. (2016) 'Effect of fiber properties and matrix composition on the tensile behavior of strain-hardening cement-based composites (SHCCs) subject to impact loading', *Cement and Concrete Research*. Elsevier Ltd, 82, pp. 23–35. doi: 10.1016/j.cemconres.2015.12.008.
- Dehghani, A., Fischer, G. and Alahi, F. N. (2013) 'Strengthening masonry infill panels using engineered cementitious composites', *RILEM 2013*.
- ElGawady, Ma, Lestuzzi, P and Badoux, M. (2006) 'Retrofitting of masonry walls using shotcrete', *2006 NZSEE Conference, Yeni ... 45*, pp. 45–54.
- EN 1998-1 (2005) 'Design of structures for earthquake resistance Part 1: general rules, seismic actions, and rules for buildings', *December 2005, European Committee for Standardization*.

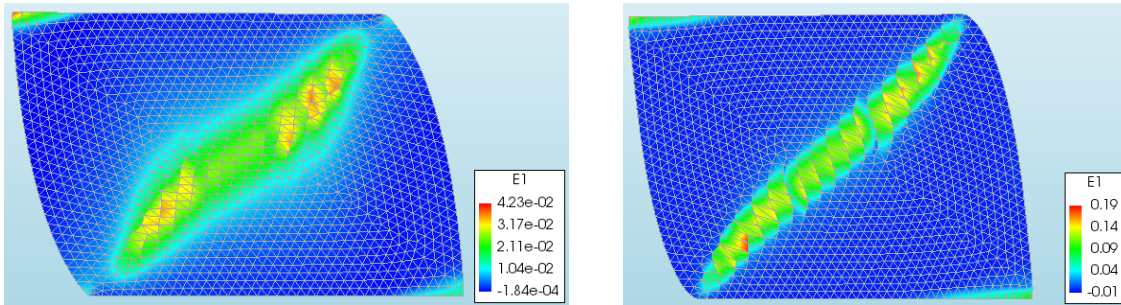
- Kim, Yong, Y. and Kong, Hyun-joon and Li, V. C. (2003) 'Design of Engineered Cementitious Composite Suitable for', (100).
- Van Der Kolf, T. (2014) 'The Seismic Analysis of a Typical South African', (April).
- Lim, Y. . and V. C. (1997) 'Durable repair of aged infrastructures using trapping mechanism of engineered cementitious composites', *Cement and Concrete Composites*, 19(4): 373-385.
- Lin, Yi Wei, Wotherspoon, Liam, Scott, Allan and Ingham, J. M. (2014) 'In-plane strengthening of clay brick unreinforced masonry wallettes using ECC shotcrete', *Engineering Structures* 66, pp. 57–65. doi: 10.1016/j.engstruct.2014.01.043.
- Lourenco, P. B. H. (1996) *Computational strategies for masonry structures*. Dissertation, Delft University of Technology, The Netherlands.
- Luković, M., Dong, H., Šavija, B., Schlangen, E., Ye, G., Van Breugel, K. (2014) *Tailoring strain-hardening cementitious composite repair systems through numerical experimentation*. *Cement & Concrete Composites*.
- Luković, M., Šavija, B., Schlangen, E., Ye, G., Van Breugel, J. (2014) 'A modelling study of drying shrinkage damage in concrete repair systems. M.C. Forde (ed.)', in *Proceedings of Structural Faults & Repair*. London, UK.
- Mahmood, H. and Ingham, J. M. (2014) 'Diagonal compression testing of FRP-retrofitted unreinforced clay brick masonry wallettes', *ASCE Journal of Composites for Construction*, 15(5):810-820.
- Manie, J. and Kikstra, W. P. (eds) (2017) 'Diana FEA - User's Manual. Release 10, Diana FEA - User's Manual. Release 10.' Delph, The Netherlands: DIANA FEA. Available at: dianafea.com.
- Palacio, K. (2013) 'Practical Recommendations for Nonlinear Structural Analysis in DIANA', (July).
- Rots, J. . and Blaawendraad, J. (1989) 'Discrete vs smeared crack modeling.pdf'.
- Le Roux, R. and Wium, J. (2012) 'Assessment of the behaviour factor for the seismic design of reinforced concrete structural walls according to SANS 10160', *part 4*. *Journal of the South African Institution of Civil Engineering*, 54(1):69–80.
- SABS 0160 (1989) 'The structural use of masonry, part 1: Unreinforced masonry walling', *SABS*.
- SANS 10160-4 (2011) 'Basis of structural design and actions for buildings and industrial structures, Part 4: Seismic actions and general requirements for buildings', *SANS*.
- SANS 10249 (2012) 'Masonry walling', in *SANS*.
- Saradj, F. M. (2007) *Earthquake Intensity, Damage, and Conservation of Unreinforced Masonry Buildings*, *Architectural Science Review*. doi: 10.3763/asre.2007.5019.

- Stander, H. (2007) *Interfacial bond properties for ECC overlay systems*. MScEng. University of Stellenbosch.
- Tomazevic, M. (1999) 'Earthquake-resistant design of masonry buildings (Vol. I)', *London: Imperial College Press*.
- Visser, C. R. (2007) *Mechanical and structural characterisation of extrusion moulded SHCC*. MScEng Thesis. University of Stellenbosch.
- Wang, Shuxin and Li, V. C. (2006) 'High-early-strength engineered cementitious composites'. 103.2, p. 9.
- Yi-Wei Lin, L. W. (2014) 'In-plane strengthening of clay brick unreinforced masonry wall panels using ECC shotcrete. *Engineering Structures*, 66, 57-65.'
- Zang, J. (2015) *Developing non-heat treated UHPC in South-Africa*. University of Stellenbosch.
- Van Zijl, G.P.A.G., Stander, H. (2009) 'SHCC repair overlays for RC: Interfacial bond characterization and modelling. M.G. Alexander, H.-D. Beushausen, F. Dehn, P. Moyo (eds.), *Proceedings of the 2nd International Conference on Concrete Repair, Rehabilitation and Retrofitting (ICRRR-2)*'. Cape Town, South Africa, Taylor & Francis Group, London, UK, 2009.
- Van Zijl, G. P. A. G. and De Vries, P. A. (2005) 'Masonry wall crack control with carbon fiber reinforced polymer', *Journal of Composites for Construction*, 9(1), pp. 84–89. doi: 10.1061/(ASCE)1090-0268(2005)9:1(84).
- Van Zijl, G. P. A. G. (2000) *Computational Modelling of Masonry Creep and Shrinkage*. Dissertation, Delft University of Technology, The Netherlands.
- Van Zijl, G. P. A. G. (2007) 'Improved mechanical performance: Shear behaviour of strain-hardening cement-based composites (SHCC)', *Cement and Concrete Research*, 37(8), pp. 1241–1247. doi: 10.1016/j.cemconres.2007.04.009.
- Van Zijl, G. P. A. G. *et al.* (2012) 'Durability of strain-hardening cement-based composites (SHCC)', *Materials and Structures*, 45(10), pp. 1447–1463. doi: 10.1617/s11527-012-9845-y.

Appendices

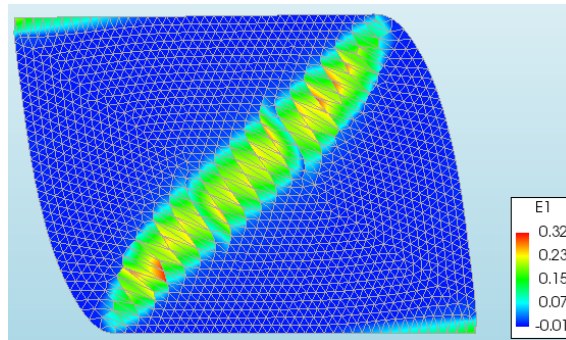
Appendix A – Computational models without strips

With and without bonded SHCC overlay



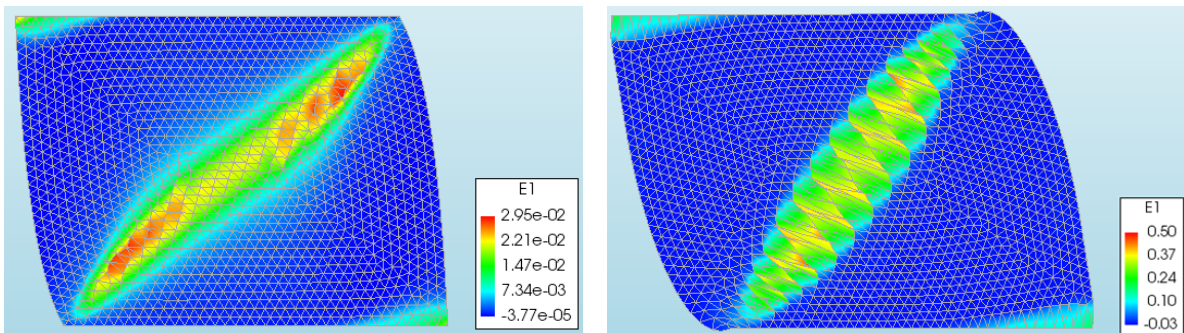
(a) 2.2 mm horizontal displacement

(b) 4.1 mm horizontal displacement



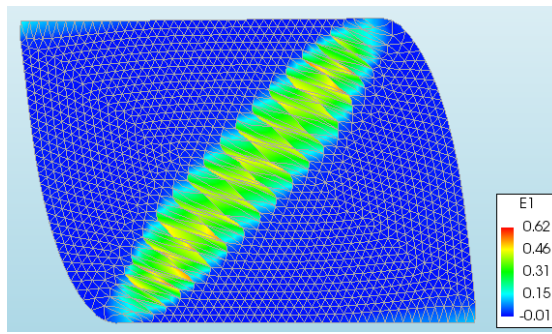
(c) 6.0 mm horizontal displacement

Figure A.6.1: SW110-0 Principle strain (E1) diagrams.



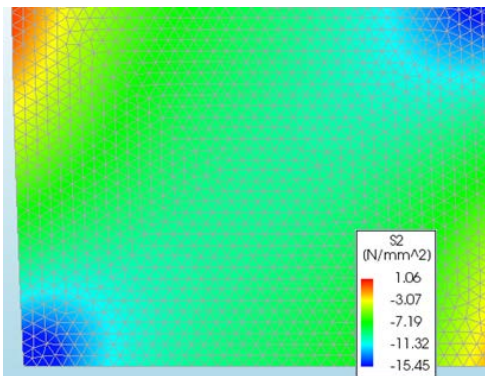
(a) 4.3 mm horizontal displacement

(b) 8.0 mm horizontal displacement

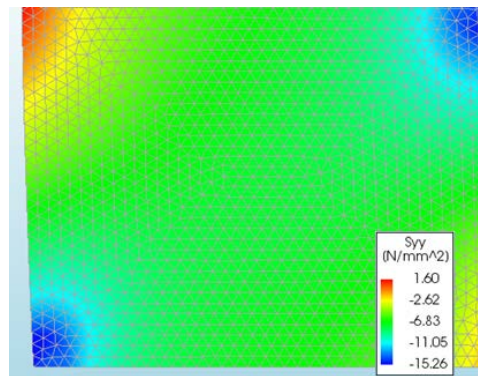


(c) 10.0 mm horizontal displacement

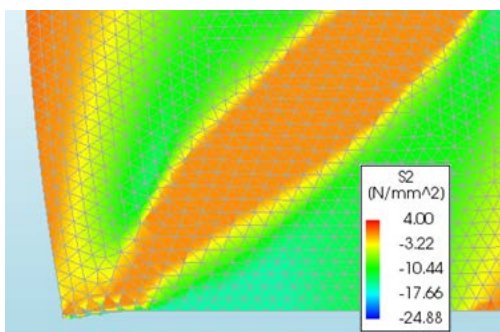
Figure A.6.2: SW330-0 Principle strain (E1) diagrams.



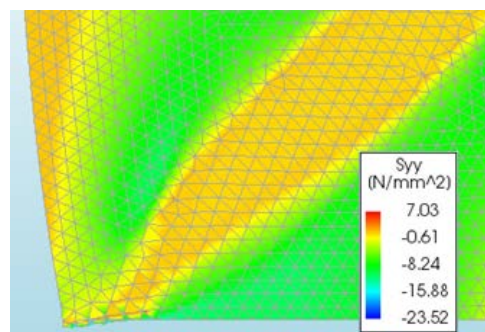
(a) S2 at 2.2 mm horizontal displacement



(b) Syy at 2.2 mm horizontal displacement



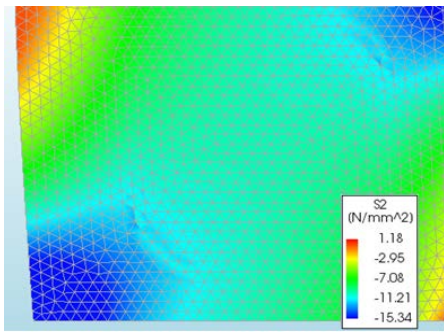
(c) S2 at 6.0 mm horizontal displacement



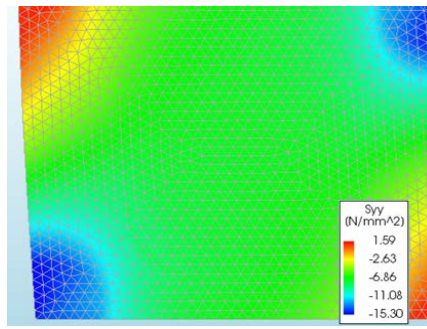
(d) Syy at 6.0 mm horizontal displacement

Figure A.6.3: SW110-0 Principle vertical stress (S2) and compressive stress (Syy) diagrams.

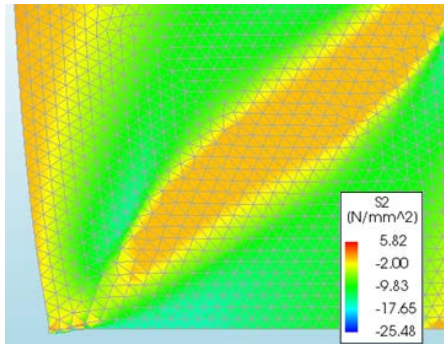
With and without bonded SHCC overlay



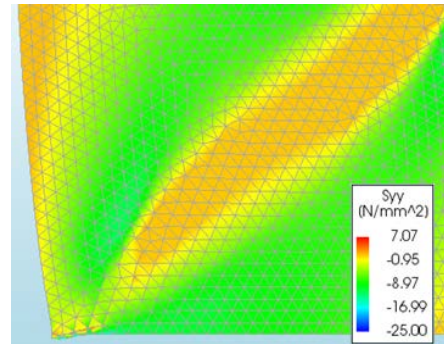
(a) S2 at 4.3 mm horizontal displacement



(b) Syx at 4.3 mm horizontal displacement

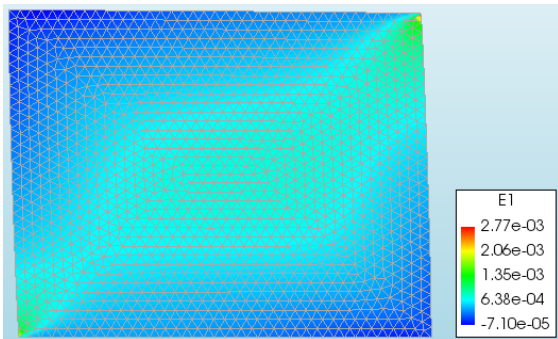


(c) S2 at 10.0 mm horizontal displacement

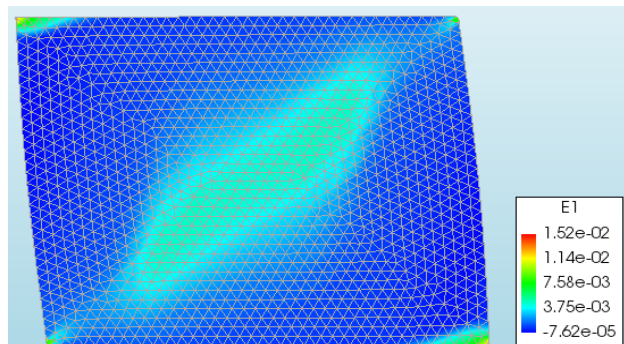


(d) Syx at 10.0 mm horizontal displacement

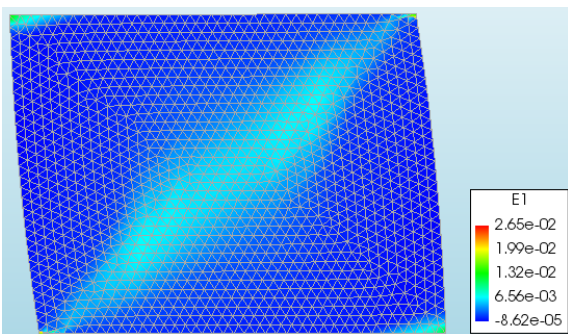
Figure A.6.4: SW330-0 Principle vertical stress (S2) and compressive stress (Syx) diagrams.



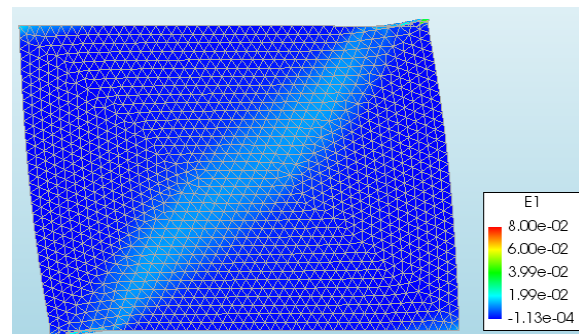
(a) 2.2 mm horizontal displacement



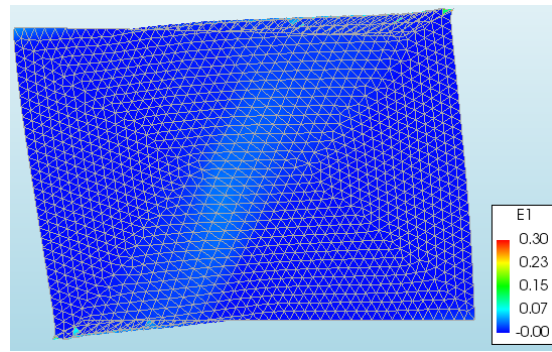
(b) 4.5 mm horizontal displacement



(c) 6.4 mm horizontal displacement

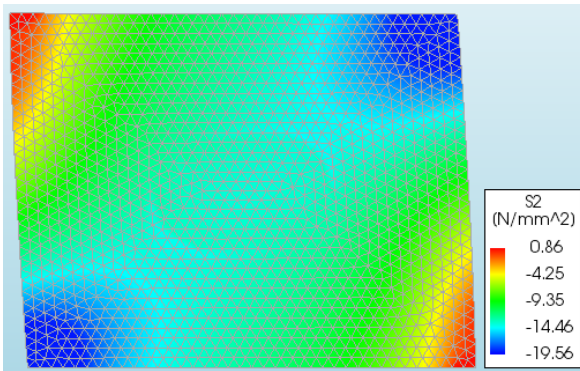


(d) 8.2 mm horizontal displacement

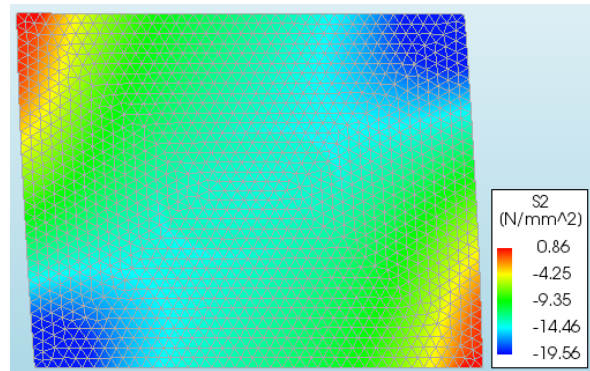


(e) 10.2 mm horizontal displacement

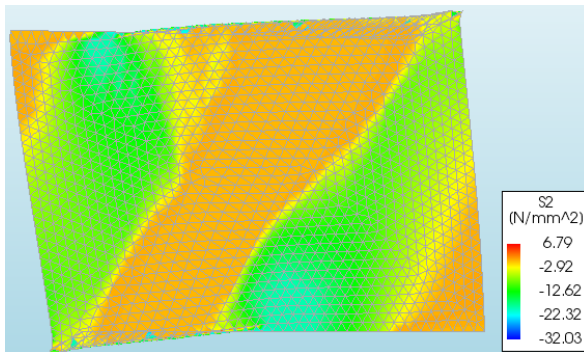
Figure A.6.5: SW220-10 Principle strain (E1) diagrams.



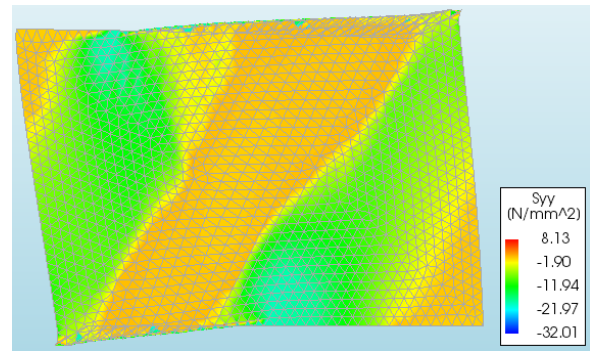
(a) S2 at 4.5 mm horizontal displacement



(b) Syy at 4.5 mm horizontal displacement

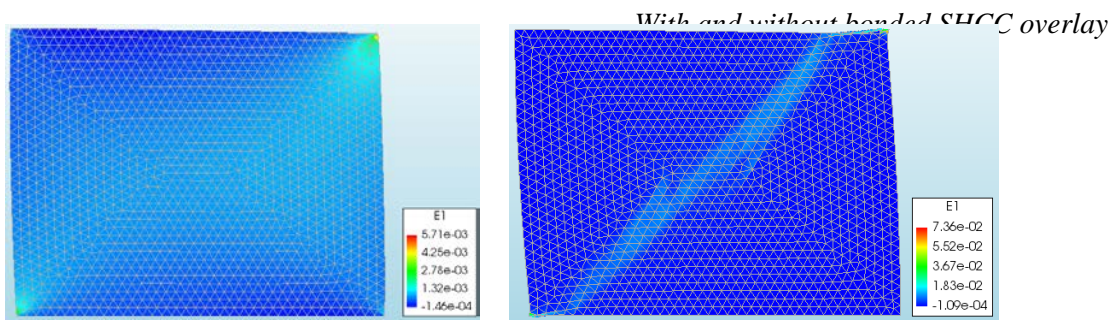


(c) S2 at 10.2 mm horizontal displacement



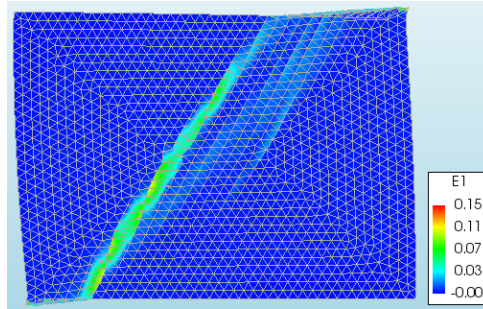
(d) Syy at 10.2 mm horizontal displacement

Figure A.6.6: SW220-10 Principle vertical stress (S2) and compressive stress (Syy) diagrams.



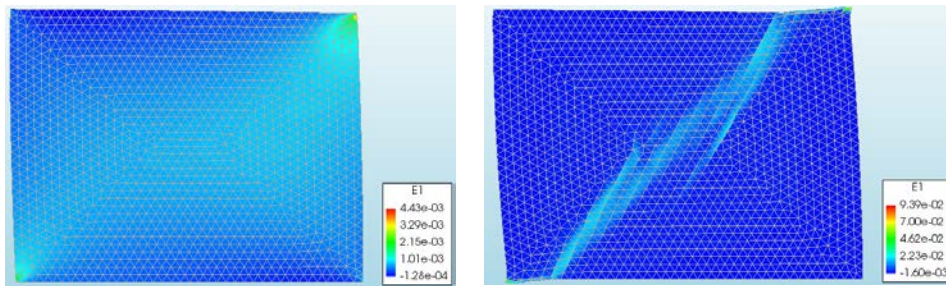
(a) 2.1 mm horizontal displacement

(b) 3.0 mm horizontal displacement



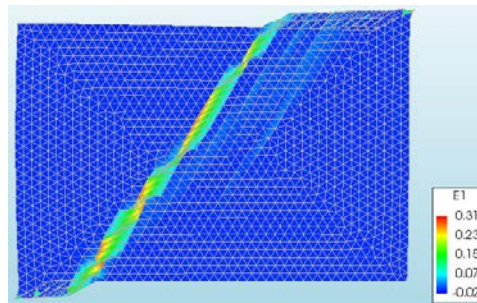
(c) 4.2 mm horizontal displacement

Figure A.7: SW110-10 Principle strain (E1) diagrams.



(a) 2.0 mm horizontal displacement

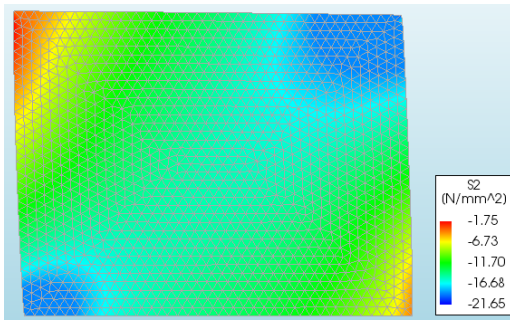
(b) 4.4 mm horizontal displacement



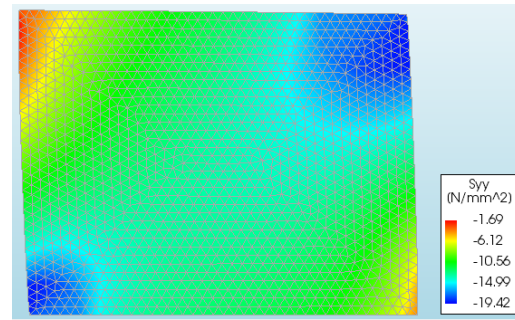
(c) 6.5 mm horizontal displacement

Figure A.8: SW110-15 Principle strain (E1) diagrams.

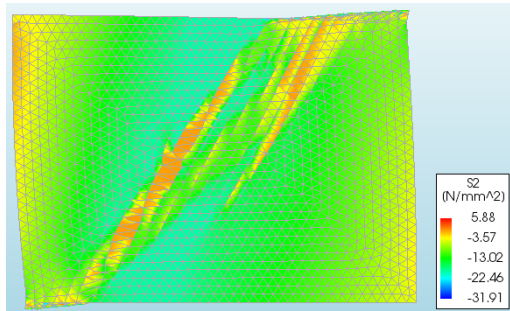
With and without bonded SHCC overlay



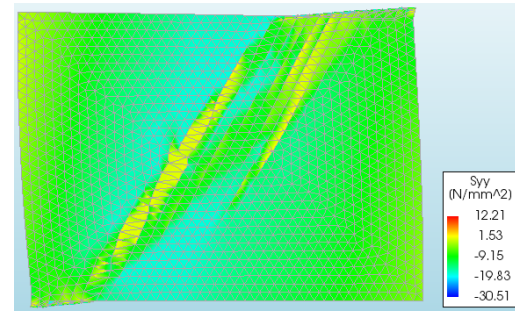
(a) S2 at 2.1 mm horizontal displacement



(b) Syy at 2.1 mm horizontal displacement

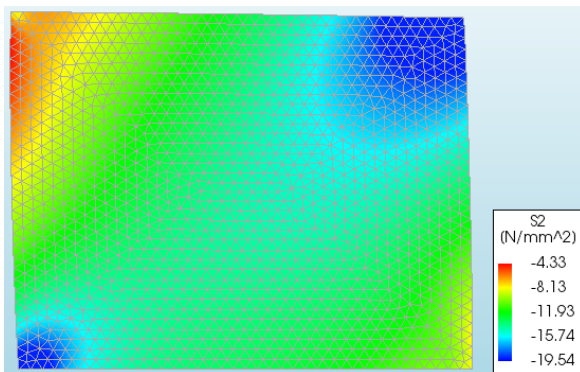


(c) S2 at 4.2 mm horizontal displacement

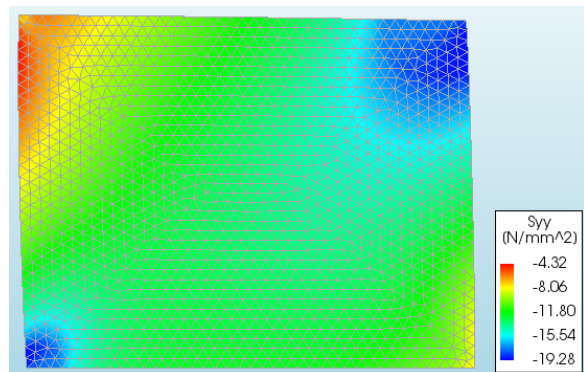


(d) Syy at 4.2 mm horizontal displacement

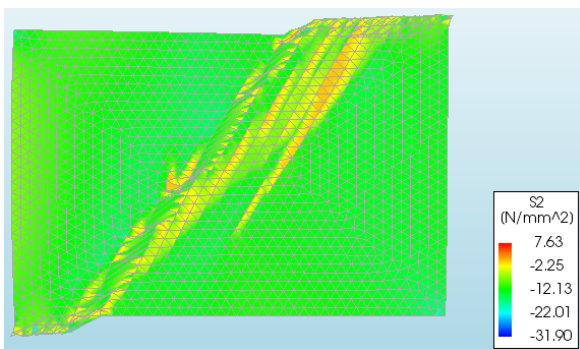
Figure A6.7: SW110-10 Principle vertical stress (S2) and compressive stress (Syy) diagrams.



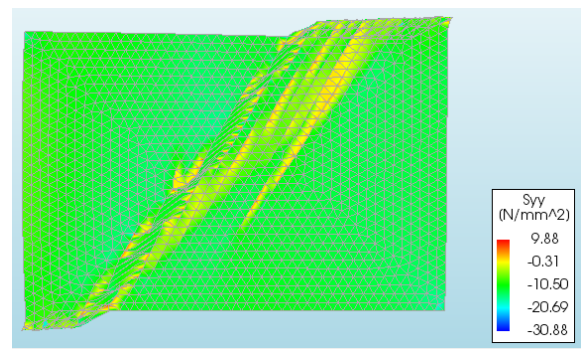
(a) S2 at 2.0 mm horizontal displacement



(b) Syy at 2.0 mm horizontal displacement



(c) S2 at 6.5 mm horizontal displacement



(d) Syy at 6.5 mm horizontal displacement

Figure A.6.8: SW110-15 Principle vertical stress (S2) and compressive stress (Syy) diagrams.

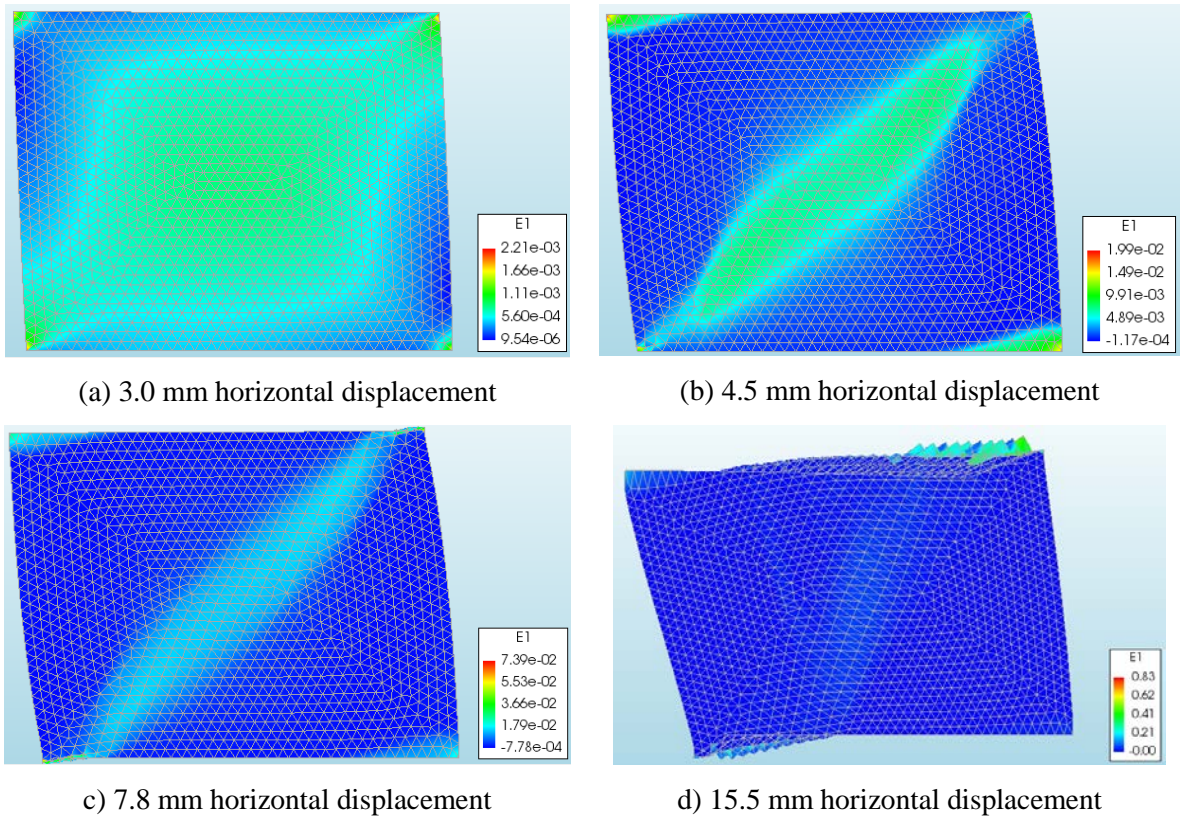


Figure A.6.9: SW330-10 Principle strain (E1) diagrams.

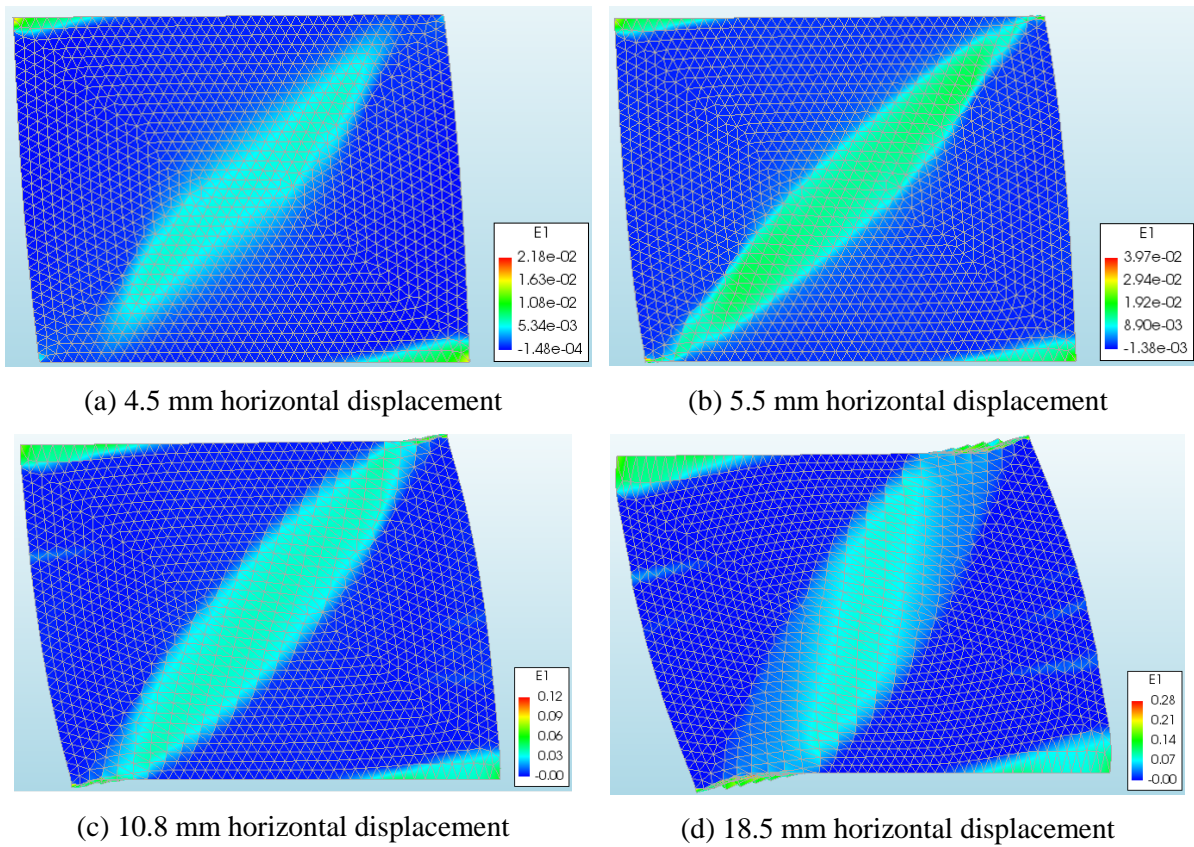
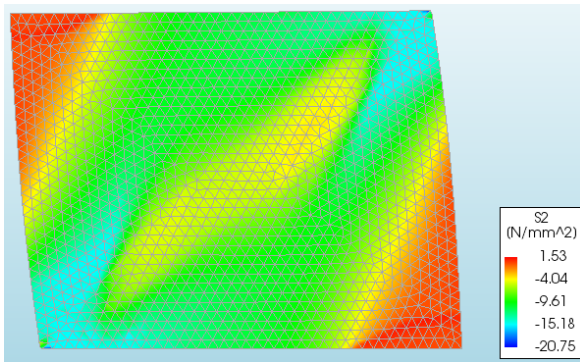
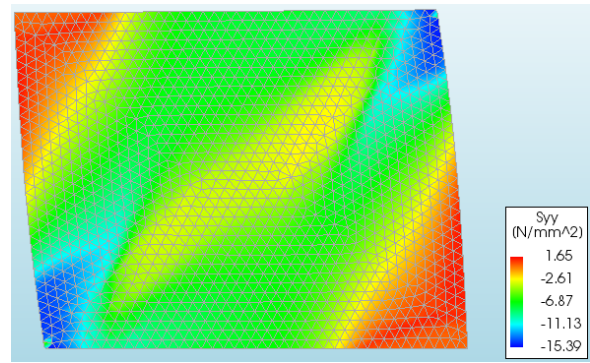


Figure A.6.10: SW330-30 Principle strain (E1) diagrams.

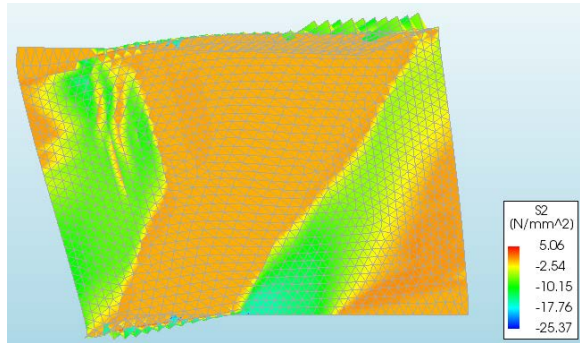
With and without bonded SHCC overlay



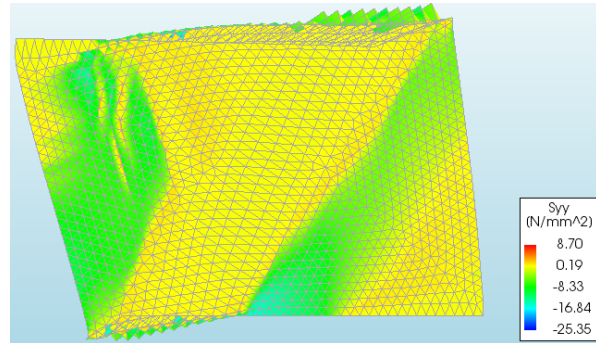
(a) S2 at 4.0 mm horizontal displacement



(b) Syy at 4.0 mm horizontal displacement

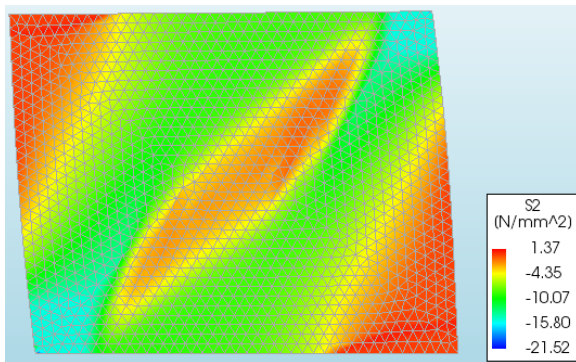


(c) S2 at 10.0 mm horizontal displacement

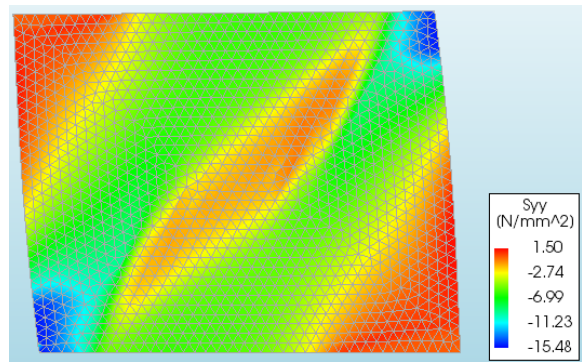


(d) Syy at 10.0 mm horizontal displacement

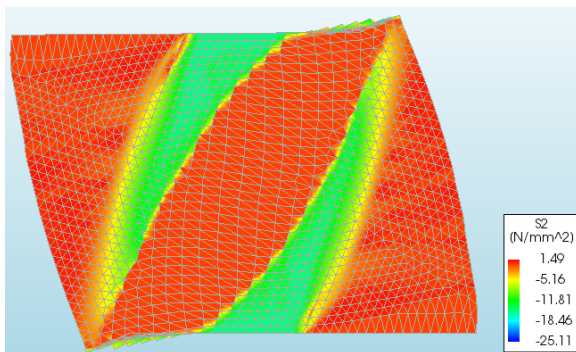
Figure A.6.11: SW330-10 Principle vertical stress (S2) and compressive stress (Sy_y) diagrams.



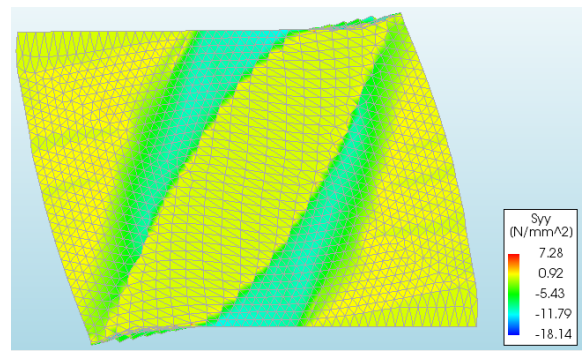
(a) S2 at 4.0 mm horizontal displacement



(b) Syy at 4.0 mm horizontal displacement



(c) S2 at 10.0 mm horizontal displacement



(d) Syy at 10.0 mm horizontal displacement

Figure A.6.12: SW330-30: Principle vertical stress (S2) and compressive stress (Sy_y) diagrams.

Appendix B – Experimental setup



Figure B.6.13: Storage of shear walls in structure lab.

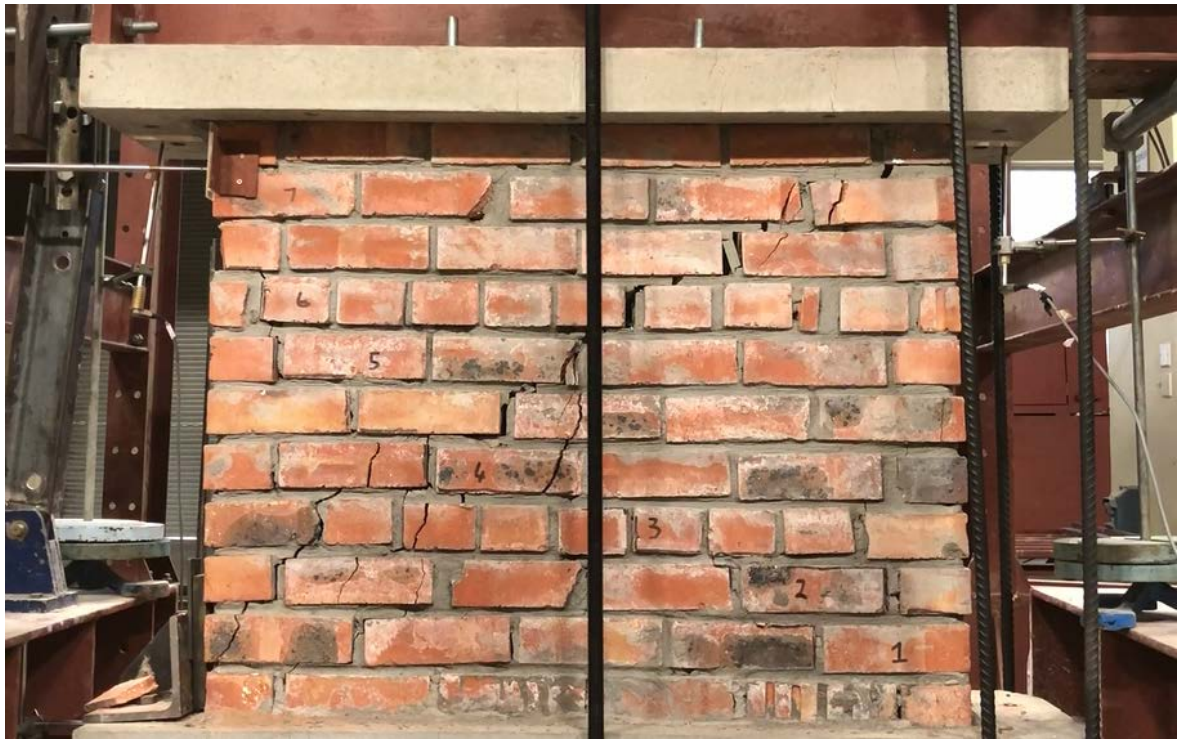


Figure B.6.14: Cracked shear wall specimen.